

May 2021

The Flow Less Traveled: Documenting Independent Original Research on Fluid Flow Interactions in the Laurentian Great Lakes and Immediate Surroundings

Thomas F. Hansen
University of Wisconsin-Milwaukee

Follow this and additional works at: <https://dc.uwm.edu/etd>



Part of the [Library and Information Science Commons](#), and the [Water Resource Management Commons](#)

Recommended Citation

Hansen, Thomas F., "The Flow Less Traveled: Documenting Independent Original Research on Fluid Flow Interactions in the Laurentian Great Lakes and Immediate Surroundings" (2021). *Theses and Dissertations*. 2669.

<https://dc.uwm.edu/etd/2669>

This Dissertation is brought to you for free and open access by UWM Digital Commons. It has been accepted for inclusion in Theses and Dissertations by an authorized administrator of UWM Digital Commons. For more information, please contact scholarlycommunicationteam-group@uwm.edu.

THE FLOW LESS TRAVELED: DOCUMENTING INDEPENDENT ORIGINAL RESEARCH ON FLUID
FLOW INTERACTIONS IN THE LAURENTIAN GREAT LAKES AND IMMEDIATE SURROUNDINGS

by

Thomas F. Hansen

A Dissertation Submitted in
Partial Fulfillment of the
Requirements for the Degree of

Doctor of Philosophy
in Freshwater Science

at

The University of Wisconsin-Milwaukee

May 2021

ABSTRACT

THE FLOW LESS TRAVELED: DOCUMENTING INDEPENDENT ORIGINAL RESEARCH ON FLUID FLOW INTERACTIONS IN THE LAURENTIAN GREAT LAKES AND IMMEDIATE SURROUNDINGS

by

Thomas F. Hansen

The University of Wisconsin-Milwaukee, 2021
Under the Supervision of Professor John A. Janssen

This work is a compilation of several research projects undertaken by the author. Each research effort identifies a problem which has been addressed traditionally using methods that are significantly costly, to such an extent that, in general, funding, convenience, and practicality are primary limiting factors to their effective implementation. In each case, the author has been able to either build upon existing, less expensive alternatives, or even invent novel approaches. The fundamental recurring research question is, can creative, even novel, computational approaches make more efficient use of resources to interpret or present data in such a way as to make what was previously impractical, inconvenient, or simply unachievable, now well within reach of even those with modest budgets? The first detailed is a research program which examines applications of digital in-line holographic microscopy, which operates by effectively replacing physical lenses with computational methods. The next uses digital storage and visualization to create real-time updating bathymetry maps using single-beam sonar already installed on most aquatic vessels. Also reviewed here is an interactive real-time computational fluid dynamics (CFD) model in which the user can simply reach out their hand and see the simulated fluid flow respond with swirling vortices and other fluid phenomena, a powerful tool for live demonstrations using equipment already installed in most classrooms. Finally, machine learning is applied to the problem of measuring fluid flow, in which a simple subsurface float can be used to measure current speed nearly as well as an expensive ADCP using a trained neural network running on an ordinary PC. Each are examples of replacing or augmenting existing, relatively expensive methods with far less costly alternatives, bringing the science of freshwater to a potentially much wider participatory scale than previously possible.

Copyright by Thomas F. Hansen, 2021
All Rights Reserved

To
My family,
Peter Hansen, Jen Hansen,
Alex N. Hansen, and Max A. Hansen

TABLE OF CONTENTS

List of Figures.....	vii
List of Tables.....	ix
ACKNOWLEDGEMENTS.....	x
FRONTISPIECE AND EPIGRAPH	xi
INTRODUCTION.....	1
CHAPTER 1. MEASURING FLOW SPEEDS IN NATURAL WATERS BY TRAINING AN ARTIFICIAL NEURAL NETWORK TO ANALYZE HIGH-FREQUENCY FLOW-INDUCED VIBRATIONS OF TETHERED FLOATS.....	3
MANUSCRIPT TEXT	4
REFERENCES	20
FIGURES	26
CHAPTER 2. DIGITAL INLINE HOLOGRAPHIC MICROSCOPY	38
CHAPTER 3. TECHNICAL BRIEF: COLLECTING REAL-TIME BATHYMETRY ABOARD A RESEARCH VESSEL.....	40
REFERENCES.....	45
CHAPTER 4. A HIGHLY INTERACTIVE FLUID DYNAMICS MODEL.....	46
CHAPTER TEXT.....	47
REFERENCES.....	72
APPENDIX A. UWM RESEARCH FOUNDATION INVENTION DISCLOSURES	75
APPENDIX B. PUBLISHED MANUSCRIPT ON HAND-HELD HOLOGRAPHIC SENSOR: OPTICALLY BASED BACTERIA HAND-HELD SENSOR: FROM FUNDAMENTALS TO PROOF OF CONCEPT.....	97
APPENDIX C. PUBLISHED MANUSCRIPT ON HAND-HELD HOLOGRAPHIC SENSOR: OPTICALLY BASED HANDHELD SENSOR FOR VISUALIZATION AND QUANTIFICATION OF CRYPTOSPORIDIUM PARVUM.....	114

APPENDIX D. PROVISIONAL PATENT APPLICATION: FLOW SIMULATION AND VISUALIZATION WITH REAL-TIME VIDEO INTERACTIVITY	129
CURRICULUM VITAE.....	145

LIST OF FIGURES

Figure 1. The flow less traveled	2
Figure 2. A schematic diagram demonstrating the principles of operation	26
Figure 3. Diagram of custom-built float (not to scale)	26
Figure 4. Map of the deployment area.....	27
Figure 5. The orientation of accelerometer and magnetometer sensor axes on the TCM.....	27
Figure 6. Map of the deployment area.....	28
Figure 7. Example data from lab-constructed float assembly.....	28
Figure 8. Depicted here are the raw time series readings from the accelerometer.....	29
Figure 9. Schematic Diagram of experimental ANN used in this work	29
Figure 10. Dense Perceptron internal structure.....	30
Figure 11. The design of the CNN sub-network.....	30
Figure 12. Original data from accelerometer x-axis sensor	31
Figure 13. Each sample of w data points is associated with a single-speed calculation	31
Figure 14. Graphically shows accelerometer readings reflected and rotated.....	32
Figure 15. Schematic of information flow	32
Figure 16. The initial set of baseline results	33
Figure 17. Results of model training on original samples plus the augmented reflected data samples	34
Figure 18. The results of rotating the original plus the reflected samples	35
Figure 19. The results of reflection and rotation data augmentation to the data from the lab-built floats	36
Figure 20. Scatterplot of the ADCP current speed, plotted against the values calculated by the ANN.....	36
Figure 21. ADCP readings plotted against ANN results to demonstrate the model's performance	37
Figure 22. Detailed rendering of bathymetry obtained with single-beam sonar	41
Figure 23. Some heavily-visited areas have a lot of data recorded over many cruises	43
Figure 24. The dock location can provide a ground-truth for depth measurements	43
Figure 25. Soundings from R/V Neeskay at various locations plotted against the USGS gauge readings	43

Figure 26. Bathymetry of Hansen Point in the Lake Michigan Mid-Lake Reef Complex	44
Figure 27. A preliminary demonstration of a hydrodynamic model.....	44
Figure 28. The author’s nephew Max Hansen interacts with the CFD model	47
Figure 29. Simplified schematic drawing of the design and organization of the system.	48
Figure 30. The nine basis vectors used for 2-D LBM (a.k.a. D2Q9).....	49
Figure 31. Illustration of the LBM "bounce-back" scheme	51
Figure 32. Using chessboard pattern to adjust the camera image	53
Figure 33. Simulated Injected Dye Advection Overlay	55
Figure 34. Lagrangian particles overlay	56
Figure 35. Speed	57
Figure 36. Vorticity	58
Figure 37. LIC	59
Figure 38. LIC+Speed	60
Figure 39. LIC+Vorticity.....	61
Figure 40. Pressure	62
Figure 41. Sudden introduction of cylinder into flow.....	63
Figure 42. Cylinder at Reynolds number ≈ 20	64
Figure 43. Cylinder at Reynolds number ≈ 30	65
Figure 44. Cylinder at Reynolds number ≈ 40	66
Figure 45. Cylinder at Reynolds number ≈ 50	67
Figure 46. Cylinder at Reynolds number ≈ 60	68
Figure 47. Children interacting with the display at Milwaukee Maker Faire 2015	70
Figure 48. Technology featured in UWM Research Foundation Annual Report 2016	71
Figure 49. Technology featured in UWM Research Foundation Annual Report 2017	71

LIST OF TABLES

Table 1. Data Collection Times and select statistics.....	8
Table 2. Data Collection Times and select statistics.....	9
Table 3. Rotational angles are used to create "augmented" samples for ANN training.....	16
Table 4. Rotational angles are used to create "augmented" samples for ANN training.....	16
Table 5. A listing of data values logged onboard the R/V Neeskay at a rate of 1 Hz.....	42
Table 6. Critical Reynolds numbers from various studies.....	69

ACKNOWLEDGEMENTS

I would like first to acknowledge Distinguished Professor Rudi J. Strickler of UWM. He was the first person I talked to about the hair-brained idea of earning a Ph.D. in my middle age. I half expected him to say, "ah, you no need!" but instead, he was very supportive of the idea. He pointed me in the direction of microfluidics, which was a brilliant idea. My interest quickly focused on creating numerical models of the fluid dynamics involved. Doing my research from the School of Freshwater Sciences, I had easy access to collaborators that work on the more macro scales of lakes and rivers. So I have taken the tools and experience I had developed for microfluidics and have applied them to larger physical scales. In the meantime, I did forge a successful collaboration that began while studying microfluidics, which has produced several peer-reviewed publications to date (Thompson, Hable, Honts, et al. 2020; Thompson, Hable, Young, et al. 2020).

I would also like to acknowledge the encouragement and inspiration, and company at countless soup lunches that I received from my first advisor Tom Consi. I will never forget what he said to me one day, shortly before I started the doctoral program. We were co-investigators on an instrumented buoy project. Tom observed, "You are so good with students and have such a passion for this research. You're here to make the rest of us look bad." I can only hope to live up to such a high opinion and vision in my future career.

Most of all, I acknowledge the encouragement and tireless effort put forth on my behalf by my current advisor, John A. Janssen. His enthusiastic interest in an extensive and varied list of subjects, from fisheries to neural networks to fluid dynamics, has led to many fruitful discussions. His quote from a popular early 80's Tom Cruise movie (which I will not repeat here) served to remind me that sometimes science, as in life itself, is about progress and not perfection.

I would also like to acknowledge the doctoral committee members I have not already mentioned, past and present: Val Klump, James Waples, Matthew Smith, and Hector Bravo. Their input, criticisms, and encouragement to myself personally and my research programs I will not forget.

FRONTISPIECE AND EPIGRAPH



Photo: Tom Hansen

Just a few blocks away from the UWM campus lies one of the largest bodies of freshwater in the world. Known collectively as "gichi-gami" by the native Ojibwe peoples, the North American Great Lakes are in fact an incredible natural wonder with many stories to tell. They hold fully 20% of the world's surface freshwater supply and are home to vast ecosystems just as complex and varied as the environment on land that we observe with our own five senses every day.

Yet most of us drive right past the lake almost every day and just see the surface [see photo above], and that's it.

Now, let's take a moment to put this in perspective: imagine if, one day, a new type of locust came down from the sky, and within just a few years' time virtually transformed the entire landscape, covering virtually every square inch of the land, our lawns, parks, forests, even our homes —everything—choking out virtually every other plant and animal that was there before.

Sounds absolutely horrible and unthinkable, doesn't it?

Yet, something just like that has been going on for the last 20 years, just those same few blocks away, as the zebra and quagga mussels have dramatically changed the ecosystems of Lake Michigan, completely covering huge swaths of the bottom—every rock, crevice, hill and valley as far as the eye can see. But most of us just look at the lake and see that same surface, and think Nothing. Had. Even. Happened.

My research explores new ways to increase awareness of these precious lakes, sensing what's going on, such as how the water currents are flowing, listening for the pulse of the ecosystem. Further, it explores new technologies to create imaginative interactive displays to help convey what all this data are telling us, and at as low a cost as

possible. It accomplishes this by using commonplace technology, such as the cameras, motion sensors, and wireless radios that almost all of us carry around with us every day in our smartphones.

This leads us to a major goal of my work, which is to democratize freshwater science, to give those of us without big research grants—the students, the citizen scientists, the hobbyists—and, perhaps most important of all, the next generation, our children, a chance to grasp what the impact of something like the dreissenid mussel invasion can have on day-to-day life on the other side of this surface.

My research envisions a day when homemade water monitoring buoys rival the popularity of do-it-yourself weather stations; a day when there are just as many 5th grade science fair projects about fish swimming in water as there are about birds flying through the air—a day when learning about a mother preparing to lay her eggs might just as easily be about a female lake trout carefully selecting that perfect spot on a reef for her brood to hatch safe from predators, as about a robin making its nest in a nearby tree.

—Tom Hansen, speech and single slide from 2019 Three Minute Thesis competition

INTRODUCTION

This work is a compilation of several research projects undertaken by the author. Each research effort identifies a problem which has been addressed traditionally using methods that are significantly costly, to such an extent that, in general, funding, convenience, and practicality are primary limiting factors to their effective implementation. In each case, the author has been able to either build upon existing, less expensive alternatives, or even invent new novel approaches. The fundamental recurring research question is, can creative, even novel, computational approaches make more efficient use of resources to interpret or present data in such a way as to make what was previously impractical, inconvenient, or simply unachievable, now well within reach of even those with modest budgets? The first detailed is a research program which examines applications of digital in-line holographic microscopy, which operates by effectively replaces physical lenses with computational methods. The next uses digital storage and visualization to create real-time updating bathymetry maps using single-beam sonar already installed on most aquatic vessels. Also reviewed here is an interactive real-time computational fluid dynamics (CFD) model in which the user can simply reach out their hand and see the simulated fluid flow respond with swirling vortices and other fluid phenomena, a powerful tool for live demonstrations using equipment already installed in most classrooms. Finally, machine learning is applied to the problem of measuring fluid flow, in which a simple subsurface float can be used to measure current speed nearly as well as an expensive ADCP using a trained neural network running on an ordinary PC. Each are examples of replacing or augmenting existing, relatively expensive methods with far less costly alternatives, bringing the science of freshwater to a potentially much wider participatory scale than previously possible.

Following the science

These varied areas of research were not arrived at arbitrarily. The chart shown in Figure 99 shows the relationship among the various research interests that were followed to arrive at the projects in this work.

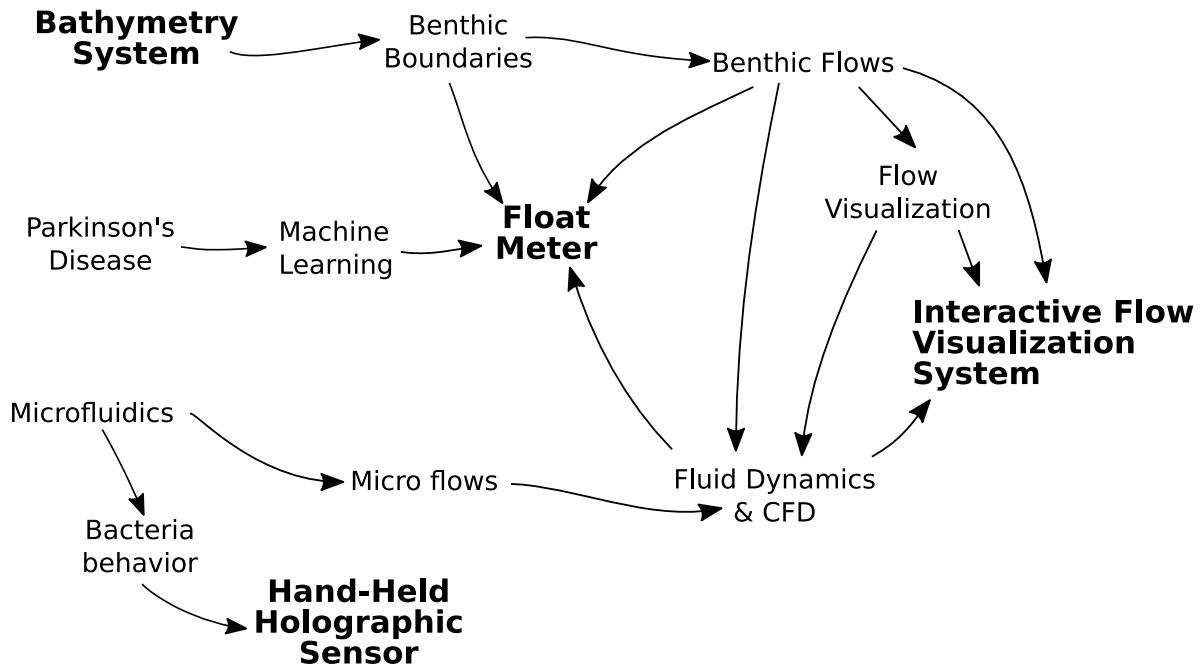


Figure 1. The flow less traveled: each arrow represents following the science to the project or area of interest.

CHAPTER 1

MEASURING FLOW SPEEDS IN NATURAL WATERS BY TRAINING AN ARTIFICIAL NEURAL NETWORK TO ANALYZE HIGH-FREQUENCY FLOW- INDUCED VIBRATIONS OF TETHERED FLOATS

MEASURING FLOW SPEEDS IN NATURAL WATERS BY TRAINING AN ARTIFICIAL NEURAL NETWORK TO ANALYZE HIGH-FREQUENCY FLOW- INDUCED VIBRATIONS OF TETHERED FLOATS

Manuscript as submitted to Environmental Monitoring and Assessment, January 13, 2021

Abstract

Measuring water currents in natural waters is limited by the cost of sensors. Standard sonar-based acoustic current doppler profilers (ADCPs) are high cost, about \$10K per unit. Tilt current meters (TCMs) are much cheaper. They consist of a bottom-mounted subsurface float equipped with an inertial measurement unit (IMU) and data center that records the float's motion and attitude as a time series. The flow speed is measured by calculating the tilt angle of the float in response to the current. However, tilt-based measurements require the float system to be carefully engineered, and its physical response optimized for good results. Even so, high-frequency flow-induced vibrations often dominate the motion and must be averaged and filtered out of the data and discarded. This represents the loss of potentially valuable information but decoding the high-frequency components for such useful data is difficult. These experiments explore using an artificial neural network (ANN) approach to extract useful information from that high-frequency data. The methods were informed by the ANN designs and data augmentation techniques used by neurologists to observe the tremors and other motions exhibited by patients experiencing symptoms of Parkinson's disease. The results are clear and promising. This novel approach could facilitate new sensor system designs that can be empirically or self-calibrated more efficiently and have a lower barrier to application than those currently available.

Keywords: fluid flow, water current, natural waters, machine learning, artificial neural networks, neural networks, convolutional neural networks

Introduction

Background

Accurate measurement of water current flows is essential to most areas of aquatic environmental research, from fisheries and aquatic habitat studies (Houghton et al. 2010; Johansen 2014) to physical limnology (Mortimer 2004)

and oceanography (Hokimoto 2012; Sieyes et al. 2008). Despite its high value, the barrier in obtaining such data has generally been the high cost of the sensors (Albaladejo et al. 2010) (Beltaos 2012).

A more inexpensive type of water current meter, known as a tilt current meter, has come into use (Sheremet 2009; Figurski et al. 2011; Anarde and Figlus 2017). Meters of this type have grown in popularity primarily due to the availability of inexpensive micro-electro-mechanical systems (MEMS) inertial motion units, or IMUs (Kamil et al. 2014; Santoso et al. 2015; Vasyukov et al. 2014).

MEMS-based tilt current meters, which effectively and accurately measure current flows in environmental waters, are now commercially available (Lowell Instruments LLC, North Falmouth, MA 2016), and their performance rivals that of ADCPs for single-depth measurements (Figurski et al. 2011; Sheremet 2009; Lowell et al. 2015). The ambient flow is determined by recording the float's current-induced motions as a high-frequency time series using embedded MEMS IMU sensors. Tilt is then calculated by averaging this time-series to smooth out any vortex shedding or other flow-induced vibrations and applying standard formulae to determine the tilt angle. The principle of hydrodynamic drag (Hoerner 1965)—which establishes a predictable relationship between the speed of ambient fluid flow surrounding an immersed body and the drag force experienced by that body—allows the tilt angle to be looked up in a calibration table prepared by the manufacturer to determine the flow speed which corresponds with the observed tilt angle. Please refer to Figure 2 for a schematic.

The problem

Traditional tilt-based calculations performed on the data from tilt-based current meters involve filtering out the collected data's high-frequency component. This component—caused by vortex shedding and other flow-induced vibrations—represents lost information that contains useful data that could increase the effectiveness of calibration and measurements.

The high-frequency component of this data is rich with information. Several laboratory studies have been done (Johnstone and Stappenbelt 2016; Marble et al. 2018), which were focused on observing and predicting the vortex-induced motions produced by subjecting immersed cylinders to known and controlled flows. These studies show that cylinders not dissimilar to the subjects of this work exhibit very complex vibrational behavior in the presence of fluid flow, the nature of which is at least partially dependent on the speed of such flow.

Also, research in the field of environmental flow and vortex-induced vibrations is quite extensive. However, the existing body of research is almost exclusively motivated by and focuses on assessing and mitigating the destructive and harmful effects of vortex shedding in various environmental and industrial settings. Examples include the operation of ROVs (Sayer 1996; Allen and Hening 2002; Gomes et al. 2003) and maintenance of offshore platforms (Gonçalves et al., 2010; Irani and Finn, 2004). A very few studies, such as (Zahari and Dol 2014), look at vortex shedding as a way to generate electricity.

A well-established technology for measuring fluid flow speed uses analysis of vortex-induced vibrations of an immersed bluff body: the vortex flowmeter (Fussell 1973; Hondoh et al. 2001; Mcmurtrie Charles and Rodely Alan 1971; Venugopal et al. 2011; Xu et al. 2009). However, this technology only appears to be used in closed pipes in commercial and industrial applications—a well-controlled environment.

An innovative solution to an ill-posed problem

Given the very high complexity that characterizes flow-induced vibrations, particularly in the relatively noisy environment found in natural waters, the author proposes experimentally investigating the efficacy of training an artificial neural network (ANN) to determine flow speed based on those vibrations.

Neural networks have a long history of demonstrating the ability to identify patterns in data, effectively cut through noise, and even solve problems previously thought to be statistically impossible (Sejnowski 2020). In particular, neural networks have been successfully applied to ill-posed problems (Raissi et al. 2018) or inverse problems. Data on the effects of phenomena of interest are known, and these data must be used to infer characteristics of the original phenomena.

These attributes, among others, have led to artificial neural networks being increasingly applied to the study of fluid dynamics (Morton et al. 2018; Thuerey and Xiangyu 2018; Wang et al. 2018).

Inverse problems are common in healthcare due to the high costs and harmful physical effects upon patients that direct physical observation of their internal organs generally incurs. Thus, non-invasive medical diagnostic and monitoring methods are largely inverse problems that rely on using external observations to infer internal state. Artificial neural networks have had a substantial positive impact on the effectiveness of medical imaging techniques such as X-rays, CAT scans, and MRIs (Chen et al. 2019), as well as other non-invasive data collection techniques such as wearable sensors (Gholamiangonabadi et al. 2020; Mathur et al. 2018; Zhang et al. 2019).

The experimental design was informed in no small part by the artificial neural network (ANN) designs and data augmentation techniques used by neurologists to observe the tremors and other motions exhibited by patients experiencing symptoms of Parkinson's disease and other motion disorders (Um et al. 2017). These techniques proved invaluable in these experiments.

All ANN models were implemented in Python 3 (Van Rossum and Drake 2009) within the Anaconda environment (Anaconda Inc. 2020) using the popular Tensorflow (Abadi et al. 2016) library. Additional libraries and functions are cited as they are mentioned.

Materials and Methods

Data were collected from several deployments over several years as part of an ongoing effort to explore inexpensive sensor alternatives. This study examines data from two sets of these deployments: a small time series recorded by a unit designed and built in-lab using spare parts and a much larger set of time series collected from a manufactured commercially available tilt current meter.

Lab-constructed floats

There were no cheap and commercially available MEMS-based tilt current meters in 2015. (Lowell et al. 2015). A small group of researchers, including the author, set about the design and construction of a set of ad-hoc floats, primarily using spare tubing and other materials, to prove a concept.

Physical description

Several floats were constructed, comprised of approximately 6-inch sections of about 6-inch diameter PVC pipe. Sealed inside were 16 C-cell batteries, which powered a custom-built circuit assembly consisting of an Arduino Uno, a standard MEMS accelerometer, magnetometer, and gyroscope. The onboard Arduino processor ran custom code to collect the accelerometer, magnetometer, and gyroscope readings at a sample rate of 2Hz. Please refer to Figure 3 for a schematic diagram of the float design.

Deployment locations

The lab-constructed floats were deployed by ship in Lake Michigan's nearshore, in the north gap of the outer harbor of Milwaukee, Wisconsin, on November 16, 2015. The exact locations and dates/times of the deployments are detailed in Table 1 and Figure 4.

Deployment Data Collected						
Deployment	Dates/Times		Readings (N)	ADCP Speeds (cm/s)		
	Start	End		Min	Median	Max
1	11/16/2015 12:19:19	11/16/2015 13:45:09	10301	33.5085	95.5753	139.1119
2	11/16/2015 12:20:16	11/16/2015 13:45:09	10187	33.6795	95.8240	139.1119

Table 1. Data Collection Times and select statistics. Readings above the 99th percentile were excluded from the data to compute these statistics to reduce outliers' effect on the result.

Commercial off-the-shelf (COTS) unit

In 2018, the laboratory obtained a commercially produced tilt current meter, a Lowell Instruments TCM-1 (Lowell Instruments LLC, North Falmouth, MA 2017).

Physical description

The Lowell Instruments TCM-1 (Lowell Instruments LLC, North Falmouth, MA 2016) consists of an extended, thin cylindrical package. The sensor, datalogger, and battery compartment are located at the instrument's anchored end, contained entirely within the cylinder. Please refer to Figure 5 for a schematic diagram of the design.

Deployment locations

The instrument was deployed at various locations along an estuarine river face dock and its immediate vicinity, per the accompanying Table 2 and Figure 6. The site, located in the Milwaukee Inner Harbor, was chosen because the current flows there are dominated by the effects of seiche in Lake Michigan, regularly exhibiting a range of flow speeds and changes of direction (House 1987; Mortimer 2004)

Deployment Data Collected						
Deployment	Dates/Times		# of datapoints N	Tilt-Calculated Speeds (cm/s)		
	Start	End		Min	Median	Max
2	6/28/2018 10:45	7/2/2018 9:58	5,425,865	0.1142	4.4563	18.3259
3	7/19/2018 13:18	7/20/2018 13:58	1,406,100	0.2146	1.7819	13.4885
4	7/20/2018 14:00	7/23/2018 12:22	4,012,509	0.0297	1.7409	11.5482

5	7/24/2018 16:28	7/25/2018 12:55	1,138,450	0.0423	0.7234	9.3730
6	7/31/2018 12:08	8/2/2018 14:25	2,866,453	0.0357	3.2495	13.5263
7	8/2/2018 14:28	8/3/2018 14:28	1,368,766	0.0401	1.6116	10.0425

Table 2. Data Collection Times and select statistics. Readings above the 99th percentile were excluded from the data to compute these statistics to reduce outliers' effect on the result.

Processing the data

Characterization of the motion data recorded

The lab-built floats recorded the following data points at a rate of 2Hz: accelerometer x, y, and z axes; magnetometer x, y, and z-axes; and gyroscope x, y, and z axes. A total of 85 minutes of data were recorded. A sample of those data is charted in Figure 7. A strong high-frequency component is evident, which makes it an excellent example for our experiments. For the data we have available for these units, a nearby ADCP, a Nortek Aquadopp, located within a few meters of the units, recorded the current speed simultaneously. These ADCP readings were used during calibration and testing.

Like the lab-built units, the IMU in the commercial TCM-1 tilt meter consists of three orthogonal accelerometers and three orthogonal magnetometers aligned with the *x*, *y*, and *z* axes. The sensors are positioned with the positive *z*-axis pointing down the center of the cylindrical float towards the tethered pivot, and the *x* and *y* axes normal to the *z*-axis using the right-hand rule. (The orientation of the sensors with respect to the sensor packaging was depicted in Figure 5.) Note that the commercial unit does not have any gyroscope sensors.

Collected data, a representative sample of which is charted in Figure 8, was initially analyzed using the manufacturer's software. This particular sensor has a very well-documented set of calibration trials published and available (Lowell et al. 2015), demonstrating that the tilt-based calculations compare quite favorably to ADCP measurements. So these calculated values were directly used to calibrate the ANN-based methods.

Artificial Neural Network Architecture

The design goal is to produce an artificial neural network (ANN) that takes as input the high-frequency components of the motion sensor data from a subsurface float—normally filtered out as noise—and can decode, or infer, the speed of the water current that the float was experiencing at the time the data was recorded. This is known as a function estimation problem or a regression.

Artificial neural networks, or ANNs, have seen recent applications in vibrational analysis. A good starting point for this research was found in the architecture used to classify Parkinson's disease patients' motor states (Um, 2017). There is an emphasis in that design on extracting the most information from the least amount of data.

For this work, some features of the ANN had to be modified to achieve acceptable results. The global average pooling (GAP) layer that served to reduce the output for classification turned out to be inappropriate for this application, which, in contrast to classification, is a regression, or continuous function estimation. Using the GAP layer often caused the model training to fail to converge. Similar results were observed when using fully connected ReLU-activated layers as the final layers of the model. In the end, a small number of fully connected layers with a linear activation function gave reliably good results.

A convolutional neural network (CNN) was also introduced to recognize repeated features in the data samples easily. The traditional CNN architecture generally has a deep (several consecutive layers) CNN sub-network fed into a fully-connected set of layers, with a small number of linearly-activated layers that drive the output. This seemed to work well for this problem up to a point. However, if the input is fed in parallel to both a CNN subnetwork and a fully-connected subnetwork, and then the concatenated outputs of both networks are fed into a small number of linearly activated layers to drive the output, the resulting network outperformed the traditional CNN architecture for this problem.

The basic layout of the model is as follows. The input examples were fed into a multilayer dense perceptron block and a multilayer convolutional neural network (CNN) in parallel. Both subnetworks' output was then concatenated and fed into a second multilayer dense Perceptron block, which then drives a very small perceptron, labeled "Regression Prep," defined using a linear activation function. (In these experiments, the omission of a final linear perceptron often caused calibration convergence failure.) The model was then trained using the tilt-calculated flow speed as the label. With the loss function defined as the mean squared error, the error is defined as the difference between the tilt-calculated flow speed and the neural network's output. Please refer to Figures 9, 10, and 11 for schematic representations of the ANN and component subnetworks. The next section details the dimensional hyperparameter values that were used.

Initial ANN hyperparameter tuning and optimization

Initial hyperparameters (such as the actual depth and width of each component of the network) were calculated using a genetic algorithm with design elements drawn from several sources (Bergstra et al. 2011; Fridrich 2017;

Ippolito 2020; Orive et al. 2014; Pant 2018) This initial optimization was used as a starting point, after which manual adjustments were made based on empirical observations. The final parameters used for the commercial float data were: Dense1(dropout=.0377, width=384, depth=9); Conv(dropout=.0398, filters=23, kernelsize=13, depth=7, maxpoolsize=2); Dense2(depth=0).

For the trials on the data from the lab-constructed float, some additional adjustments to the model parameters were made to optimize the results. The new set of parameters were: Dense1(dropout=0.15, width=384, depth=6), Conv(dropout=0.140, filters=23, kernelsize=13,depth=7,maxpoolsize=2), Dense2(width=185, depth=3).

Preparing and organizing the data for input to the neural network

This study's purpose is to demonstrate the extraction of useful data from the customarily discarded high-frequency components of the data collected by the sensors. Therefore, it was essential to prepare the data carefully such that the high-frequency components are separated from the low-frequency displacement information.

The first experiments were performed on the more recent 2018 data from the commercial TCM-1 unit (Lowell Instruments LLC, North Falmouth, MA 2016). This data was chosen primarily due to the considerable size of the dataset—over 16 million points in six time series lasting a total of 281 hours, or nearly 12 days of data—as compared with less than 2 hours of data from the first experiment. The accelerometer x - and y -axis accelerometer readings were selected as the only input to the ANN model because the vibrations appeared to be most strongly expressed in this data. This choice of inputs made it more straightforward to apply certain data augmentation techniques, as will be shown later.

Note here that when performing the tilt-based calculations, the tilt angle θ can be calculated directly from these same data, using the following formula. Values A_x and A_y are the accelerometer x and y -axis accelerometer readings, respectively:

$$\theta = \arcsin\left(\frac{\sqrt{A_x^2 + A_y^2}}{g}\right) \quad \text{Eqn. 1}$$

To prevent the neural network model training process from simply calibrating itself to infer this relation, it was essential to find an effective method to detrend the data or remove the low frequency and net displacement information. This is important for the data from the commercial TCM-1 unit (Lowell Instruments LLC, North Falmouth, MA 2016)

Two detrending methods were tested, the results of which on the input signal are shown in Figure 12. The first method consists of applying a Savitzky-Golay filter (Savitzky and Golay 1964) to the accelerometer data and subtracting that smoothed data from the original. The second method applies forward differences defined as

$$\Delta S_n \equiv S_{(n+1)} - S_n \quad \text{Eqn. 2}$$

as produced by Python's `numpy.diff()` function (C. R. Harris et al. 2020).

Examination of spectrograms generated from representative data samples before and after the detrending methods were applied revealed that a simple numerical difference applied to the data was preferred. It was very effective at removing the lowest frequencies while at the same time preserving the higher frequency signal. This method was chosen because it requires no windowing of the data, unlike subtracting a smoothed value. Each data point generated is only dependent on immediately adjacent values of the time series.

Creating labeled training inputs

Training, or calibrating, an artificial neural network (ANN) consists of preparing examples of the data in the network's intended domain, along with a label, which is the desired result in the network's intended range. For these experiments, the input to the training mode of the neural network consists of tuples t_i :

$$t_i = (Ax_i, Ay_i, U_i), i \in (1, 2, \dots, N) \quad \text{Eqn. 3}$$

where at each time point i , Ax_i is the data derived from the accelerometer reading parallel to the x -axis, Ay_i is the data derived from the accelerometer reading parallel to the y -axis, and U_i is the corresponding current speed computed using the traditional tilt method. Note that the U_i values were smoothed using a sliding Hann window weighted mean, with a window size of 1024 data points or $1024 / 16\text{Hz} = 64$ seconds. The Hann window was selected due to its favorable spectral characteristics (J. Harris 1978) and its history as applied eponymously to climatological data (Hann and Ward 1903).

A moving window was then used to divide the data stream into potentially overlapping samples s_j of $w = 1024$ data points each, as follows:

$$S_j = (t_{jk}, t_{jk+1}, \dots, t_{jk+w-1}); j \in (0, 1, 2, 3, \dots) \quad \text{Eqn. 4}$$

where j is the sample number, k is the spacing or stride between samples, and w is the window size. Note that the samples overlap when $k < w$. Overlapping of samples is done to provide the neural network with enough samples to train the model effectively. Each sample corresponds to a unique label, so there is no redundancy introduced.

Finally, the labeling was simplified by taking the value of U from the middle of each sample window, or $u_{jk+w/2}$, and used it to label the entire window. Thus, the actual sample inputs to the neural network look like this:

$$S_j = \left[\left[(Ax_{(j.k)}, Ay_{(j.k)}), (Ax_{(j.k)}, Ay_{(j.k)}), \dots, (Ax_{(j.k)}, Ay_{(j.k)}) \right], U_{(j.k)+w/2} \right] \quad \text{Eqn. 5}$$

This process may become more apparent by referring to Figure 13.

Selection of Training Data

The initial experiments with ANN training were performed with the 2018 data using the commercially purchased float. Training and testing data were drawn from separate deployments to increase confidence that the model can infer the current flows from entire deployments previously unseen during training. Because the performance of a neural network model is generally limited by the range of values supplied to it during training (Wu et al. 2018), we selected Deployment 2 because it displayed the broadest range of water current speeds.

However, the current speed distribution was heavily skewed—an attribute shared by all the deployments—with the selected training dataset having a mode of approximately 0.5 cm/s and a median of 4.46 cm/s. This limited the effectiveness of the training because a disproportionate number of samples were clustered near the mode. To improve training quality, sample selection for both training and validation data used a label-leveling scheme. This method divided the label range into ten equally spaced bins, sorted all the samples by label, and selected equal numbers of samples corresponding to each of the ten bins' speed range. This algorithm ensured that the total number of samples chosen required by that training run was correct.

Training and testing the model

The trials documented here were performed using the time series from Deployment 2 as the training data, with a separate time series collected a few weeks later (Deployment 6) serving as the test. This means, briefly, that the training phase used only Deployment 2 data to establish the calibration. The resulting trained network was then used to infer the current speed from the previously unseen data from Deployment 6. These results were then compared with the original tilt-calculated water current speed, and the error was evaluated. This process constitutes one training and testing run.

Evaluation Design

For all trials using the data from the 2018 deployments, an automated script repeated 5 sets of training and testing runs for each sample size of 500, 1000, 1500, 2000, 3000, 4000, 5000, 7500, and 10,000 samples. The model iteratively read through all samples and used the Adam optimizer (Kingma and Ba 2017), a very popular stochastic optimizer based on adaptive moment estimation. The metrics used to evaluate the model's performance against the tilt-calculated speed are root-mean-square error, Pearson's r^2 , and the slope and Y-intercept of a simple linear regression performed on the model results.

Data augmentation

Data augmentation is a tool commonly found in the scientific literature applied to neural network models. (Ferreira et al. 2017; Rashid and Louis 2019). Recently published works specifically using augmented motion sensor data to improve model training data efficiency of vibrational motion include a study of the monitoring of building site construction equipment (Rashid and Louis 2019), and a very well documented study on using human-wearable motion sensors to monitor the symptoms of Parkinson's disease (Um et al. 2017).

In the 2017 Parkinson's study, the authors list several commonly used data augmentation techniques. They all involve transforming the data in space, time, or both, to enrich the domain of data available to train the model. This enrichment is accomplished by applying such transformations in ways that anticipate possible inputs that could have been encountered by the system without changing the labeling of the data.

In the case of Parkinson's patients, there is sufficient variation in amplitude and frequency of such symptoms as tremor among the patients' population to allow transformations in both time and space domains to be applied without changing labels. However, this study's labeling is by water current speed, a scalar value, and not a classification. As established by Strouhal, Von Karman, and Vonnegut (Strouhal 1878; Von Karman 1911; Vonnegut 1957), among others, one of the most important flow-induced phenomena driving the results—vortex shedding—varies in frequency with the water current speed. Therefore, the temporal transformations applied there were deemed not immediately applicable to this work. However, two important spatial transformations, reflection and rotation, have proven very useful.

For this immediate problem, recalling Figure 6, which depicts the commercial TCM unit's physical construction and sensor placement, note that its external shell is cylindrical and thus symmetric about its center axis. Also, note that the sensor is installed with its z-axis is parallel to the center axis of the float package. In practice, this means two things. First, the float will respond, for all practical purposes, identically to a water current regardless of the direction

the current is passing around the float. Second, unless the package is carefully marked and deployed, it would not be easy to control the float's actual orientation with respect to a desired rotational frame of reference. For example, the float at rest in still water might have the sensor package oriented with its x-axis pointing north for one deployment, southeast for the next, and so on. The float may even move about slightly if the anchor is not quite heavy enough or if especially rough conditions are experienced.

Therefore, any piece of data recorded by this sensor system can be rotated about the z-axis mathematically and represent a set of readings that could have occurred, and still represent the same speed reading as the original raw data.

Similarly, the cylindrical package is also symmetric about the z-axis. So input can also be reflected or flipped about any axis perpendicular to the z-axis and be identically labeled as the untransformed raw data. Please refer to Figure 14 for diagrams graphically depicting the two forms of data augmentation.

Reflection, which exploits the symmetry property, was performed first, as it is the simplest, both conceptually and computationally. The scripts simply changed the sign of the sensor readings from the x-axis sensor to produce one additional set of augmented training inputs; and then similarly changed the sign of the y-axis sensor readings. This process tripled the number of data samples presented to the ANN for training without increasing the number of raw samples needed.

Following the application of reflection, the rotational symmetry was exploited as follows: for all original and symmetrically augmented samples, the system applied the following formula to obtain a series of samples rotated through a series of angles about the z-axis, which is the origin on the x-y plane.

For each set of observations (x_i, y_i, u_i) representing the accelerometer readings along the x and y axes respectively, labeled as representing the labeled water current speed u , an augmented training point $(x_{\theta_i}, y_{\theta_i}, u_i)$ was created, where

$$\begin{aligned} x_{\theta_i} &= x_i \cos(\theta) - y_i \sin(\theta) \\ y_{\theta_i} &= y_i \cos(\theta) + x_i \sin(\theta) \end{aligned} \tag{Eqn. 6}$$

which represents the original point rotated about the origin $(0, 0)$ by the angle θ . The rotational angle intervals used are shown in **Table 3**.

Rotational Scheme	Enumeration of rotational angles applied	Factor increase in samples
rot(60)	(60, 120, 180, 240, 300)	6x
rot(40)	(40, 80, 120, 160, 200, 240, 280, 320)	9x
rot(20)	(20, 40, 60, 80, 100, 120, 140, 160, 180, 200, 220, 240, 260, 280, 300, 320, 340)	18x

Table 3. Rotational angles are used to create "augmented" samples for ANN training.

Analysis of Lab-Constructed Prototype Data

Compared with the 2018 data, the 2015 data is an almost unimaginably tiny dataset. Containing only 10,301 data points spanning only 85 minutes, it is only 0.0006 of the data points and only 0.0051 of the deployment time.

A review of the lab-constructed floats' construction reveals that it shares the cylindrical shape, and thus the reflective and rotational symmetry, of the commercial TCM system.

In contrast with the previous experiments, the x- and y-axis gyroscope data (not available on the commercial unit) was used instead of the x- and y-axis accelerometer values, simply because better results were obtained. Also, due to the nature of the gyroscope data, which is recorded in degrees of rotation per second, no detrending of the data was required.

Another important difference is that all data labeling, and evaluation of results, was accomplished using readings from an acoustic doppler current profiler (a Nortek ADCP) deployed within a few meters of the floats., which recorded the data simultaneously during the deployments.

Data from one of the deployments, *Float 1*, labeled with the ADCP data, was used to train a neural network of the identical design as used in the previous experiment. The trained model then read the raw data produced by a second nearby but physically independent float (*Float 2*) to predict the current readings. These predictions are then compared to the original ADCP data. The flow of information is depicted in Figure 15.

As with the previous experiment, the data from one of the floats designated *Float 1* was divided into a series of an increasing number of samples: 300, 500, 1000, 2000, 3000, and 4000. Each data sample was 512 data points / 2 Hz= 256 seconds or about 4.2 minutes. The readings from the ADCP were smoothed over that same 512 datapoint window using a moving average Hann-weighted scheme identical to the previous experiment.

The calculations were performed using two rotational densities: 30 and 40 degrees.

Rotational Scheme	Enumeration of rotational angles applied for lab-built float	Factor increase in samples
rot(30)	(30, 60, 90, 120, 150, 180, 210, 240, 270, 300, 330)	12x
rot(40)	(40, 80, 120, 160, 200, 240, 280, 320)	9x

Table 4. Rotational angles are used to create "augmented" samples for ANN training.

Results and Discussion

Baseline performance without data augmentation

The results were very promising. The model converged consistently and gave good results at higher numbers of samples (4,000 and higher), showed very inconsistent performance at 3000, displayed a clear inflection point across all chosen metrics, and failed to converge at 2,000 fewer samples. This shows that the data preparation paradigm used here had served as a realistic testbed to help identify calibration methods that may be generalizable to other, much more challenging applications. The results were as shown in Figure 16.

Results using reflective data augmentation

These results (Figure 17) clearly show the benefits of data augmentation for this application. The previous set of training runs required 4000 raw data samples from the sensors to achieve consistent convergence and reasonable results. By simply inverting the readings about each of the x- and y-axes in turn and supplying those transformed samples as additional inputs to the model training, the training efficiency has increased by nearly a factor of three: Instead of requiring 4000 samples to achieve meaningful calibration, training with data augmentation converges, and testing results quickly improve with only 1000 samples, a 4-fold reduction in the number of samples required. Note that, to provide a better range of samples due to increased efficiency observed in these data-augmented trials, the model was trained using 5 repeated trials each at sample quantities of 100, 200, 300, and 400 samples in addition to the higher quantities already noted.

Results with both reflective and rotational data augmentation applied

With these results, charted in Figure 18, consistent model behavior was observed when training with as few as 300 original samples. Compared to the requirement of at least 4000 samples when data augmentation is not used, this represents a *13-fold increase* in training efficiency.

Results from lab-constructed floats

With the considerable power of data augmentation having proved itself in the somewhat contrived testbed environment, the earlier 2015 deployment data were analyzed similarly. Compared with the 2018 data, the 2015 data

is an almost unimaginably tiny dataset. Containing only 10,301 data points spanning only 85 minutes, it is only 0.0006 of the data points and only 0.0051 of the deployment time.

The results metrics are shown in Figure 19. A demonstration of the model's performance is charted in a labeled scatterplot in Figure 20. A direct time-series plot of ADCP measurements overplotted with the model's output is shown in Figure 21. The ANN model produced data that correlated with the actual ADCP measurements quite well. The final chart shows an r^2 of .96 and an overall RMSe of 6.03 cm/s from a range of 40-140 cm/s.

Discussion

The last experiment's results were computed using data from three completely physically separate and independent devices, using the same methodology as our initial proof-of-concept. As compared with the new Lowell TCM device, these homemade floats were a less stable design, were much larger and had a bulkier form factor, recorded data at $\frac{1}{8}$ the sampling rate, and were only deployed for 85 *minutes*. Yet, given the data from a previously unseen device, in a slightly different location, and likely with variations in its construction due to its homemade nature, the ANN model produced data that correlated with the actual ADCP measurements quite well. The final chart shows an r^2 of .96, an overall RMSe of 6.03 cm/s from a range of 40-140 cm/s.

I believe these results demonstrate that this general technique and approach can enable researchers to obtain meaningful current flow readings from even less expensive devices than are now available.

Conclusions

Major, firm discoveries

The methods described in this paper demonstrate a technique to extend the current speed measuring power of an ADCP with the deployment of very low-cost assemblies. This technique works well when similar assemblies are deployed in similar locations and may very well generalize to a wider variety of deployment locations, such as nearshore swash zones, very deep or shallow waters.

Limitations

What has not been thoroughly studied to date is whether a neural network model trained on the data from a particular subsurface float design can generalize to substantially different locations. Even a difference in bottom character could potentially affect the results. A subsurface float deployed near a bottom covered in a large rocky substrate will likely experience a more turbulent boundary layer, affecting the nature and character of the flow-induced vibrations experienced by the float assembly.

However, this limitation can be overcome by training a new neural network model at each deployment location. As long as the ADCP is deployed at each location long enough to capture a sufficient range of current speeds, a neural network model can be trained for each deployment. If each deployment only requires the ADCP to be in its vicinity for 10% of the deployment time to achieve good convergence of its corresponding network model, it would allow the current speed to be measured at 10 locations with only one ADCP. Of course, it would require each site to be visited twice; however, these visits could safely be distributed throughout the study's time period. This is because a trained network model can infer the current from vibrational data collected before the training as well as after, as long as it is the same float in the same location.

Interesting future research questions

The initial observations in this study lead to many interesting research questions moving forward. As noted in the introduction, to date, the designs of subsurface structures subject to water currents have been almost exclusively focused on controlling, limiting, or eliminating vortex shedding phenomena. Does purposely increasing the number of vortex-shedding modes exhibited by a body increase its efficacy in this new paradigm? Despite the ability of ANNs to make sense of such complexity, does a system that is limited in the number of vortexshedding modes it can exhibit always give better results than systems that exhibit more complex behavior? And finally, are these results generalizable to a larger variety of locations and instrument types than shown in these experiments?

Bibliography

- Abadi, M., Barham, P., Chen, J., Chen, Z., Davis, A., Dean, J., et al. (2016). Tensorflow: A system for large-scale machine learning. In *12th USENIX Symposium on Operating Systems Design and Implementation (OSDI 16)* (pp. 265–283).
- Albaladejo, C., Sánchez, P., Iborra, A., Soto, F., López, J. A., & Torres, R. (2010). Wireless Sensor Networks for Oceanographic Monitoring: A Systematic Review. *Sensors (Basel, Switzerland)*, *10*(7), 6948–6968.
<https://doi.org/10.3390/s100706948>
- Allen, D. W., & Hening, D. L. (2002). Ultrashort fairings for suppressing vortex-induced-vibration. *The Journal of the Acoustical Society of America*, *111*(3), 1151. <https://doi.org/10.1121/1.1469283>
- Anaconda Inc. (2020). *Anaconda Software Distribution. Anaconda Documentation*. Anaconda Inc.
<https://docs.anaconda.com/>
- Anarde, K., & Figlus, J. (2017). TILT CURRENT METERS IN THE SURF ZONE: BENCHMARKING UTILITY IN HIGH-FREQUENCY OSCILLATORY FLOW. *Coastal Dynamics*, (050), 11.
- Beltaos, S. (2012). Mackenzie Delta flow during spring breakup: uncertainties and potential improvements. *Canadian Journal of Civil Engineering*, *39*(5), 579–588. <https://doi.org/10.1139/l2012-033>
- Bergstra, J. S., Bardenet, R., Bengio, Y., & Kégl, B. (2011). Algorithms for Hyper-Parameter Optimization. In J. Shawe-Taylor, R. S. Zemel, P. L. Bartlett, F. Pereira, & K. Q. Weinberger (Eds.), *Advances in Neural Information Processing Systems 24* (pp. 2546–2554). Curran Associates, Inc.
<http://papers.nips.cc/paper/4443-algorithms-for-hyper-parameter-optimization.pdf>. Accessed 29 March 2020
- Chen, Y.-C., Hong, D. J.-K., Wu, C.-W., & Mupparapu, M. (2019). The Use of Deep Convolutional Neural Networks in Biomedical Imaging: A Review. *Journal of Orofacial Sciences*, *11*(1), 3.
https://doi.org/10.4103/jofs.jofs_55_19
- Ferreira, J., Ferro, M., Fernandes, B., Valenca, M., Bastos-Filho, C., & Barros, P. (2017). Extreme learning machine autoencoder for data augmentation. In *2017 IEEE Latin American Conference on Computational Intelligence (LA-CCI)* (pp. 1–6). Presented at the 2017 IEEE Latin American Conference on Computational Intelligence (LA-CCI). <https://doi.org/10.1109/LA-CCI.2017.8285702>

- Figuerski, J. D., Malone, D., Lacy, J. R., & Denny, M. (2011). An inexpensive instrument for measuring wave exposure and water velocity: Measuring wave exposure inexpensively. *Limnology and Oceanography: Methods*, 9(5), 204–214. <https://doi.org/10.4319/lom.2011.9.204>
- Fridrich, M. (2017). Hyperparameter Optimization of Artificial Neural Network in Customer Churn Prediction using Genetic Algorithm. *Trends Economics and Management*, 11(28), 9-21–21. <https://doi.org/10.13164/trends.2017.28.9>
- Fussell, T. (1973, May 15). Bluff body flowmeter with internal sensor. <http://www.google.com/patents/US3732731>. Accessed 4 January 2018
- Gholamiangonabadi, D., Kiselov, N., & Grolinger, K. (2020). Deep Neural Networks for Human Activity Recognition With Wearable Sensors: Leave-One-Subject-Out Cross-Validation for Model Selection. *IEEE Access*, 8, 133982–133994. Presented at the IEEE Access. <https://doi.org/10.1109/ACCESS.2020.3010715>
- Gomes, R. M. F., Sousa, J. B., & Pereira, F. L. (2003). Modeling and control of the IES project ROV. In 2003 *European Control Conference (ECC)* (pp. 3424–3429). Presented at the 2003 European Control Conference (ECC). <https://doi.org/10.23919/ECC.2003.7086570>
- Hann, J. von, & Ward, R. D. (1903). *Handbook of climatology*. New York, The Macmillan company; London, Macmillan & co., ltd. <http://archive.org/details/handbookclimato01wardgoog>. Accessed 16 August 2020
- Harris, C. R., Millman, K. J., Walt, S. J. van der, Gommers, R., Virtanen, P., Cournapeau, D., et al. (2020). Array programming with NumPy. *Nature*, 585(7825), 357–362. <https://doi.org/10.1038/s41586-020-2649-2>
- Harris, J. (1978). On the Use of Windows for Harmonic Analysis with the Discrete Fourier Transform. *Proceedings of the IEEE*, 66(1), 33.
- Hoerner, S. F. (1965). *Fluid-Dynamic Drag* (2nd ed.). Midland Park, NJ: Hoerner Fluid Dynamics.
- Hokimoto, T. (2012). Prediction of Wave Height Based on the Monitoring of Surface Wind. In M. Marcelli (Ed.), *Oceanography*. InTech. <https://doi.org/10.5772/27278>
- Hondoh, M., Wada, M., Andoh, T., & Kurornori, K. (2001). A vortex flowmeter with spectral analysis signal processing. In *SIcon/01. Sensors for Industry Conference. Proceedings of the First ISA/IEEE. Sensors for Industry Conference (Cat. No.01EX459)* (pp. 35–40). Presented at the SIcon/01. Sensors for Industry Conference. First ISA/IEEE Sensors for Industry Conference, Rosemont, IL, USA: IEEE. <https://doi.org/10.1109/SFICON.2001.968495>

- Houghton, C. J., Bronte, C. R., Paddock, R. W., & Janssen, J. (2010). Evidence for allochthonous prey delivery to Lake Michigan's Mid-Lake Reef Complex: Are deep reefs analogs to oceanic sea mounts? *Journal of Great Lakes Research*, 36(4), 666–673. <https://doi.org/10.1016/j.jglr.2010.07.003>
- House, L. B. (1987). *SIMULATION OF UNSTEADY FLOW IN THE MILWAUKEE HARBOR ESTUARY AT MILWAUKEE, WISCONSIN* (Water-Resources Investigations Report No. 86–4050) (p. 25). Madison, Wisconsin: US Geological Survey. <https://pubs.usgs.gov/wri/1986/4050/report.pdf>. Accessed 17 August 2018
- Ippolito, P. P. (2020, February). Practical Hyperparameter Optimization. *KDnuggets News*. Industry. <https://www.kdnuggets.com/2020/02/practical-hyperparameter-optimization.html>. Accessed 30 March 2020
- Johansen, J. L. (2014). Quantifying Water Flow within Aquatic Ecosystems Using Load Cell Sensors: A Profile of Currents Experienced by Coral Reef Organisms around Lizard Island, Great Barrier Reef, Australia. *PLoS ONE*, 9(1), e83240. <https://doi.org/10.1371/journal.pone.0083240>
- Johnstone, A. D., & Stappenbelt, B. (2016). Flow-induced vibration characteristics of pivoted cylinders with splitter-plates. *Australian Journal of Mechanical Engineering*, 14(1), 53–63. <https://doi.org/10.1080/14484846.2015.1093219>
- Kamil, M., Chobtrong, T., Günes, E., & Haid, M. (2014). Low-cost object tracking with MEMS sensors, Kalman filtering and simplified two-filter-smoothing. *Applied Mathematics and Computation*, 235, 323–331. <https://doi.org/10.1016/j.amc.2014.03.015>
- Kingma, D. P., & Ba, J. (2017). Adam: A Method for Stochastic Optimization. *arXiv:1412.6980 [cs]*. <http://arxiv.org/abs/1412.6980>. Accessed 30 November 2020
- Lowell Instruments LLC, North Falmouth, MA. (2016). *TCM-1 Tilt Current Meter*. North Falmouth, MA. <http://lowellinstruments.com/products/tcm-1-tilt-current-meter/>. Accessed 31 January 2017
- Lowell Instruments LLC, North Falmouth, MA. (2017, January). Universal User Guide for TCM-x Current Meters, MAT-1 Data Logger and MAT Logger Commander Software. Lowell Instruments, Inc., North Falmouth, MA. <http://lowellinstruments.com/products/tcm-1-tilt-current-meter/>. Accessed 31 January 2017
- Lowell, N. S., Walsh, D. R., & Pohlman, J. W. (2015). A comparison of tilt current meters and an acoustic doppler current meter in vineyard sound, Massachusetts. In *2015 IEEE/OES Eleventh Current, Waves and Turbulence*

- Measurement (CWTM)* (pp. 1–7). Presented at the 2015 IEEE/OES Eleventh Current, Waves and Turbulence Measurement (CWTM). <https://doi.org/10.1109/CWTM.2015.7098135>
- Marble, E., Morton, C., & Yarusevych, S. (2018). Vortex dynamics in the wake of a pivoted cylinder undergoing vortex-induced vibrations with elliptic trajectories. *Experiments in Fluids*, 59(5), 78. <https://doi.org/10.1007/s00348-018-2530-3>
- Mathur, A., Zhang, T., Bhattacharya, S., Velickovic, P., Joffe, L., Lane, N. D., et al. (2018). Using Deep Data Augmentation Training to Address Software and Hardware Heterogeneities in Wearable and Smartphone Sensing Devices. In *2018 17th ACM/IEEE International Conference on Information Processing in Sensor Networks (IPSN)* (pp. 200–211). Presented at the 2018 17th ACM/IEEE International Conference on Information Processing in Sensor Networks (IPSN), Porto: IEEE. <https://doi.org/10.1109/IPSN.2018.00048>
- McMurtree Charles, L., & Rodely Alan, E. (1971, June 28). Differential sensor bluff body flowmeter. <http://www.google.com/patents/US3587312>. Accessed 4 January 2018
- Mortimer, C. H. (2004). *Lake Michigan in Motion: Responses of an Inland Sea to Weather, Earth-spin, and Human Activities*. Univ of Wisconsin Press.
- Morton, J., Witherden, F. D., Jameson, A., & Kochenderfer, M. J. (2018). Deep Dynamical Modeling and Control of Unsteady Fluid Flows. *arXiv:1805.07472 [cs]*. <http://arxiv.org/abs/1805.07472>. Accessed 8 April 2019
- Orive, D., Sorrosal, G., Borges, C. E., Martin, C., & Alonso-Vicario, A. (2014). EVOLUTIONARY ALGORITHMS FOR HYPERPARAMETER TUNING ON NEURAL NETWORKS MODELS, 8.
- Pant, N. (2018). *Hyper-Optimized Machine Learning and Deep Learning Methods for Geo-Spatial and Temporal Function Estimation* (Ph.D.). The University of Texas at Arlington, United States -- Texas. Retrieved from <http://search.proquest.com/docview/2314065307/abstract/D8EFA13BC9A44414PQ/1>
- Raissi, M., Yazdani, A., & Karniadakis, G. E. (2018). Hidden Fluid Mechanics: A Navier-Stokes Informed Deep Learning Framework for Assimilating Flow Visualization Data. *arXiv:1808.04327 [physics, stat]*. <http://arxiv.org/abs/1808.04327>. Accessed 13 April 2019
- Rashid, K. M., & Louis, J. (2019). Times-series data augmentation and deep learning for construction equipment activity recognition. *Advanced Engineering Informatics*, 42, 100944. <https://doi.org/10.1016/j.aei.2019.100944>

- Santoso, D. R., Maryanto, S., & Nadhir, A. (2015). Application of Single MEMS-Accelerometer to Measure 3-Axis Vibrations and 2-Axis Tilt-Angle Simultaneously. *Telkomnika*, 13(2), 442–450.
<https://doi.org/10.12928/TELKOMNIKA.v13i2.1490>
- Savitzky, A., & Golay, M. J. E. (1964). Smoothing and Differentiation of Data by Simplified Least Squares Procedures. *Analytical chemistry (Washington)*, 36(8), 1627–1639.
- Sayer, P. (1996). Hydrodynamic Forces On ROVs Near the Air-Sea Interface. *International Journal of Offshore and Polar Engineering*, 6(03). <https://www.onepetro.org/journal-paper/ISOPE-96-06-3-177>. Accessed 22 July 2019
- Sejnowski, T. J. (2020). The unreasonable effectiveness of deep learning in artificial intelligence. *Proceedings of the National Academy of Sciences*. <https://doi.org/10.1073/pnas.1907373117>
- Sheremet, V. A. (2009). *Observations of Near-Bottom Currents With Low-Cost SeaHorse Tilt Current Meters*: Fort Belvoir, VA: Defense Technical Information Center. <https://doi.org/10.21236/ADA531856>
- Sieyes, N. R. de, Yamahara, K. M., Layton, B. A., Joyce, E. H., & Boehm, A. B. (2008). Submarine Discharge of Nutrient-Enriched Fresh Groundwater at Stinson Beach, California Is Enhanced during Neap Tides. *Limnology and Oceanography*, 53(4), 1434–1445. <https://doi.org/10.2307/40058264>
- Strouhal, V. (1878). Ueber eine besondere Art der Tonerregung. *Annalen der Physik*, 241(10), 216–251.
<https://doi.org/10.1002/andp.18782411005>
- Thuerey, N., & Xiangyu, H. (2018, October 18). Deep Learning Methods for Reynolds-Averaged Navier-Stokes Simulations. Technical University of Munich. <https://doi.org/10.14459/2018mp1459172>
- Um, T. T., Pfister, F. M. J., Pichler, D., Endo, S., Lang, M., Hirche, S., et al. (2017). Data Augmentation of Wearable Sensor Data for Parkinson's Disease Monitoring using Convolutional Neural Networks. *Proceedings of the 19th ACM International Conference on Multimodal Interaction - ICMI 2017*, 216–220.
<https://doi.org/10.1145/3136755.3136817>
- Van Rossum, G., & Drake, F. L. (2009). *Python 3 Reference Manual*. Scotts Valley, CA: CreateSpace.
- Vasyukov, S. A., Ostapenko, D. G., & Avdeeva, T. V. (2014). Experimental Study of the Information Signal of Combined Shock, Tilt, and Motion Sensor Based on the 3-Axis MEMS-Accelerometer. *Nauka i Obrazovanie*, 0(10), 209–229.

- Venugopal, A., Agrawal, A., & Prabhu, S. V. (2011). Review on vortex flowmeter—Designer perspective. *Sensors and Actuators A: Physical*, 170(1–2), 8–23. <https://doi.org/10.1016/j.sna.2011.05.034>
- Von Karman, T. (1911). Über den Mechanismus des Widerstandes, den ein bewegter Körper in einer Flüssigkeit erfährt. *Nachrichten von der Gesellschaft der Wissenschaften zu Göttingen, Mathematisch-Physikalische Klasse*, 1911, 509–517.
- Vonnegut, B. (1957, June 4). Vortex whistle measuring instrument for fluid flow rates and/or pressure [U.S. Patent No. US2794341A]. <http://www.google.com/patents/US2794341>. Accessed 4 January 2018
- Wang, J.-X., Wu, J., Ling, J., Iaccarino, G., & Xiao, H. (2018). A Comprehensive Physics-Informed Machine Learning Framework for Predictive Turbulence Modeling. *Physical Review Fluids*, 3(7), 074602. <https://doi.org/10.1103/PhysRevFluids.3.074602>
- Wu, Y., Rivenson, Y., Zhang, Y., Wei, Z., Günaydin, H., Lin, X., & Ozcan, A. (2018). Extended depth-of-field in holographic imaging using deep-learning-based autofocusing and phase recovery. *Optica*, 5(6), 704–710. <https://doi.org/10.1364/OPTICA.5.000704>
- Xu, K.-J., Zhu, Z.-H., Zhou, Y., Wang, X.-F., Liu, S.-S., Huang, Y.-Z., & Chen, Z.-Y. (2009). Applied digital signal processing systems for vortex flowmeter with digital signal processing. *Review of Scientific Instruments*, 80(2), 025104. <https://doi.org/10.1063/1.3082044>
- Zahari, M. A., & Dol, S. S. (2014). Application of Vortex Induced Vibration Energy Generation Technologies to the Offshore Oil and Gas Platform: The Preliminary Study, 8(7), 4.
- Zhang, W., Qin, L., Zhong, W., Guo, X., & Wang, G. (2019). Framework of Sequence Chunking for Human Activity Recognition Using Wearables. In *Proceedings of the 2019 International Conference on Image, Video and Signal Processing - IVSP 2019* (pp. 93–98). Presented at the the 2019 International Conference, Shanghai, China: ACM Press. <https://doi.org/10.1145/3317640.3317647>

List of Figures and Captions

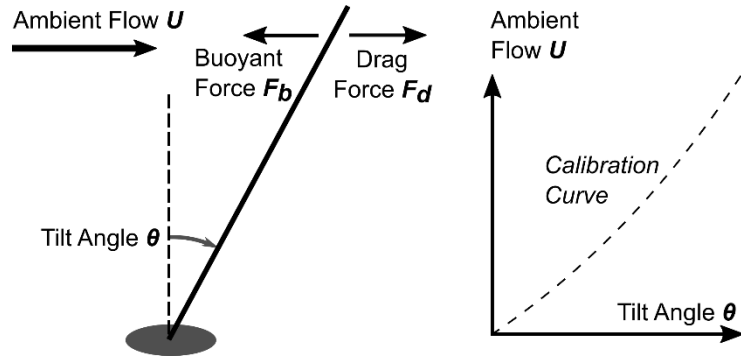


Figure 2. A schematic diagram demonstrating the principles of operation of the tilt current meter. The software included with the device first calculates the time-averaged tilt angle experienced by the unit. It then uses a calibration table to determine the speed of the ambient current. *Source: diagram drawn by the author from documentation provided by the manufacturer.* (Lowell Instruments LLC, North Falmouth, MA 2017) as well as background information from Figurski et al. (2011)

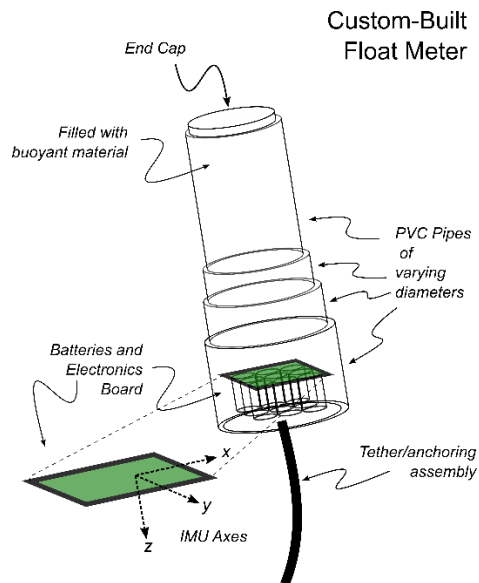


Figure 3. Diagram of custom-built float (not to scale)
 Designed and built by Matthew Smith, Ph.D., 2015.

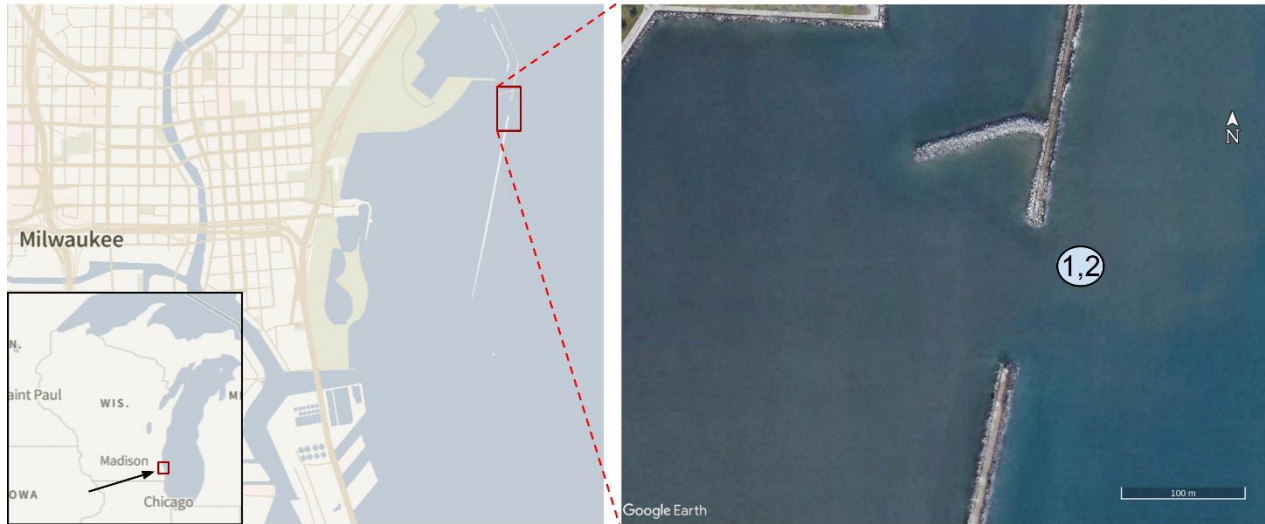


Figure 4. Map of the deployment area. Map/imagery: Mapbox (left); Google Earth (right)

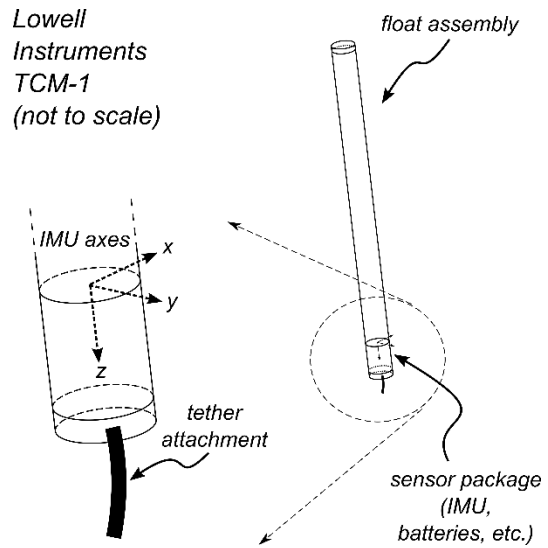


Figure 5. The orientation of accelerometer and magnetometer sensor axes on the TCM instrumented float. Please note that this is a simplified schematic. *Source: drawn by the author from direct observation and information in the TCM-1 manual (Lowell Instruments LLC, North Falmouth, MA 2017)*



Figure 6. Map of the deployment area. *Map/imagery: Mapbox (left); Google Earth (right)*

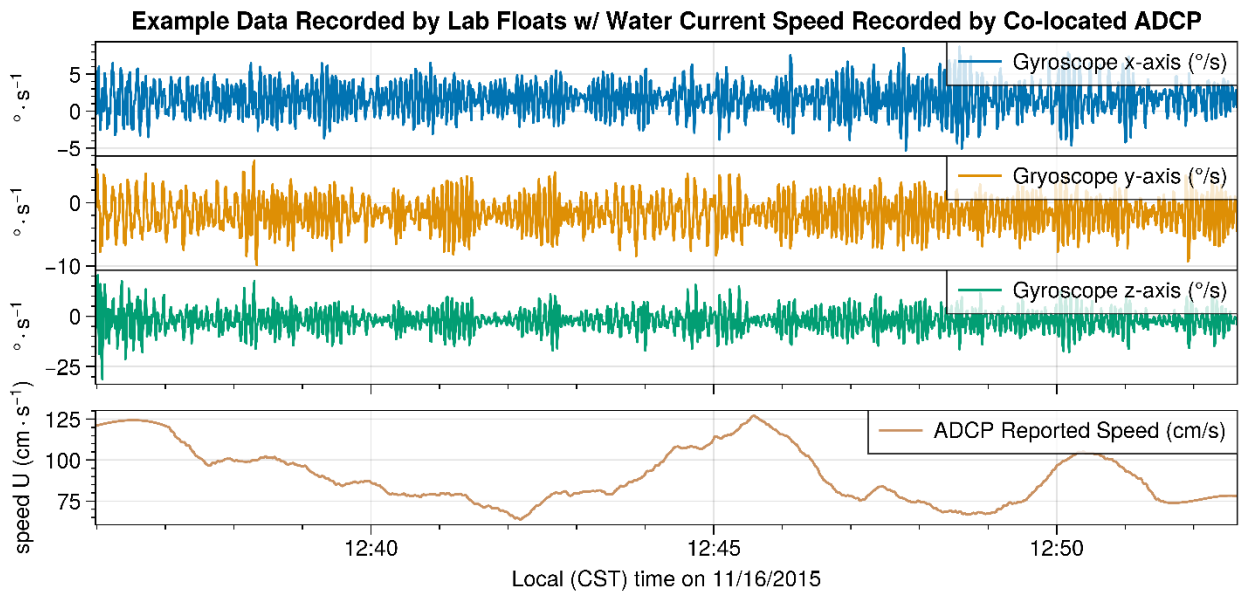


Figure 7. Example data from lab-constructed float assembly.

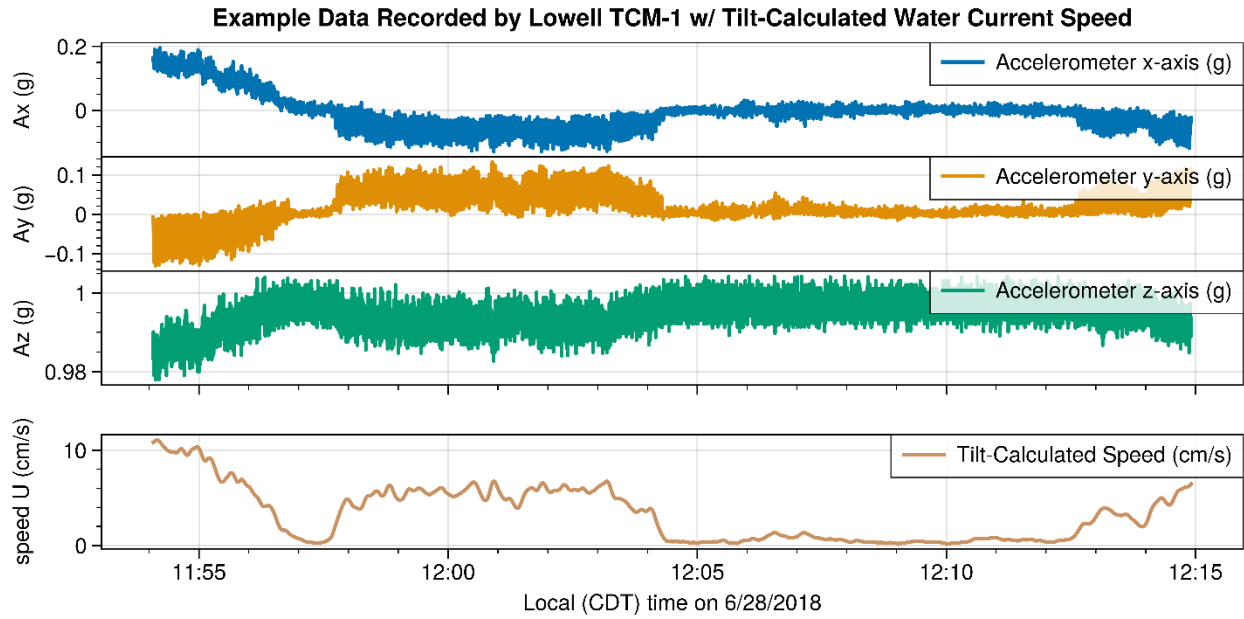


Figure 8. Depicted here are the raw time series readings from the accelerometer x, y, and z-axis sensors. (Note: signals from the x- and y-axes were sufficient to train the ANN; the z-axis data was not used in training.)

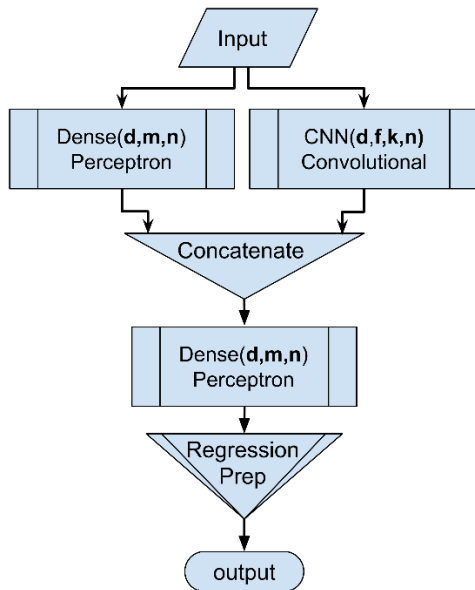


Figure 9. Schematic Diagram of experimental ANN used in this work. (Created by the author)

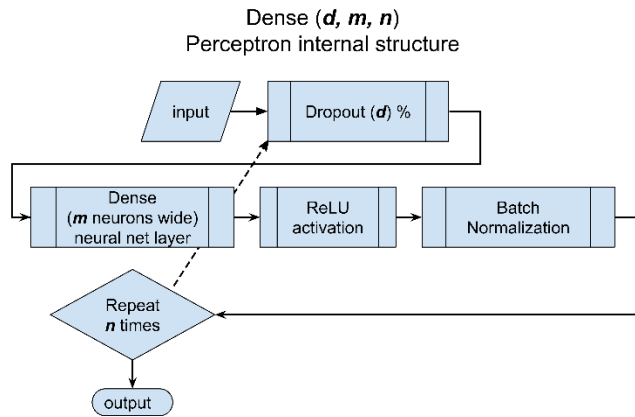


Figure 10. Dense Perceptron internal structure *(drawing created by the author)*

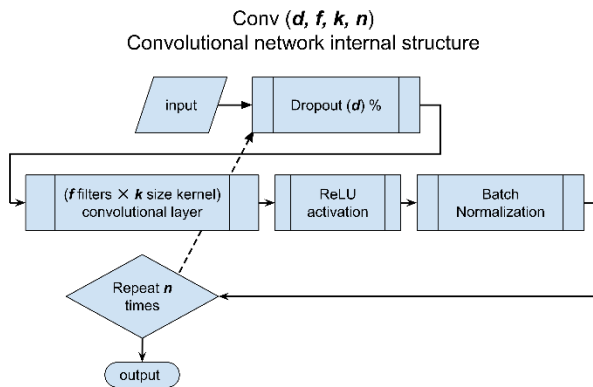


Figure 11. The design of the CNN sub-network *(drawing by the author)*

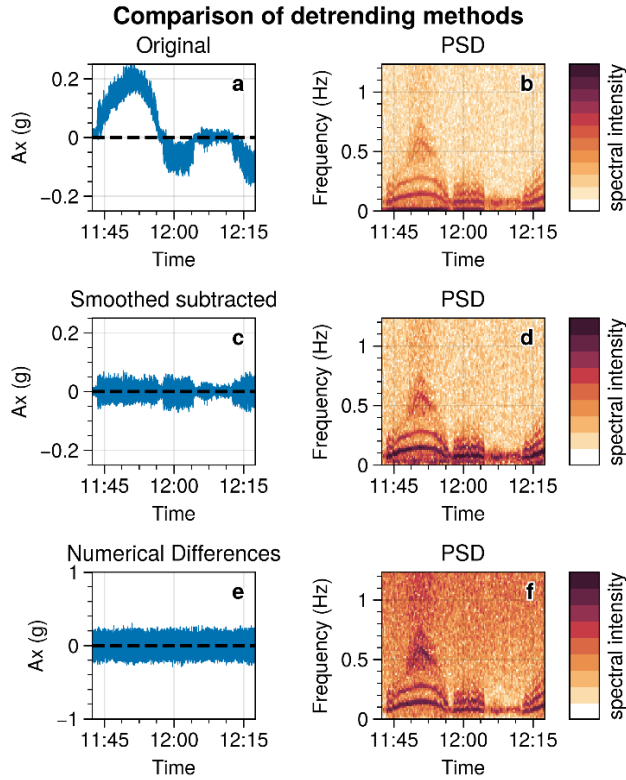


Figure 12. **a.** Original data from accelerometer x-axis sensor plotted as a time series signal; **b.** Partial spectrogram of the original signal; **c.** The original signal with a Savitsky-Golay filtered version subtracted; **d.** the spectrogram of (c); **e.** a very simple numerical differencing produced by applying the Python `numpy.diff()` function (see text) to the original data; **f.** the spectrogram of (e).

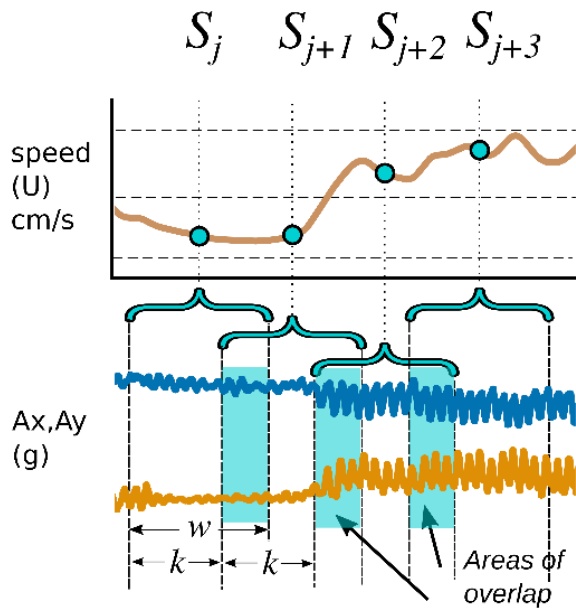


Figure 13. Each sample of w data points is associated with a single-speed calculation corresponding to the sample's midpoint.

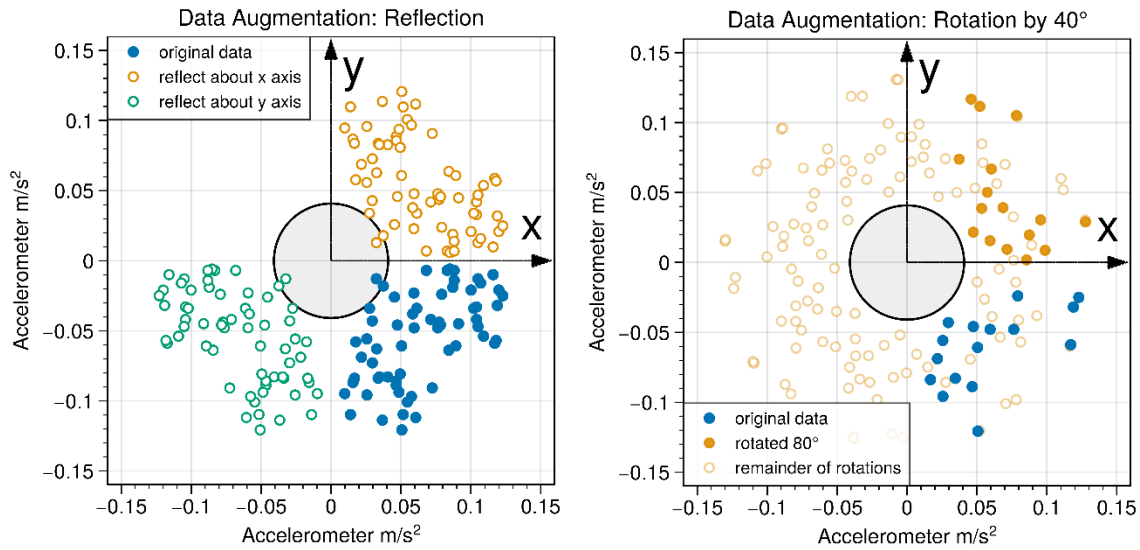


Figure 14. (left) graphically shows accelerometer readings reflected about the x and y axes; (right) showing accelerometer readings rotated by 40 degrees around the origin. The data is rotated by 40, 80, 120, 160, 200, 240, 280, and 320 degrees. The 80-degree rotation is highlighted just to illustrate how the rotation works.

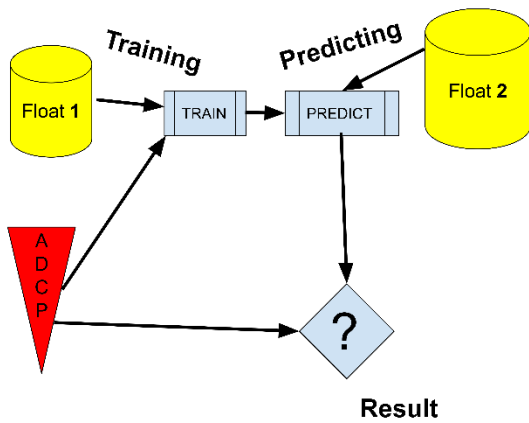


Figure 15. Schematic of information flow

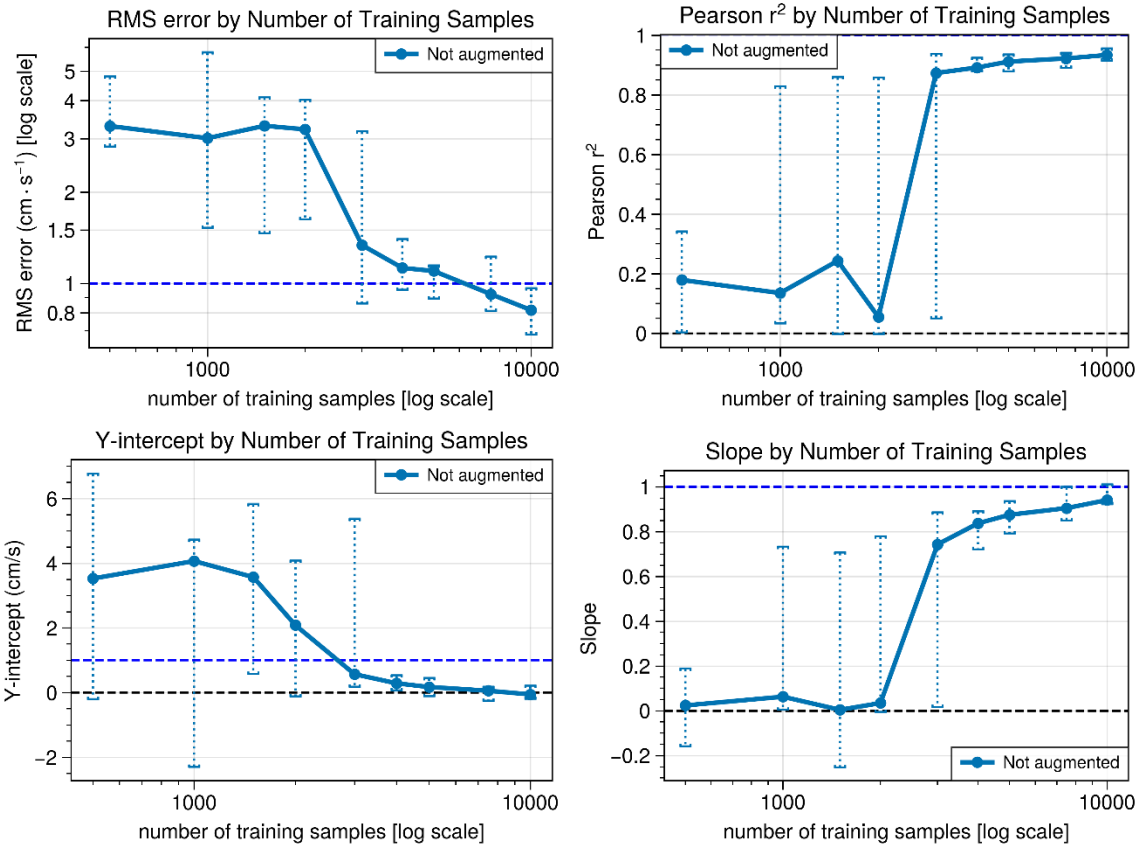


Figure 16. The initial set of baseline results evaluated by the following metrics: **(a)** Root-mean-squared error (RMSe), **(b)** Pearson's r^2 ; **(c)** slope, and **(d)** Y-intercept. The markers and lines represent the evaluation metric's median values from 5 trial runs performed at each sample level for all four charts. The error bars represent the maximum and minimum values of the evaluation metric.

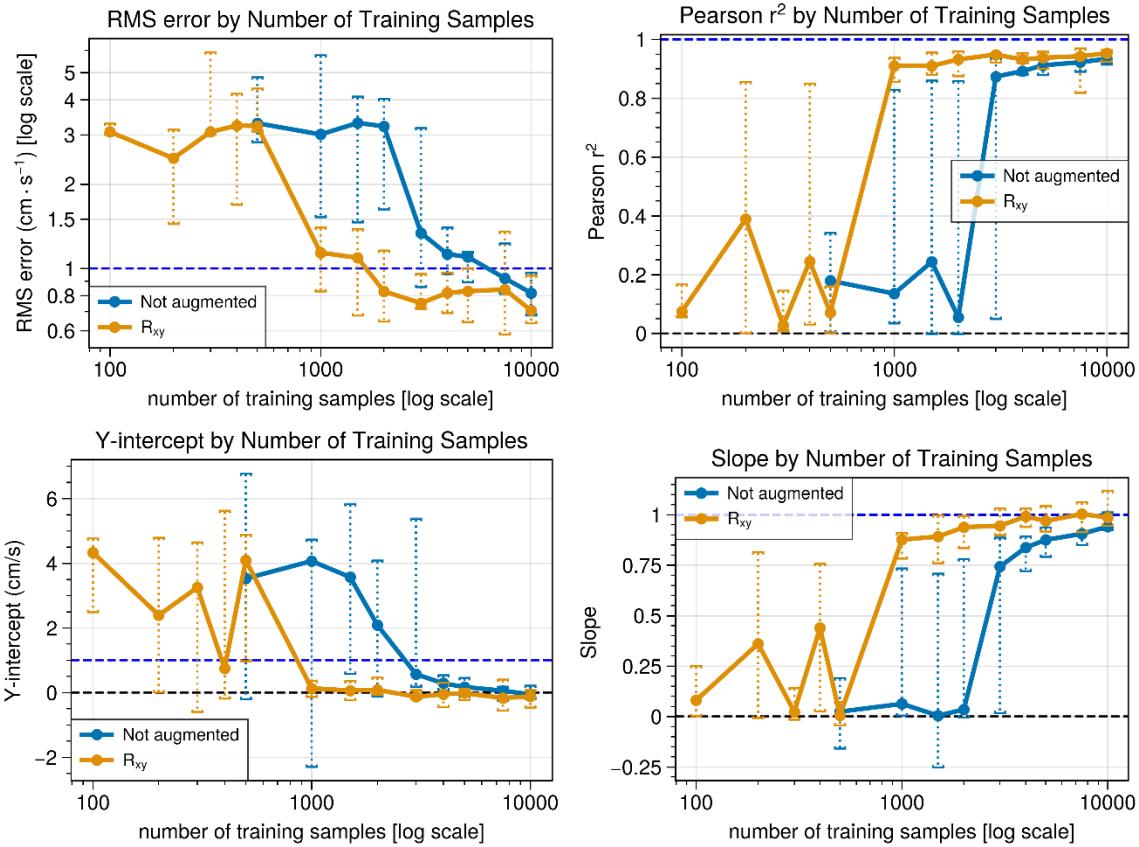


Figure 17. Results of model training on original samples plus the augmented reflected data samples. Once again, each data point represents the median of 5 complete training/testing cycles, with the error bars representing the minimum and maximum values of the corresponding metric.

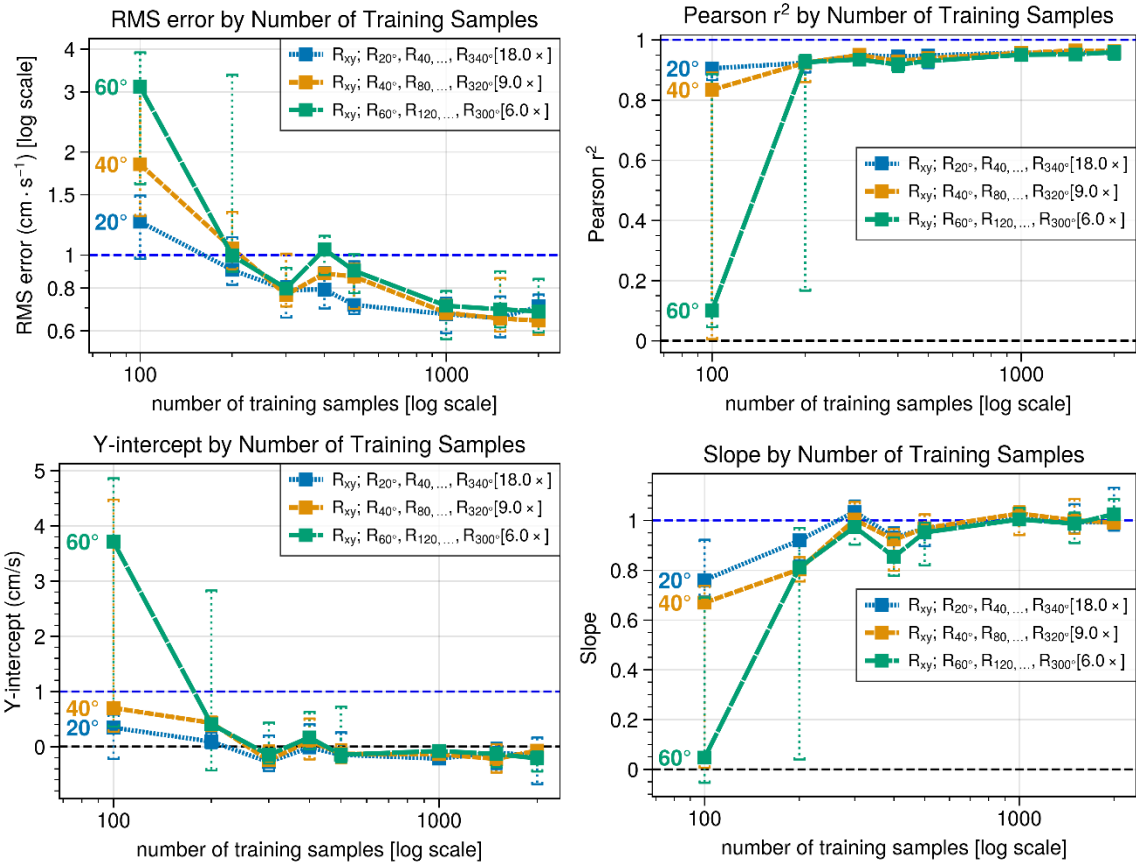


Figure 18. The results of rotating the original plus the reflected samples through 20, 40, and 60 degree series of angles through all 360 degrees (with 0 and 360 omitted because they would be identical to the original). Each data point shown represents the median of 5 separate training/testing runs, and the error bars show the minimum and maximum results obtained for the metric.

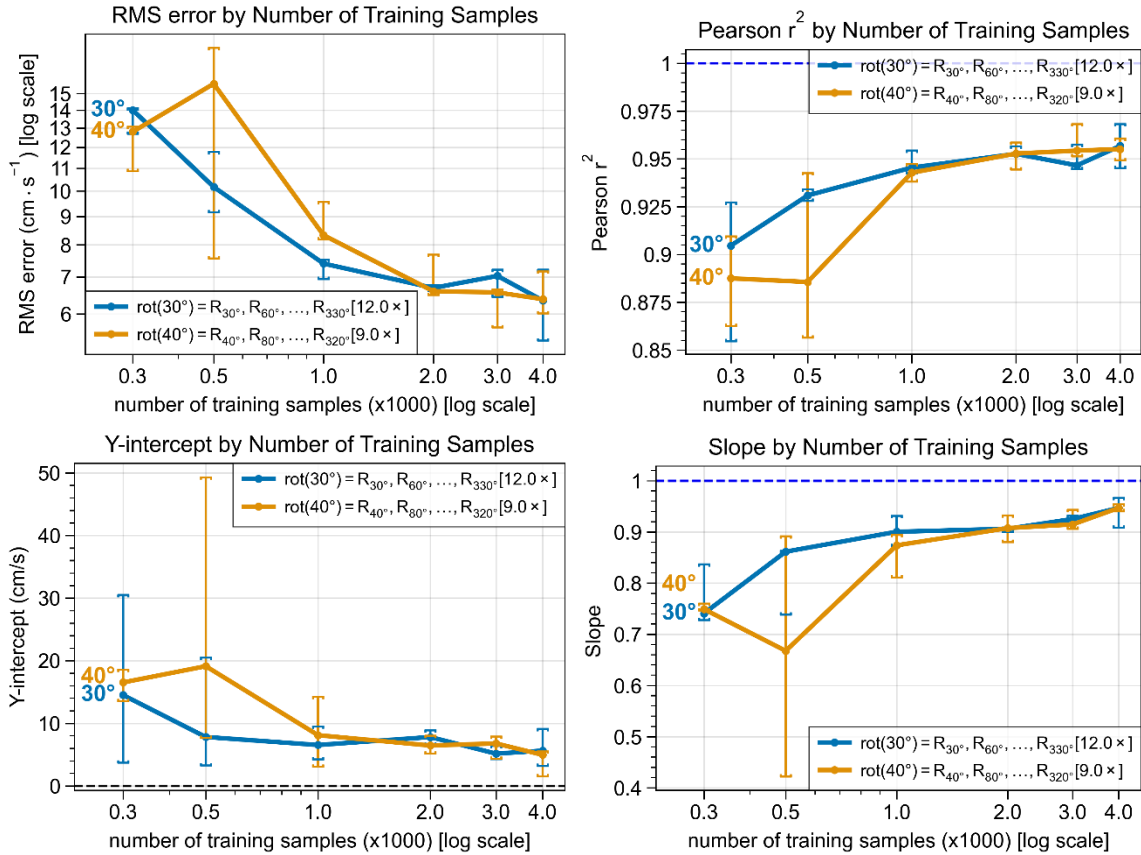


Figure 19. The results of applying reflection and rotation data augmentation to the data from the lab-built floats. Each point represents the median of 3 separate training/testing cycles; error bars represent the corresponding metric's maximum and minimum values.

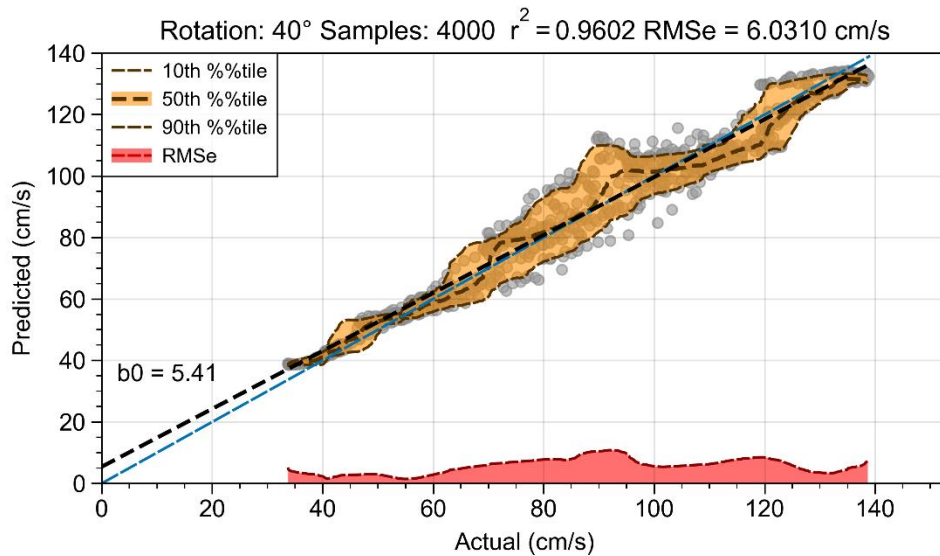


Figure 20. Scatterplot of the actual (ADCP-measured) current speed, plotted against the values calculated by the ANN after being trained on the data from a physically separate flow, deployed simultaneously near the same ADCP.

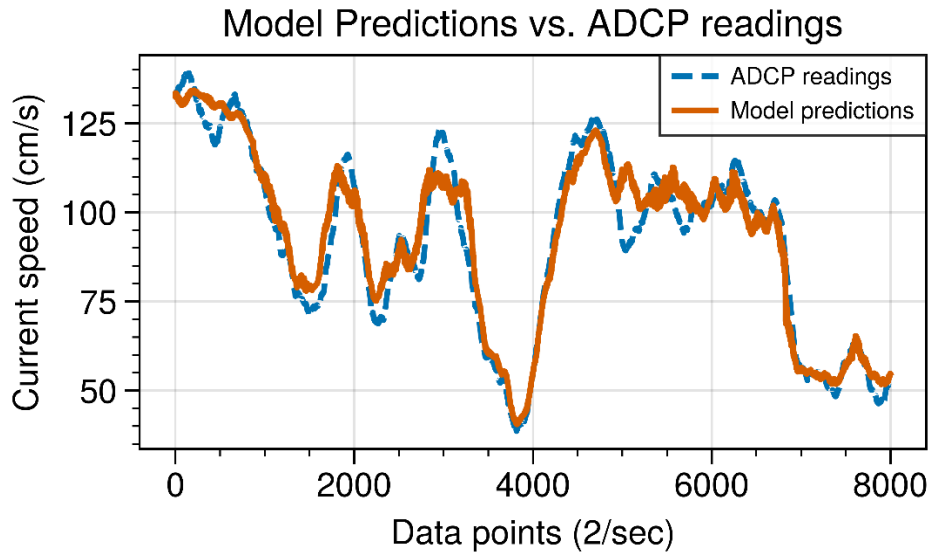


Figure 21. Here are the ADCP readings plotted against the same model as used in Figure 19 as a demonstration of the model's performance.

CHAPTER 2

DIGITAL INLINE HOLOGRAPHIC MICROSCOPY

INTRODUCTION

A hand-held particle sensor based on Digital Inline Holographic Microscopy (DIHM) is under development. The aim of the device is to record holographic images of environmental water samples in the field and perform rapid analyses of these samples to give timely information about the levels of contamination present. This was accomplished in the laboratory by uploading collected imagery over the Internet to network-connected computing resources to perform numerical reconstruction of sample volumes, perform analysis on the reconstructed volumes to characterize the particle populations of these samples, and to finally make a determination if there are bacteria or other pathogenic species present. The device uses commercial off-the-shelf (COTS) parts, such as an inexpensive solid-state laser such as the type found in laser pointers, and a CMOS sensor commonly used in smartphone cameras. These components are all mass-produced by the millions, and, due to the economies of scale are available very inexpensively. Several experimental trials have been performed and recorded, and the preliminary results are reported here. The potential advantages of this device are portability, low cost, and the purely optical nature of the detection process. The sensor consumes no chemical or biological media or reagents in its operation—only replacement flow chamber slides and small amounts of tubing need be replaced periodically to maintain the device.

PAPERS

This research effort has recently produced two peer-reviewed articles, published in the journal *Sensing and Imaging* in December of 2020. Rather than duplicate that text here, we direct the reader to Appendices X and Y for the full text of these papers, which detail the activities of this research program.

Note on author's contribution to the manuscripts: For both papers, the author of this dissertation wrote the software, created the methods, and drew most of the figures. The first-listed authors were undergraduate students working under the direction of the author.

CHAPTER 3

TECHNICAL BRIEF: COLLECTING REAL-TIME BATHYMETRY ABOARD A RESEARCH VESSEL

INTRODUCTION

The author has had a data collection and logging platform running continuously aboard the *R/V Neeskay* since 2007. It was originally created simply to log vital cruise data such as depth, temperature, and GPS coordinates as reported by the ship's navigational and sonar systems.

However, the infrastructure was soon expanded to allow rendering of bathymetry maps from the data.

This chapter is based on the content of several oral presentations given by the author, which is herein transcribed in written form.

TECHNICAL NOTES AND METHODS

The data collection, storage, indexing, retrieval, and map rendering runs on a shipboard Linux workstation. All software was constructed using open-source tools. These tools include Kermit (Cruz and Gianone 1996), R (R Core Team 2017), Python (Van Rossum and Drake 2009), MySQL, and others.

Why Open Source

Using open source tools helps to keep down the cost of constructing and maintaining the system. It also allows the free exchange of code with other academic and governmental institutions without legal or financial encumbrances.

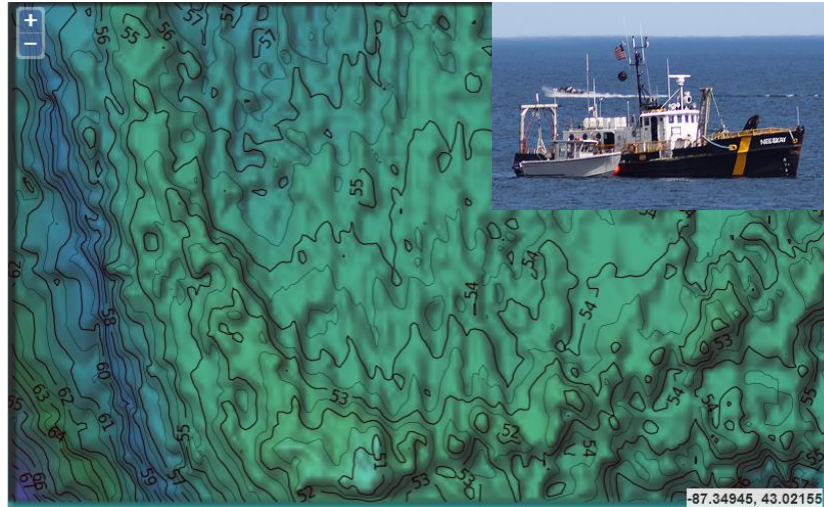


Figure 22. Detailed rendering of bathymetry obtained with single-beam sonar aboard the *R/V Neeskay* (inset).

Data collection

The data collection script is one of the key components of the system. Most shipboard navigation systems are capable of outputting a stream of data in computer-readable format. The set of standards by which such data is generated is called NMEA (Krile et al. n.d.), established by the National Marine Electronics Association. This data stream is read and parsed by a Kermit script. Kermit was chosen for this project because of its ability to interoperate with a large number of different protocols and systems. The data collected from the NMEA stream includes the parameters listed in Table 5.

Database Column	Description
recdate	Date/time recorded
gpslat	Latitude
gpslng	Longitude
depthm	Depth (m)
tempc	Temperature (degrees C)
gpsfixquality	Fix Quality
gpsnsats	Number of GPS satellites
gpshdop	GPS Horizontal Dilution of Precision
gpsalt	GPS Altitude
gpsttmg	GPS True Track Made Good
gpsmtmg	GPS Magnetic Track Made Good
gpssogn	GPS Speed Over Ground (knots)
gpssogk	GPS Speed Over Ground (km/h)
gpsmagvar	Magnetic variation from true north

Table 5. A listing of data values logged onboard the *R/V Neeskay* at a rate of 1 Hz.

These pieces of data are recorded at a rate of 1 Hz whenever the ship is underway.

Map Rendering

The map rendering component runs independently from the data collection. The latest version in use is written in Python (Van Rossum and Drake 2009) the interface is entirely web-based. A duplicate of the shipboard map rendering software is used by land-based servers to facilitate access to a mirrored copy of the data recorded by the ship. Typically the land and ship databases are synchronized while the ship is in dock, when data transfer speed is highest and the least costly.

Data increases in value over time

As this data collection platform has been allowed to run over many years' worth of cruises, the data has become more valuable, particularly over more well-trafficked areas of Lake Michigan. In some areas such as the Mid-Lake Reef Complex (Houghton et al. 2010) the map appears virtually blanketed with data points.

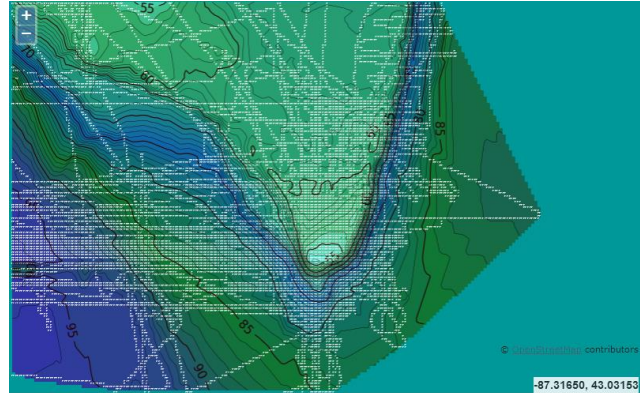


Figure 23. Some heavily-visited areas have a lot of data recorded over many cruises.

Dock soundings offer calibration opportunity

It is of course well known that lake levels are not stable, but vary quite substantially from year to year, month to month, sometimes even daily. So, even if you have the same boat running the same equipment, the data collected will develop errors over time. In the case of the *R/V Neeskay*, there is a USGS lake level gauge nearby.

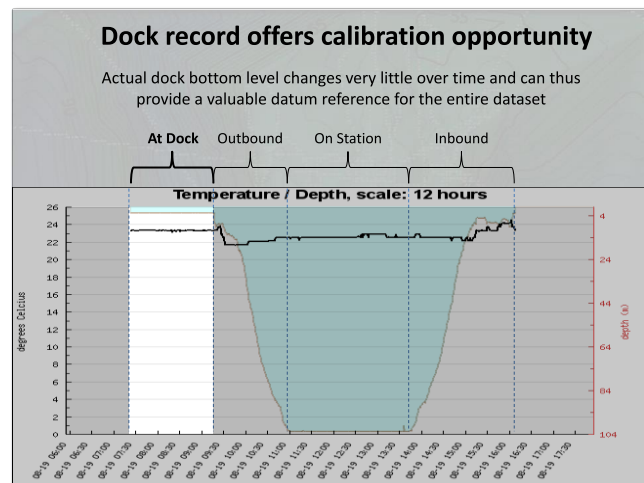


Figure 24. The dock location can provide a ground-truth for depth measurements.

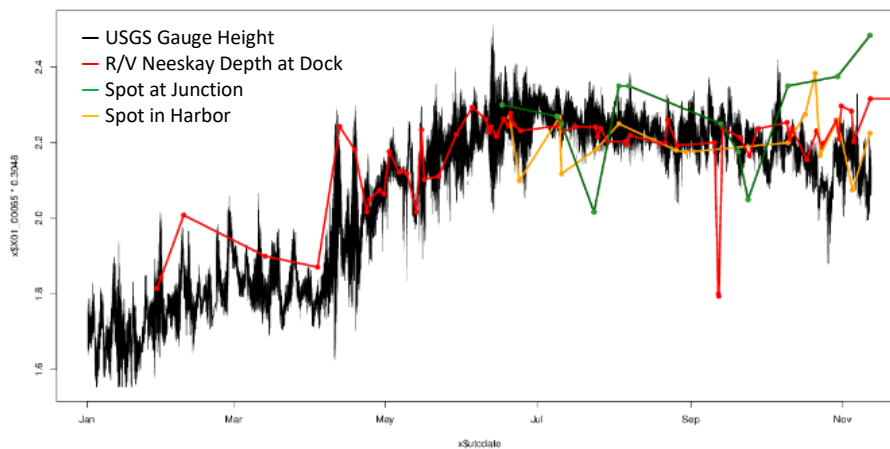


Figure 25. Soundings from *R/V Neeskay* at various locations plotted against the USGS gauge readings

In Figure 25 we plotted the reading from the USGS lake level guage against soundings from the *R/V Neeskay* and the result showed the expected correlation of readings.

FUTURE WORK

There are of course many potential uses for this data and software platform that have heretofore gone unexplored.

Develop a biotope map

Develop a biotope model of the area of interest. Use statistical techniques inspired by Elvenes et. al. 2013 to produce a biotic map of the interest area. (Elvenes et al. 2013)



Figure 26. Bathymetry of Hansen Point in the Lake Michigan Mid-Lake Reef Complex, as plotted with this system.

Produce a hydrodynamic model

Overlay a hydrodynamic model over the interest area to evaluate how it can improve predictions made by the biotope model. Thee author did preliminary investigation into using the Gerris flow solver, and produced the graph shown in Figure 27.

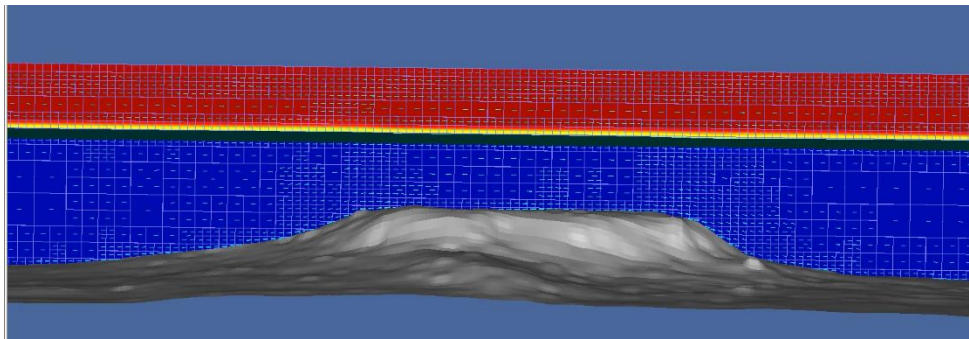


Figure 27. A preliminary demonstration of a hydrodynamic model over the Mid-Lake Reef Complex created by the author using the Gerris CFD. (Popinet 2003)

REFERENCES

- Cruz, F. da, & Gianone, C. (1996). *Using C-Kermit* (2nd edition.). Boston: Digital Press.
- Elvenes, S., Dolan, M. F. J., Buhl-Mortensen, P., & Bellec, V. K. (2013). An evaluation of compiled single-beam bathymetry data as a basis for regional sediment and biotope mapping. *ICES Journal of Marine Science: Journal du Conseil*, fst154. <https://doi.org/10.1093/icesjms/fst154>
- Houghton, C. J., Bronte, C. R., Paddock, R. W., & Janssen, J. (2010). Evidence for allochthonous prey delivery to Lake Michigan's Mid-Lake Reef Complex: Are deep reefs analogs to oceanic sea mounts? *Journal of Great Lakes Research*, 36(4), 666–673. <https://doi.org/10.1016/j.jglr.2010.07.003>
- Krile, S., Kezić, D., & Dimc, F. (n.d.). NMEA Communication Standard for Shipboard Data Architecture. *Naše more*, 15.
- Popinet, S. (2003). Gerris: a tree-based adaptive solver for the incompressible Euler equations in complex geometries. *Journal of Computational Physics*, 190(2), 572–600. [https://doi.org/10.1016/S0021-9991\(03\)00298-5](https://doi.org/10.1016/S0021-9991(03)00298-5)
- R Core Team. (2017). *R: A Language and Environment for Statistical Computing*. Vienna, Austria: R Foundation for Statistical Computing. <https://www.R-project.org/>
- Van Rossum, G., & Drake, F. L. (2009). *Python 3 Reference Manual*. Scotts Valley, CA: CreateSpace.

CHAPTER 4

A HIGHLY INTERACTIVE COMPUTATIONAL FLUID DYNAMICS MODEL

A Highly Interactive Computational Fluid Dynamics Model: Details of the technology and its implementation

Thomas F. Hansen, School of Freshwater Sciences, University of Wisconsin-Milwaukee

tomh@uwm.edu

Abstract

A highly interactive computational fluid dynamics (CFD) model is described. In its basic form, the model flow is visualized and projected on a wall. Users then place objects, or themselves, between the projector and the wall, and the shadows cast are detected by a digital video camera. The images of the shadows are then used to compute immersed boundaries in the path of the flow. The net effect is that the shadow appears as an object obstructing the flow, and the visualized flow reacts immediately to the changed boundaries. This allows the user to experiment with different arrangements and orientations of objects, or the user can simply stand in the flow field and reorient their limbs and posture, and see the results immediately reflected in the flow patterns. Early demonstrations to date have proven very popular with people of all ages and backgrounds, from very small children to seasoned professionals in a wide range of fields. The CFD model itself is based on the increasingly popular Lattice Boltzmann method (LBM). The system is implemented using OpenGL and the bulk of the model calculations are performed on a massively parallel processing unit (GPU) using vertex and fragment shaders coded in the GLSL language. The principles of the LBM are discussed, including specific add-ons and stabilizations incorporated to accommodate the features and challenges of this implementation. Details of the system are described, including descriptions of visualization techniques employed. The model is verified by experiment. Finally, some preliminary field test results are depicted.

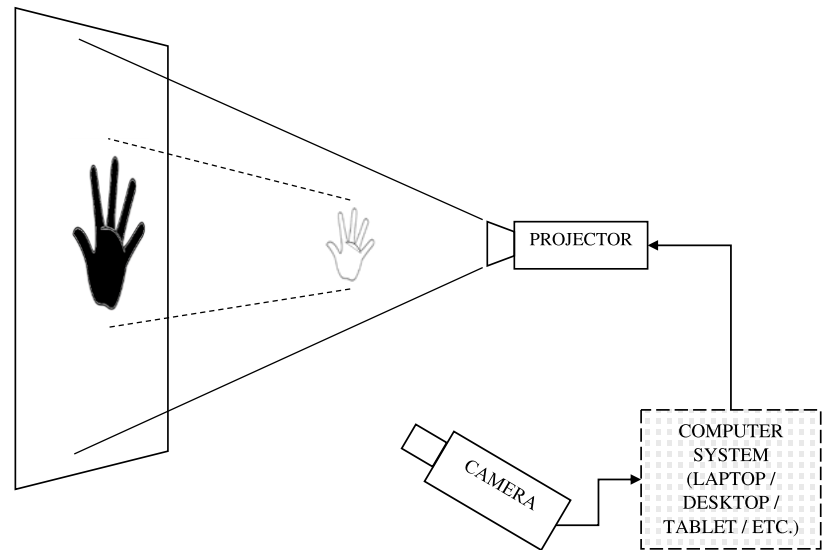


Figure 28. The author's nephew Max Hansen interacts with the CFD model.

I. INTRODUCTION AND MOTIVATION

A highly interactive computational fluid dynamics (CFD) model has been created by the author. Originally intended as a simple demonstration of the data visualization capabilities of the new facilities at UWM's School of Freshwater Sciences, it was immediately recognized as possessing significant potential as an educational tool. It creates dynamic flow visualizations which can be altered interactively by simply casting a shadow onto the projected visualization. This enables users, even very small children, to meaningfully interact with the simulated fluid flow field, and experience flow phenomena such as Bernoulli effects, Karman vortex streets, and so on by simply raising a hand, arm, hand-held objects, or even their whole bodies into the flow projection.

Figure 1 is a simple schematic which depicts the overall design conception. In short, the fluid flow simulation is projected onto a screen. Participants then cast shadows onto the projected flow field. A camera pointed at the screen detects the shadows and feeds their presence back into the model as boundaries to the flow.



This work was heavily inspired and motivated by the work of Snibbe

Figure 29. Simplified schematic drawing of the design and organization of the system. (From the author's provisional patent application, filed in March, 2015. See Appendix)

and Raffle (2009) who have been working in the field of what they describe as "Social Immersive Media" since 1998. The work of these artists highlights the benefits of such a paradigm in outreach and education – perhaps best summarized by the saying they cite, "I hear and I forget. I see and I remember. I do and I understand" (Snibbe and Raffle 2009).

While all their exhibits feature interactivity with users by the use of projected imagery and shadows, with some of them even featuring water themes, none have used fluid dynamics as an interactive component (Snibbe and Raffle 2009).

II. DESIGN AND METHODS

A. Background on the Lattice Boltzmann method (LBM)

The computational fluid dynamic model used in this system is based on the Lattice Boltzmann method (LBM) (Higuera and Jiménez 1989). This method is quite new; the first papers describing the method began to appear less than 30 years ago (Huang et al. 2015, p. 2). The LBM is derived from the concept of cellular automata as explored by computer science pioneer John von Neumann and others starting in the 1940s (Von Neumann 1951; Wolfram 1983).

A.1. Origins of the LBM

As von Neumann (1951) described, a cellular automaton is a collection of conceptual units called cells, most usefully arranged in a regular geometric pattern, or lattice, to represent a line, surface, or volume. Each cell carries a finite number of attributes that together comprise the state of the cell. Discrete time steps, most usefully regularly spaced in time, are defined, and each cell's state is computed at each time step as a function of the state of the automaton at the previous time step. In this way, the automaton's overall state thus evolves over time, based on the choice of attributes and the choice of functions that are used to compute the values of those attributes from each time step to the next. This paradigm can be useful for creating a model of physical phenomena. For example, heat propagating across a surface could be simulated by dividing the surface into a grid of cells and assigning each cell a temperature. Each cell's temperature could then be calculated for each consecutive time step using a relatively simple heat transfer equation, using only each cell's temperature and that of its adjacent cells.

The Lattice Boltzmann Method (LBM) was originally developed for computing gas flows (Higuera and Jiménez 1989). However, researchers recognized that the LBM results are valid for fluids in general as well, particularly at low Mach numbers—at speeds small compared to the speed of sound in the medium (Higuera and Succi 1989). It is straightforward to show that the well-known Navier-Stokes equations of fluid dynamics can be derived from the LBM equations (Chen et al. 1992; He and Luo 1997, p. 6813).

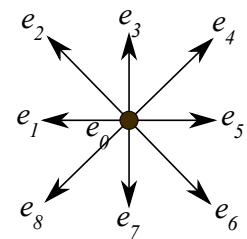


Figure 30. The nine basis vectors used for 2-D LBM (a.k.a. D2Q9)

A.2. Details of the method

The LBM is implemented as a von Neumann cellular automaton: it divides a line, plane, or volume into regularly spaced cells, and the state of the fluid at each time step is completely computed from the previous state. The state of the fluid in each cell, to be completely accurate, comprises the position and velocity of each molecule within the boundaries of the cell. The actual state for all practical purposes is incomputable. The LBM approximates each cell's fluid state by choosing a finite number of unit basis vectors and assigning a numeric coefficient to each basis vector. Each coefficient then represents the relative quantity of hypothetical fluid particles moving in the direction of that vector. (Heubes 2010)

The macroscopic properties of the fluid, such as velocity and pressure, are computed from the individual velocity distributions. Velocity is computed as the vector sum of each velocity distribution value multiplied by its corresponding basis vector. The pressure is recovered by taking the arithmetic sum of the magnitudes of each velocity distribution.

The computation for each time-step of the Lattice Boltzmann method consists of two fundamental sub-steps, which are both carried out, one after the other, when computing each time step. One sub-step is generally called the **streaming** step. It computes the position of the particle distributions from one step to the next. To simplify this step almost to the point of triviality, the basis vectors are chosen such that each basis vector points exactly towards the center of a neighboring cell (usually including one for stationary particles) and is proportional to the displacement between the cells. If we assume a grid size of 1, and a time step of 1, streaming simply calls for all velocity distributions to be moved to the adjacent cell in the direction of the vector: up, down, left, right, diagonally, or, in the case of \mathbf{e}_0 (the stationary particles) to stay where it is. (Tian et al. 2011) The process could be likened to moving many checkers on a checkerboard simultaneously, each checker representing a distribution of particles going in a particular direction.

The other sub-step is called the **collision** step, and it takes into account the physical interaction, or colliding, of the particles within each cell. It is in this step that a derivation of the Maxwell-Boltzmann distribution function is used to determine the new velocity distributions (Higuera and Jiménez 1989). To extend the checker analogy, it basically takes all the directions and values of the incoming checkers that have all landed on the same square, and reallocates their distributions for the next move, or time step. The commonly employed Bhatnagar, Gross, and Krook, (Bhatnagar et al. 1954) or BGK, collision model is used here.

A.3. Boundary Conditions

In its simplest form, boundary conditions involving fixed, no-slip boundaries are computed using what is termed a "bounce-back" scheme, in which the streaming step is modified so that particles which are destined to penetrate a boundary are instead effectively "bounced", or reflected, back into the fluid by propagating their values back into the original source cell, but pointing in the opposite direction. These are also the precise velocities which would otherwise be left empty, because fixed boundaries do not themselves produce particles.

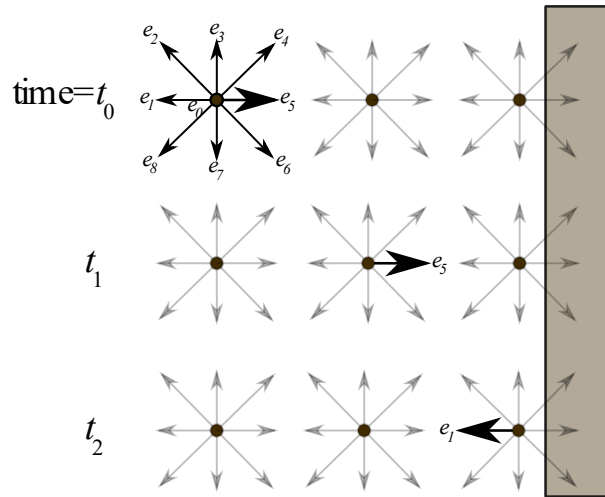


Figure 31. Illustration of the LBM "bounce-back" scheme

B. Advantages of the LBM for interactive applications

B.1. Parallelizable

A very important aspect of the Lattice Boltzmann method, which was recognized in its earliest published descriptions (Higuera and Jiménez 1989, p. 663; Higuera and Succi 1989, p. 517), is that for each step in the computation, the values for each lattice cell can be completely computed using only its own values and those of its immediate neighbors from the previous time step. This property of locality in the computations makes the method highly parallelizable, easily computed in parallel by dividing up the computational task among multiple processing units operating simultaneously. In particular, modern graphics cards' designs are particularly amenable to this type of parallel computation (Zhao 2008). Modern cards are based on graphics processor units, or GPUs, which contain hundreds – even thousands -- of individual processing cores operating simultaneously ("Compare and Buy GPUs | GeForce" n.d.)

B.2. Able to jump complex flows in a single bound(ary condition)

Another very important advantage of the Lattice Boltzmann method is the ease of specifying complex and arbitrary boundaries (Wei et al. 2004).

There are also relatively simple methods for implementing true immersed boundary (IB) conditions, which are important for the system's future enhancement. True immersed boundary conditions allow such things as accurate calculations of flow around moving boundaries, calculation of net drag, lift, and buoyancy forces on immersed objects, and simulating the interface between differing fluids (Dupuis et al. 2008; Seo and Mittal 2011; Tian et al. 2011)

C. Stabilizing the Model

An important consideration when designing interactive flow simulations is the stability of the model. This is because the user's actions cannot be predicted yet must be accommodated in real-time to avoid undesirable "blow ups" in the model (Stam 1999). For the lattice Boltzmann method, there are several published methods (Almalawi 2014; Brownlee et al. 2013) for increasing the stability of the model. These vary from simple entropy limiters that smooth out spikes in physical values and gradients to complex multi-relaxation-time methods involving large matrices and much-increased computation time.

The Brownlee (2013) paper contains a thorough comparison of several stabilization and regularization methods. The performance of the various methods were compared with each other under a variety of conditions and Reynolds numbers. Of particular note was this result: "For the final two Reynolds numbers we use, 7500 and 10000, only the BGK system with the Ehrenfest limiter completes the simulation" (Brownlee et al. 2013, p. 45). Although the most likely applications of this system will not experience Reynolds numbers approaching 7500 or 10000, the demonstrated stability of the "Ehrenfest limiter" makes it an attractive choice.

Fortuitously, the Ehrenfest limiter turned out to be one of the simplest to implement and inexpensive in terms of computational cost. As described in Brownlee (2013), implementation of the method involves calculating the change in entropy in a lattice cell from one time step to the next. If the change exceeds a given threshold value, the cell is simply taken to equilibrium; in effect, setting the local viscosity to zero for that one time step.

Calculating the change in entropy ΔS for each cell, in quadratic approximation, is (Brownlee et al. 2013, p. 36)

$$\Delta S = \sum_i \frac{(f_i - f_i^{eq})}{f_i^{eq}}$$

where f_i is the velocity distribution function and f_i^{eq} is the equilibrium distribution function. When the change in entropy exceeds a pre-determined value δ , the limiter is invoked, and the cell is set to equilibrium by assigning $f_i = f_i^{eq}$ for all distribution functions f_i .

If the value δ is chosen carefully, the Ehrenfest limiter provides, as described by Brownlee, "rare, intense, and localized corrections." As of this writing, the value of δ has been chosen empirically in order that the limiter exhibits this behavior. More robust methods of selecting sites for correction do exist (Brownlee et al. 2013, p. 37) but would result in increased computational demand.

D. Interactivity

The concept of interactivity with a projected image using shadows is not by any means unique to this system. As mentioned in the introduction, the author is familiar with the work of Scott Snibbe, who has experimented with many different and varied forms of shadow-projector interaction (Snibbe and Raffle 2009).

To accomplish the required interactivity, the author incorporated the OpenCV open-source computer vision library, which implements over 500 algorithms including image processing, background subtraction, and object tracking (Bradski 2000).

The use of OpenCV for this application, while ultimately rather straightforward, involves using many of the tools in unusual ways. For example, typically, shadow detection is accomplished in OpenCV for the purposes of removing said shadows from an image (Sanin et al. 2010). For this project, however, the requirement is to isolate the shadow and eliminate everything else.

A particularly challenging aspect of this system to implement is the precise alignment

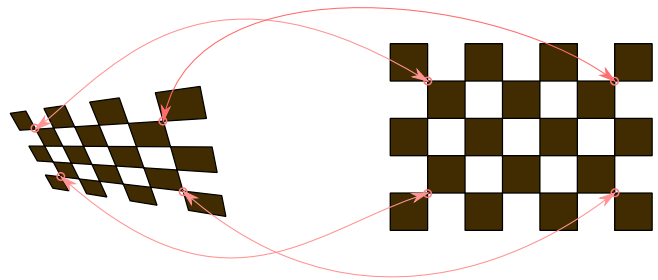


Figure 32. Using a projected chessboard pattern to adjust the camera image (left) to match the flow model (right).

which must be accomplished between the camera and the projection screen so that the software can take the position of the shadow as seen by the camera, and accurately calculate where the shadow falls in the model. This is crucial to the interactivity, as it is important that the computed solid barriers always coincide with the shadows in real time.

However, images projected onto flat surfaces are very often subject to rhombus-shaped distortions, commonly referred to as "keystoning" effects. Similarly, images taken by cameras of images on a flat surface usually exhibit similar distortions (Moreno and Taubin 2012).

Fortunately, the OpenCV library contains a camera calibration facility which is designed to counteract these effects. While ostensibly created to compensate for the distortions introduced by off-angle camera alignment, it works equally well if the image being recorded by the camera is itself similarly distorted. This is because both distortions are examples of linear transformations of a coordinate space, and the composition of two or more linear transformations is itself a linear transformation (Moreno and Taubin 2012).

In order to place this method in context, the author also reviewed the work of several other researchers, which included complex examples of 3-D object detection (Sadlo et al. 2005), and other techniques much more closely related to the camera-projector problem (Fiala and Shu 2007; Zhang 2000). All involved chessboard or chessboard-like images to calibrate use of cameras to acquire images projected onto surfaces, with good results.

For now, the system herein described is only equipped to compensate for linear distortions.

E. Visualizations Implemented

The following visualizations have been implemented in this system. All examples depict flow around a cylinder at $Re \approx 100$. For all visualizations, the macroscopic values are obtained using bilateral interpolation of the underlying lattice.

E.1. Simulated Injected Dye Advection Overlay (can overlay/coexist with all other visualizations)

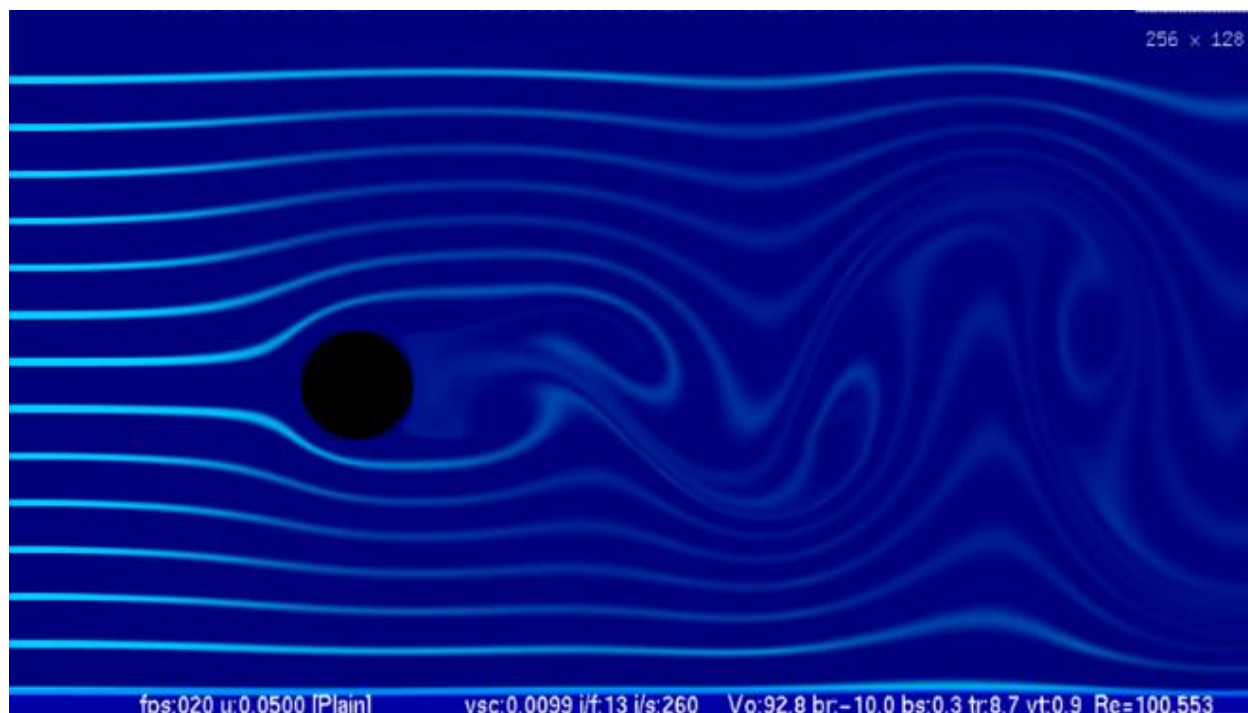


Figure 33. Simulated Injected Dye Advection Overlay

This is a very simplistic implementation in which each output frame is computed from the previous by applying this formula for each pixel p at location \vec{x} in the domain, and the corresponding fluid velocity $\vec{u}(\vec{x})$ at those points:

$$p(\vec{x}, t + \Delta t) = p(\vec{x} - \vec{u}(\vec{x})\Delta t, t)$$

So for each pixel, this formula simply "looks back" to where the fluid that pixel represents must have been at the time t and places that value in the current pixel for time $t + \Delta t$.

This is a slight simplification, because in reality a Runge-Kutta fourth order approximation is done to improve the accuracy of the advection. See reference (Weisstein n.d.) for more information on the Runge-Kutta fourth order approximation.

E.2. Lagrangian Particles overlay (can overlay/coexist with all other visualizations)

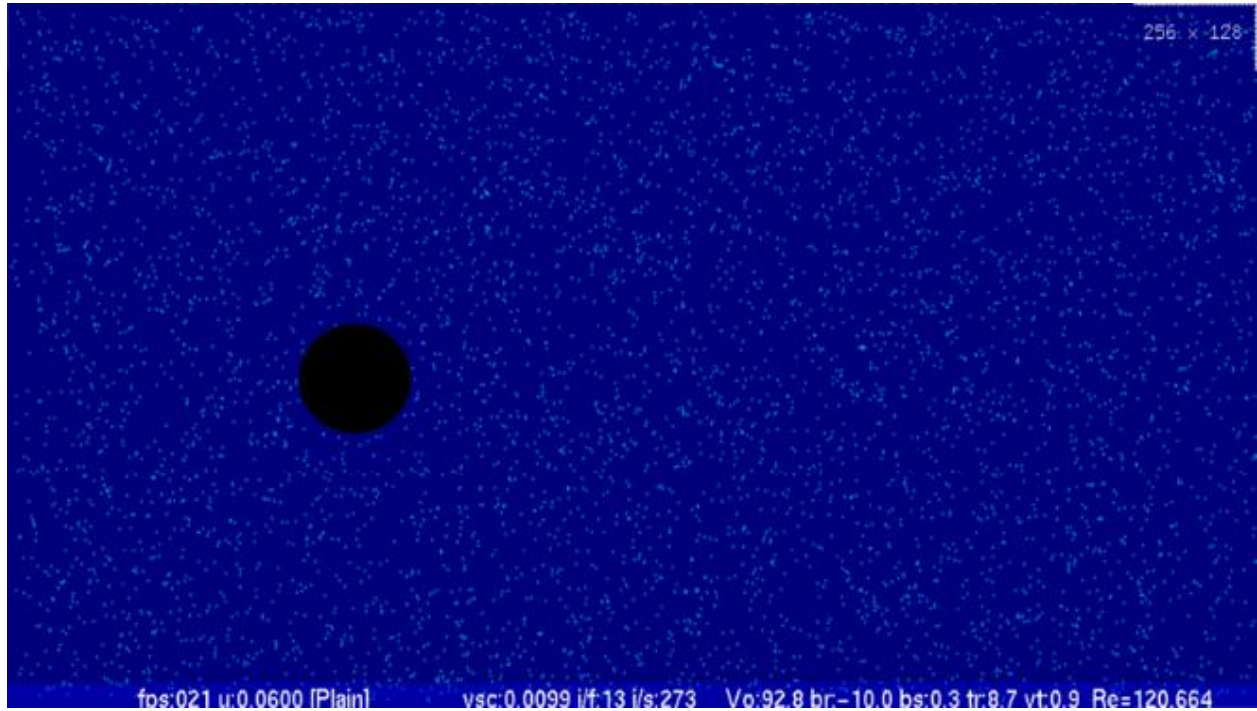


Figure 34. Lagrangian particles overlay

These are simply particles that behave as massless points embedded in the flow. Their position \vec{p}_t is updated as follows:

$$\vec{p}_{t+\Delta t} = \vec{p}_t + \vec{u}(\vec{p})$$

Again, in practice the Runge-Kutta method (Weisstein n.d.) is used for better accuracy.

Note: all other visualizations are akin to "backgrounds," and cannot coexist with any of the other backgrounds. They may have either of the above overlays applied to them, however.

E.3) Speed

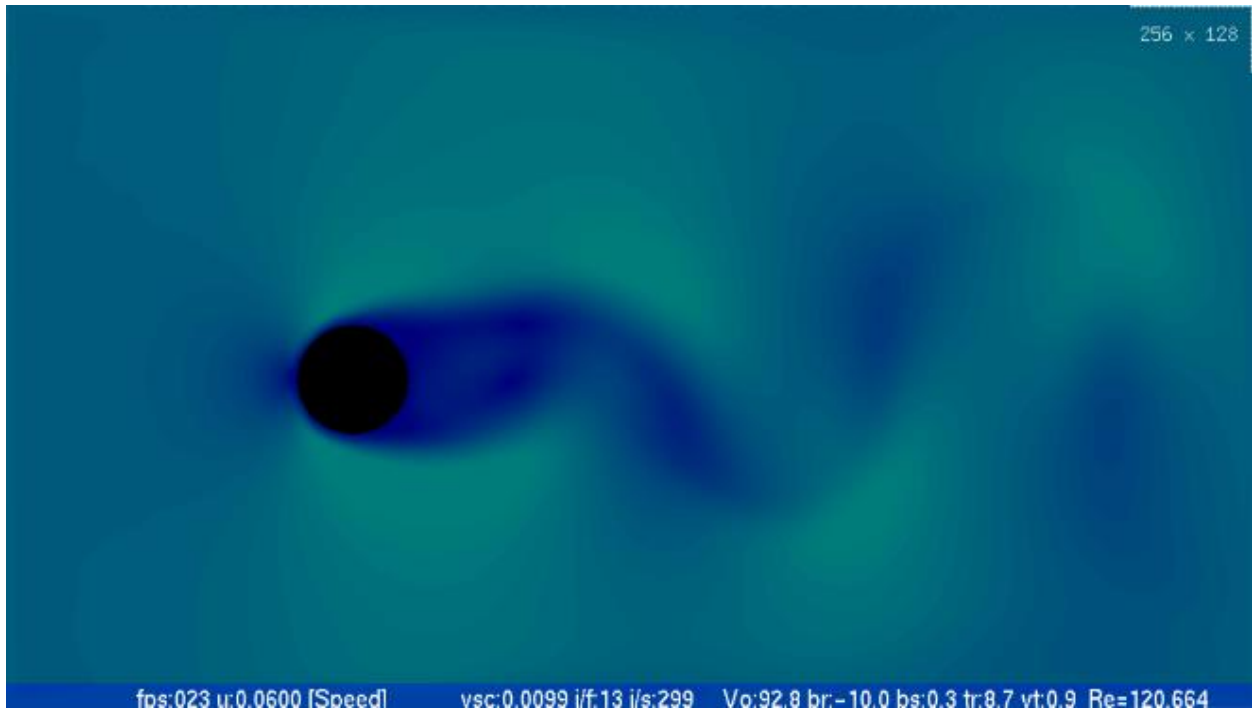


Figure 35. Speed

This is simply a plot of the speed, or the magnitude of the velocity, at each pixel.

E.4. Vorticity

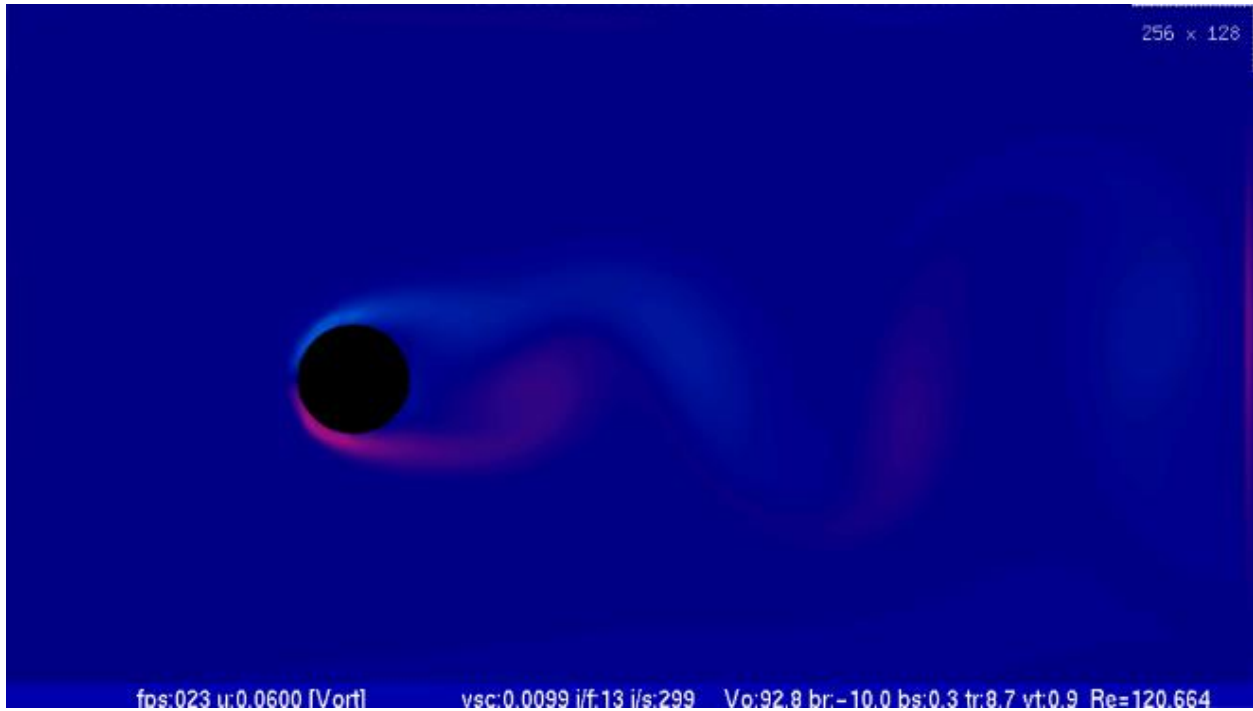


Figure 36. Vorticity

Vorticity is a measure of the rotational moment of a fluid. The vorticity at each point is calculated using the well-known discrete vorticity formula

$$\frac{u_y(x-h, y) - u_y(x+h, y) + u_x(x, y+h) - u_x(x, y-h)}{h}$$

Where h is the distance between cells, $u_x(x, y)$ is the component of the fluid velocity parallel to the x-axis at that point, and $u_y(x, y)$ is the component of the fluid velocity parallel to the y-axis.

E.5. Line Integral Convolution (LIC)

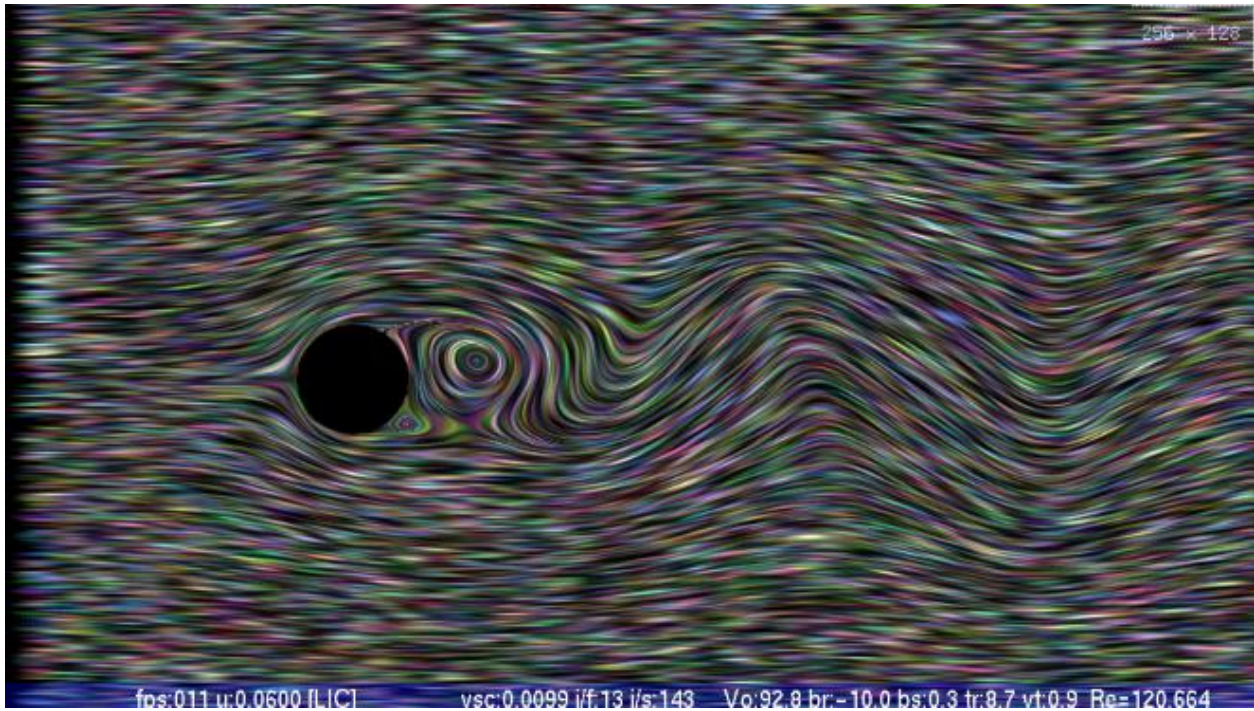


Figure 37. LIC

The LIC method allows for the easy recognition of many important characteristics of fluid flow (Liu et al. 2012). It is created by starting with a field of random noise, and, for each pixel in the output, integrating along the streamline intersecting that pixel for a short distance. This has the effect of stretching the original noise pixels along the streamlines, giving the effect of stirring a multicolored fluid, or pulling taffy. In many cases it is more effective when combined with another visualization method. The next two visualizations incorporate LIC.

E.6. LIC+Speed

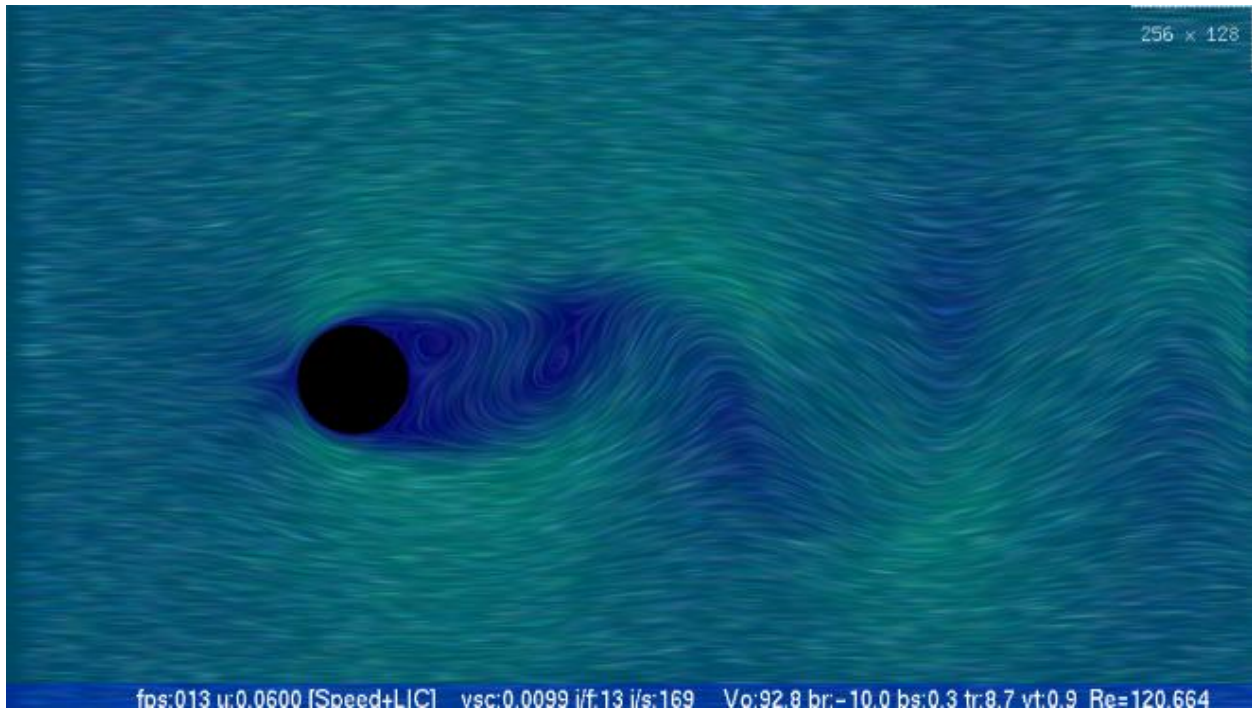


Figure 38. LIC+Speed

This is a composition of the speed visualization and the LIC visualization.

E.7. LIC+Vorticity

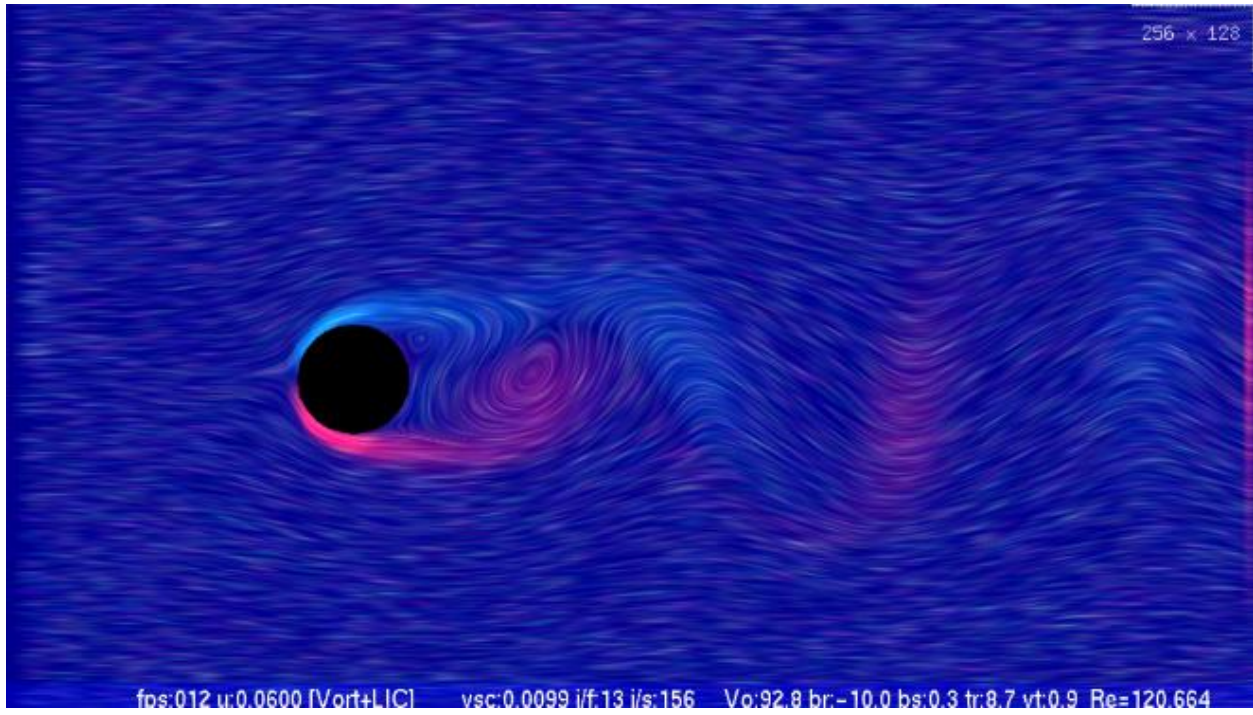


Figure 39. LIC+Vorticity

This is a composition of the vorticity visualization and the LIC visualization.

E.8. Pressure

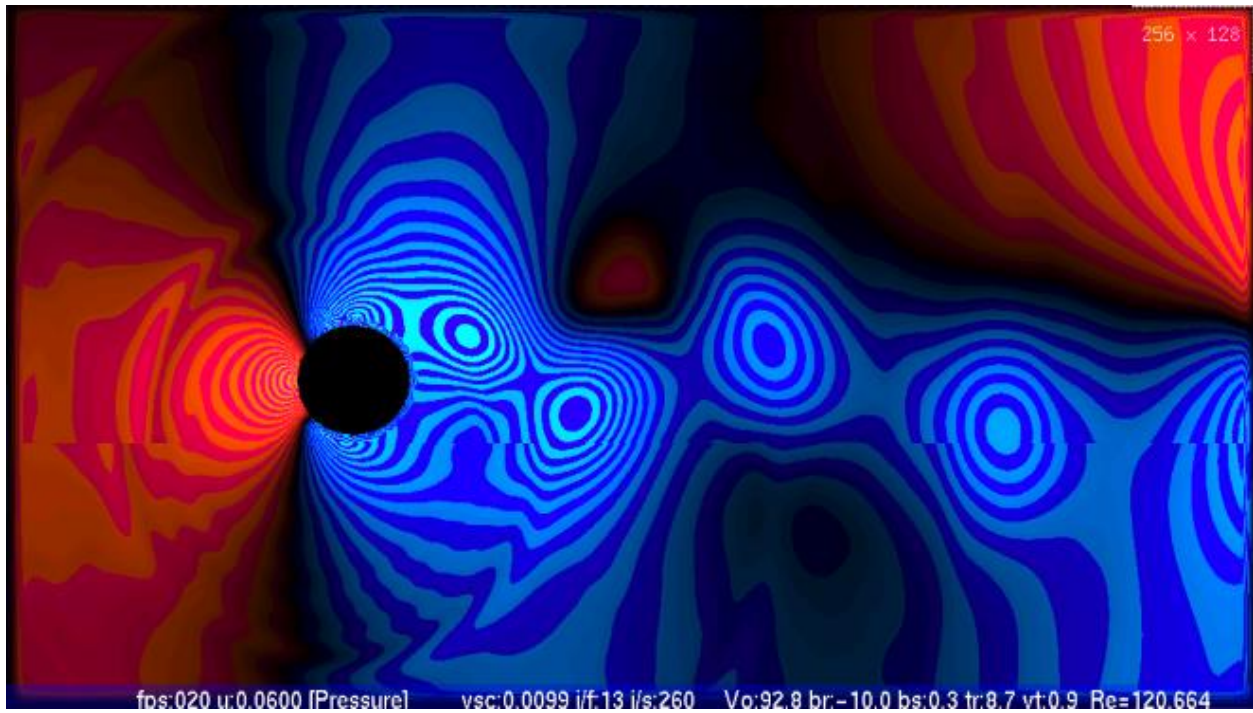


Figure 40. Pressure

This visualization depicts pressure variations from "gauge pressure" which is unity in this non-dimensional model. Black is gauge pressure; increasing shades of blue represent pressures lower than gauge, and increasing shades of red indicate pressures exceeding gauge pressure.

III. EXPERIMENTAL RESULTS

Experimental trials were run in order to verify that the model behaves as expected in standard tests at relevant Reynolds numbers. These tests demonstrate if the crucial calculations of relaxation time in the BGK model from a given viscosity are correct.

Note that these tests are partially qualitative, because as of this writing, the model does not output numerical data directly. This is because the numerical model is run entirely on the GPU, with all results being displayed graphically on screen. (Note that this is not a technical problem. Eventually the code will be added to extract numerical results, it simply has not been a priority to date.)

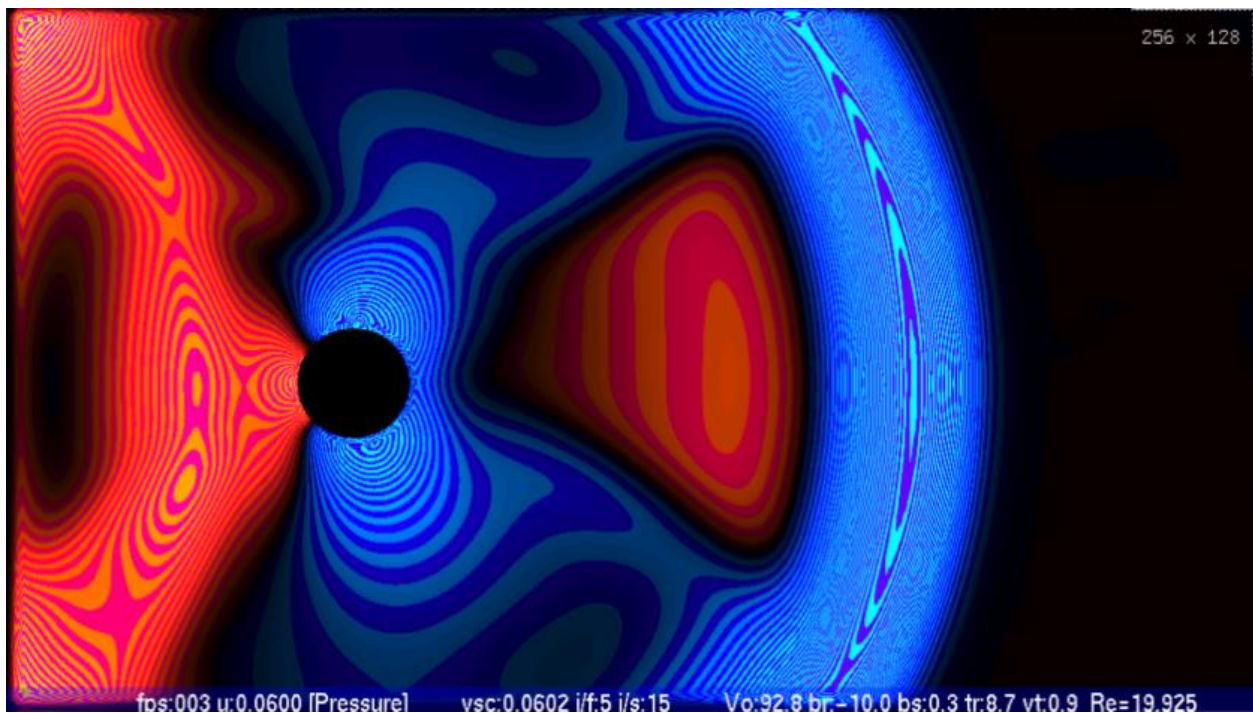


Figure 41. Sudden introduction of cylinder into flow

These experiments followed the initial conditions of Higuera and Succi (1989), simulating the abrupt introduction of a cylinder into a uniform flow.

Higuera and Succi (1989), describe that the behavior of their model displayed three phases. The first, immediately after the cylinder is introduced, consists of acoustic waves which reverberate around the domain for a short time. The second phase consists of the vortex pair behind the cylinder forming and growing, and the third phase is either the steady state (for low Reynolds numbers) or the unsteady vortex shedding mode (for high Reynolds numbers).

Careful examination of the behavior of the author's model showed that its behavior is consistent with the description given by Higuera and Succi (1989) in this regard. The accompanying figure shows the expanding pressure front as it quickly approaches the right-hand outflow edge of the domain, using the Pressure visualization.

A. Simulating Flow around a cylinder at various Reynolds numbers to determine Re_c

As a first test, flow around a cylinder was simulated at a series of Reynolds numbers to determine approximately the value of the critical Reynolds number Re_c , below which flow reaches a steady state, and above which flow is unsteady (Higuera and Succi 1989; Kumar and Mittal 2006).

A.1. Reynolds number ≈ 20

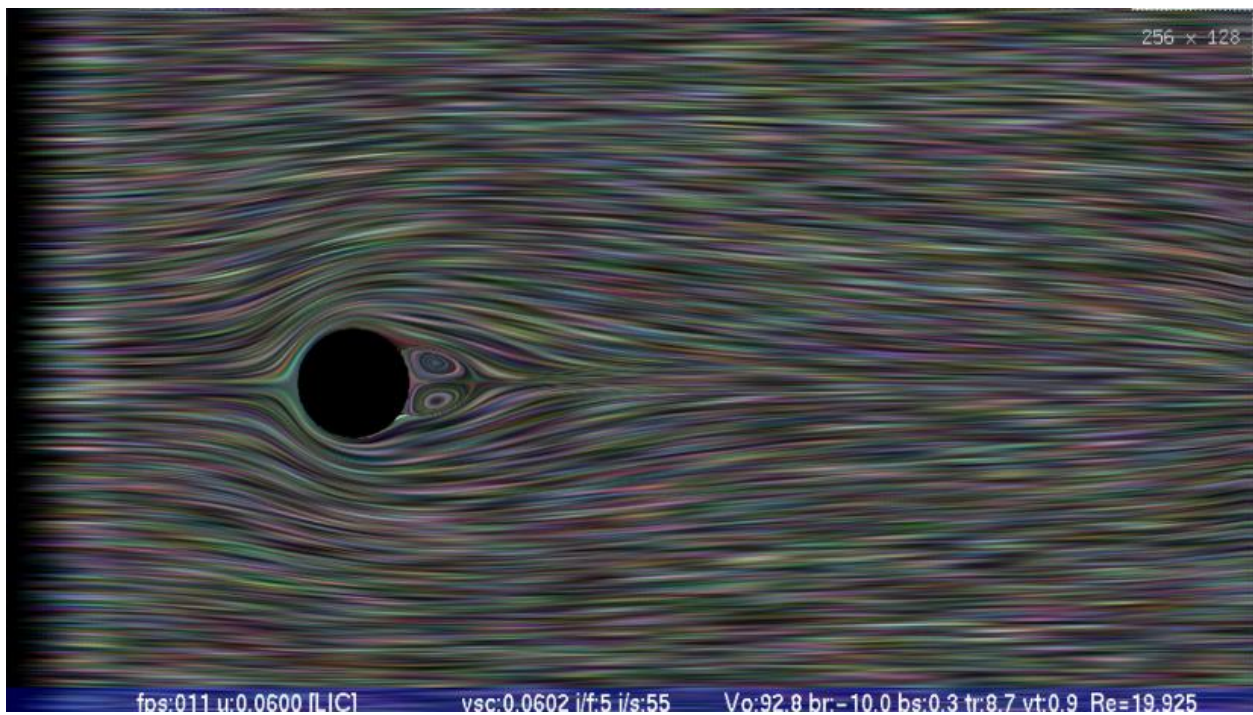


Figure 42. Cylinder at Reynolds number ≈ 20

At a Reynolds number of 20, vortices quickly formed in the wake of the cylinder and remained stable.

A.2) Reynolds number ≈ 30

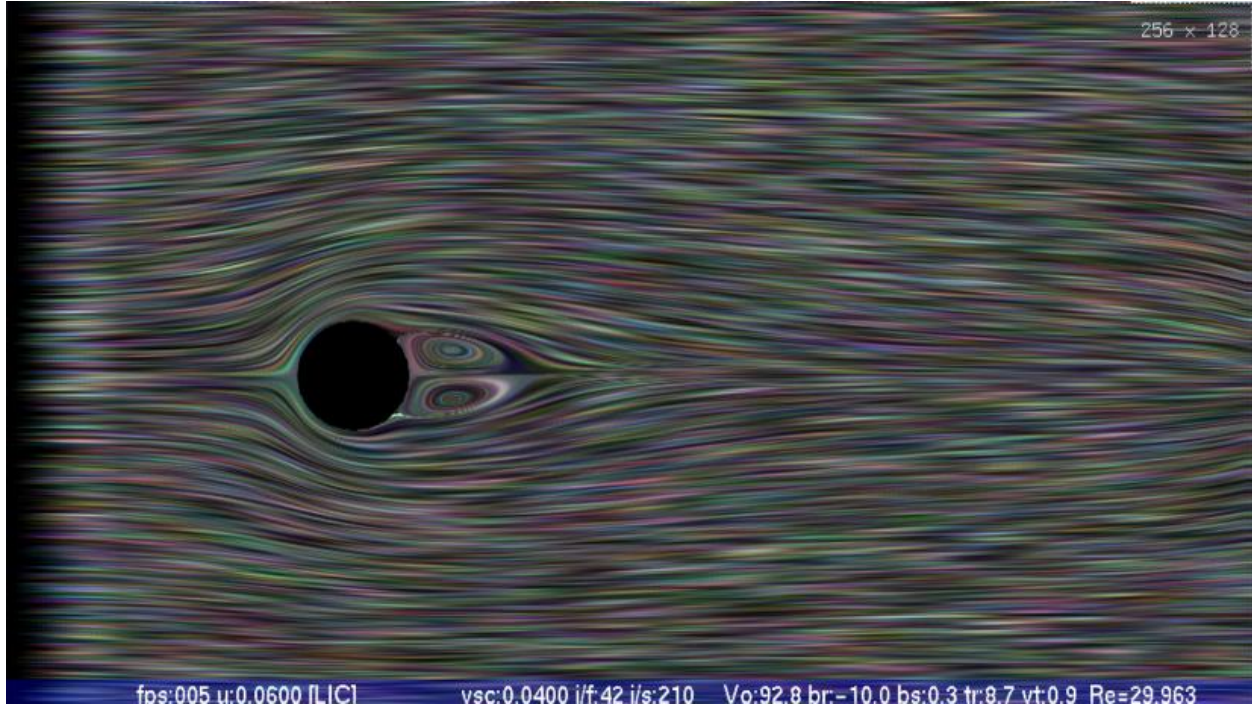


Figure 43. Cylinder at Reynolds number ≈ 30

At Reynolds number of 30, the vortices took a bit longer to stabilize, however the simulation did arrive at steady state.

A.3. Reynolds number ≈ 40

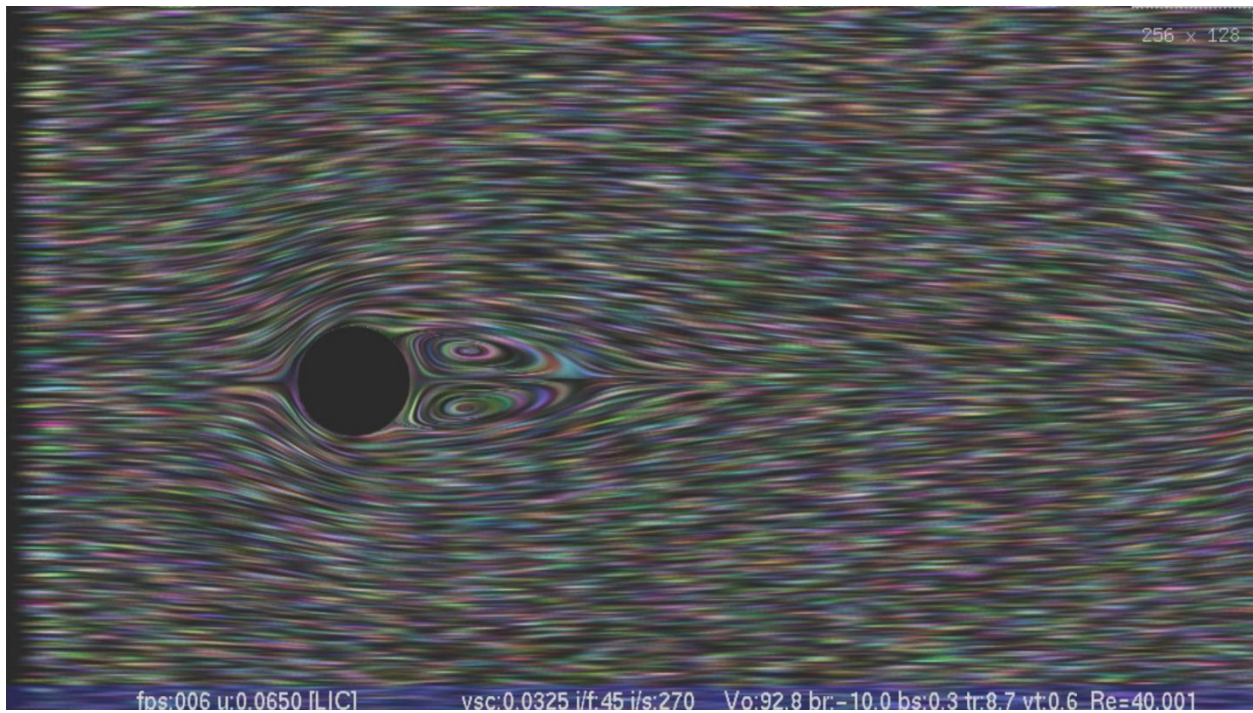


Figure 44. Cylinder at Reynolds number ≈ 40

Here we had for the first time a significant wait before the vortices stabilized. The author estimated approximately 4-5 residence times (horizontal velocity divided by domain width) before steady state was achieved.

A.4. Reynolds number ≈ 50

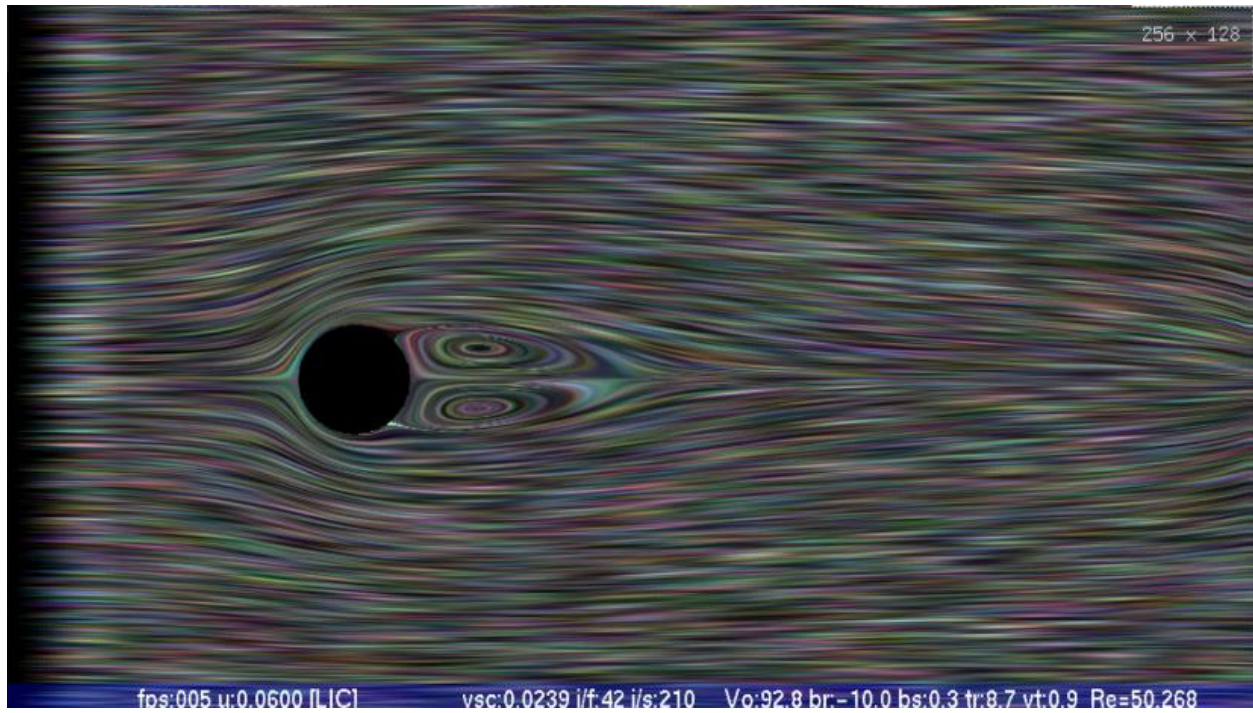


Figure 45. Cylinder at Reynolds number ≈ 50

At this Reynolds number, the model was allowed to run for a very long time, and the flow never fully stabilized.

The vortices continued to slowly oscillate, and the boundary between them continued to move for up to an hour—after which the simulation was ended.

A.5) Reynolds number ≈ 60

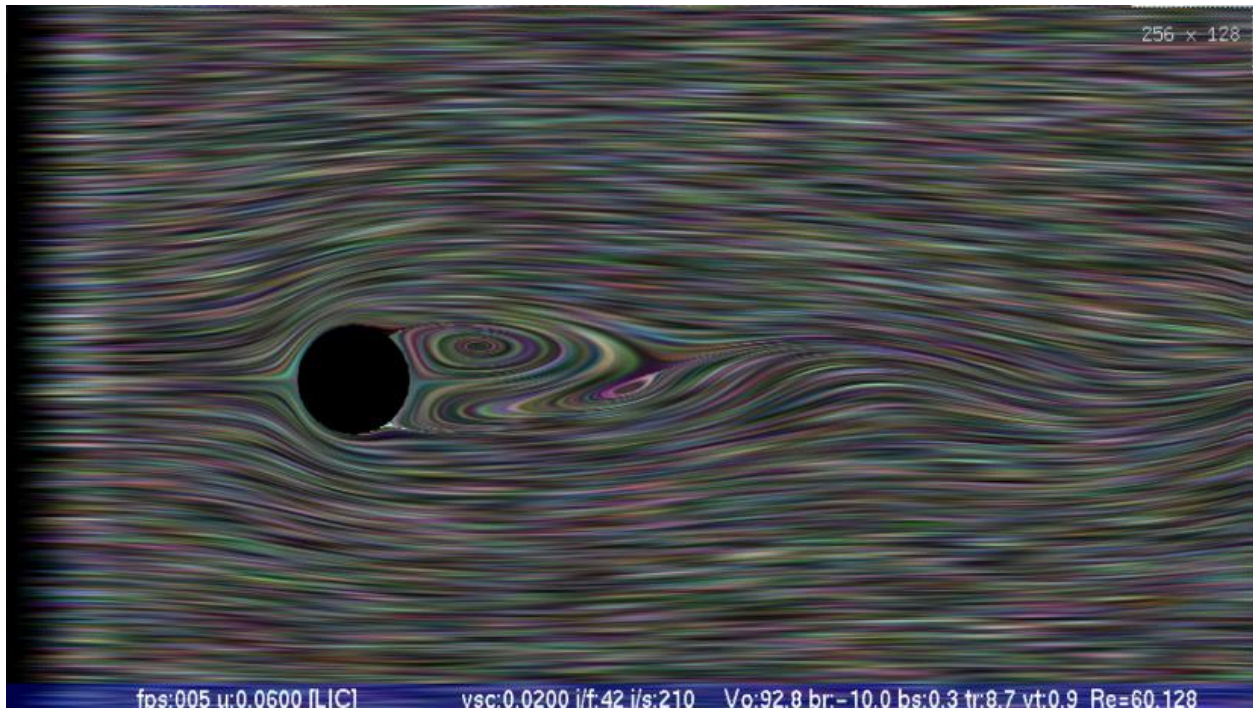


Figure 46. Cylinder at Reynolds number ≈ 60

Here the flow was clearly unsteady, and vortices began shedding after a short time.

A.6. Conclusion from first test

It is evident from these tests that the Re_c which marks the critical point of transition between steady and unsteady flow, is less than 60 and greater than 40, and very likely near 50. This is consistent with the published results of several studies (Table 6).

Critical Reynolds Number	Study
$Re_c \approx 48$	(Rajani et al. 2009)
$Re_c \approx 46$	(Higuera and Succi 1989)
$Re_c \approx 46.877, 47.318$	(Kumar and Mittal 2006)

Table 6. Critical Reynolds numbers from various studies

Kumar & Mittal (2006, p. 6047), in addition to sharing the results from their own numerical model, published a table of values of Re_c obtained from a wide variety of sources, including results from both physical experiment and numerical calculations. All values of Re_c listed were in the range of 39 – 50, with most of them (8 out of 13) in the range of 45 – 48.

These results strongly indicate that the numerical model constructed for this system is numerically sound, and that the calculations for viscosity and Reynolds number are within a useful range of accuracy.

IV. FIELD RESULTS

The model has been field tested at a public exhibit, the Milwaukee Maker Faire 2015. The reception was outstanding, and much interest was generated.



Figure 47. Children interacting with the display at Milwaukee Maker Faire 2015

V. Updates as of January 2021

The previous sections of this chapter were originally written in 2015. There have been many significant developments since then.

A. Technology Licensed

The technology was licensed by the UWM Research Foundation in 2016 to Science Kinetics, a Columbus, OH based company. The author's technology is featured on the company's web site ("Science Kinetics | Augmented Reality Wall" n.d.). The first royalty-generating sale by Science Kinetics, in 2017, was to the Virgin Islands Children's Museum in St. Thomas. ("The Virgin Islands Children's Museum" n.d.) There have been several other

installations purchased to date, including most notably the Great Lakes Science Center in Cleveland, OH. ("Great Lakes Science Center" n.d.) Approximately \$4000 in royalties have been generated to date.

B. Grants and Awards

- **NSF iCorps** The author was chosen to participate in the NSF iCorps program in summer of 2017 that included a \$2400 award.
- **UWM Research Foundation 2016 Annual Report** The Immersive Fluid Flow Experience was featured as the basis of the cover art for the UWM Research Foundation 2017 Annual Report and was prominently featured in a story.

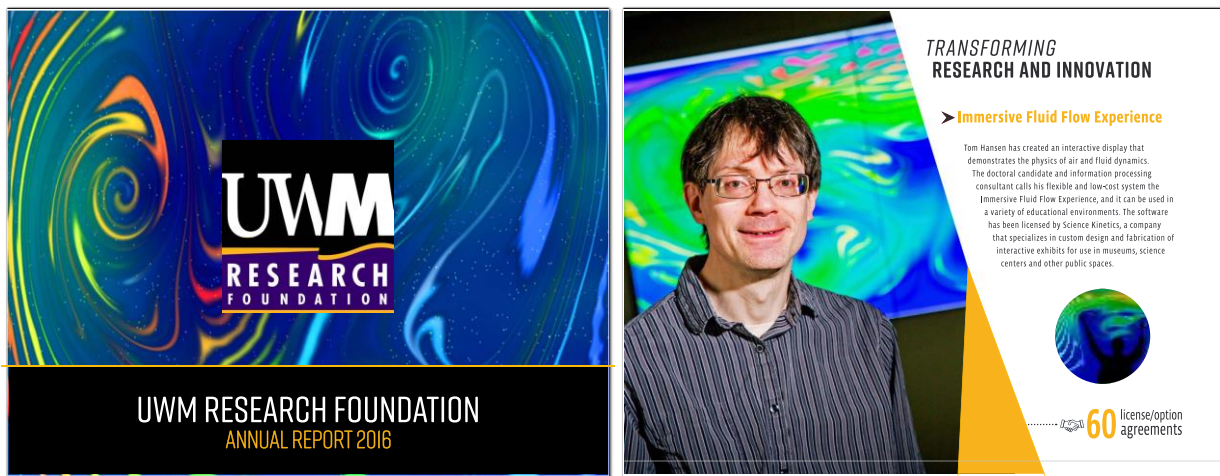


Figure 48. Technology featured in UWM Research Foundation Annual Report 2016

- **UWM Research Foundation 2017 Annual Report** The author and this work were featured in the UWM Research Foundation's 2017 Annual Report.

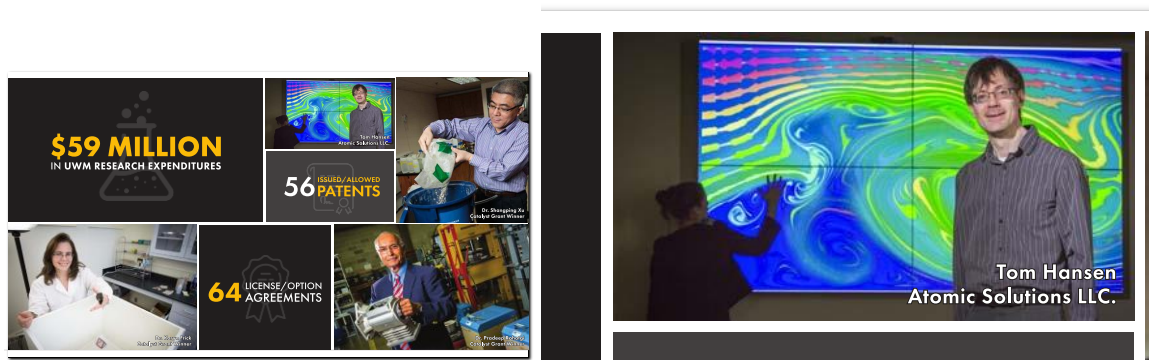


Figure 48. Technology featured in UWM Research Foundation Annual Report 2017

REFERENCES

- Almalowi, S. J. (2014). *Developing a stable lattice Boltzmann method for computational fluid dynamics applications* (Ph.D.). Lehigh University, United States -- Pennsylvania. Retrieved from <http://search.proquest.com/docview/1654788915/abstract/7F7FF0F8E4B542D8PQ/1?accountid=15078>
- Bhatnagar, P. L., Gross, E. P., & Krook, M. (1954). A model for collision processes in gases. I. Small amplitude processes in charged and neutral one-component systems. *Physical review*, *94*(3), 511.
- Bradski, G. (2000). The OpenCV library. *Dr. Dobb's Journal*, *25*(11), 120–125.
- Brownlee, R. A., Levesley, J., Packwood, D., & Gorban, A. N. (2013). Add-ons for Lattice Boltzmann Methods: Regularization, Filtering and Limiters. *Prog. Comput. Phys*, *3*, 31–52.
- Chen, H., Chen, S., & Matthaeus, W. H. (1992). Recovery of the Navier-Stokes equations using a lattice-gas Boltzmann method. *Physical Review A*, *45*(8), R5339–R5342. <https://doi.org/10.1103/PhysRevA.45.R5339>
- Compare and Buy GPUs | GeForce. (n.d.). <http://www.geforce.com/hardware/compare-buy-gpus>. Accessed 28 September 2015
- Dupuis, A., Chatelain, P., & Koumoutsakos, P. (2008). An immersed boundary–lattice-Boltzmann method for the simulation of the flow past an impulsively started cylinder. *Journal of Computational Physics*, *227*(9), 4486–4498. <https://doi.org/10.1016/j.jcp.2008.01.009>
- Fiala, M., & Shu, C. (2007). Self-identifying patterns for plane-based camera calibration. *Machine Vision and Applications*, *19*(4), 209–216. <https://doi.org/10.1007/s00138-007-0093-z>
- Great Lakes Science Center. (n.d.). *Great Lakes Science Center*. <https://greatscience.com/>. Accessed 17 January 2021
- He, X., & Luo, L.-S. (1997). Theory of the lattice Boltzmann method: From the Boltzmann equation to the lattice Boltzmann equation. *Physical Review E*, *56*(6), 6811.
- Heubes, D. (2010). Lattice Boltzmann Method in Theory and in Application to Coupled Problems.". http://www-num.math.uni-wuppertal.de/fileadmin/mathe/www-num/theses/ma_heubes.pdf. Accessed 31 July 2015
- Higuera, F. J., & Jiménez, J. (1989). Boltzmann Approach to Lattice Gas Simulations. *EPL (Europhysics Letters)*, *9*(7), 663. <https://doi.org/10.1209/0295-5075/9/7/009>

- Higuera, F. J., & Succi, S. (1989). Simulating the Flow Around a Circular Cylinder with a Lattice Boltzmann Equation. *EPL (Europhysics Letters)*, 8(6), 517. <https://doi.org/10.1209/0295-5075/8/6/005>
- Huang, H., Sukop, M., & Lu, X. (2015). *Multiphase Lattice Boltzmann Methods: Theory and Application*. John Wiley & Sons.
- Kumar, B., & Mittal, S. (2006). Prediction of the critical Reynolds number for flow past a circular cylinder. *Computer Methods in Applied Mechanics and Engineering*, 195(44–47), 6046–6058. <https://doi.org/10.1016/j.cma.2005.10.009>
- Liu, Z., Cai, S., Swan, J. E., Moorhead, R. J., Martin, J. P., & Jankun-Kelly, T. J. (2012). A 2D Flow Visualization User Study Using Explicit Flow Synthesis and Implicit Task Design. *IEEE Transactions on Visualization and Computer Graphics*, 18(5), 783–796. <https://doi.org/10.1109/TVCG.2011.110>
- Llewellyn, E. W. (2010). LBflow: An extensible lattice Boltzmann framework for the simulation of geophysical flows. Part I: theory and implementation. *Computers & Geosciences*, 36(2), 115–122. <https://doi.org/10.1016/j.cageo.2009.08.004>
- Moreno, D., & Taubin, G. (2012). Simple, Accurate, and Robust Projector-Camera Calibration. In *2012 Second International Conference on 3D Imaging, Modeling, Processing, Visualization and Transmission (3DIMPVT)* (pp. 464–471). Presented at the 2012 Second International Conference on 3D Imaging, Modeling, Processing, Visualization and Transmission (3DIMPVT). <https://doi.org/10.1109/3DIMPVT.2012.77>
- Rajani, B. N., Kandasamy, A., & Majumdar, S. (2009). Numerical simulation of laminar flow past a circular cylinder. *Applied Mathematical Modelling*, 33(3), 1228–1247. <https://doi.org/10.1016/j.apm.2008.01.017>
- Sadlo, F., Weyrich, T., Peikert, R., & Gross, M. (2005). A practical structured light acquisition system for point-based geometry and texture. In *Point-Based Graphics, 2005. Eurographics/IEEE VGTC Symposium Proceedings* (pp. 89–145). Presented at the Point-Based Graphics, 2005. Eurographics/IEEE VGTC Symposium Proceedings. <https://doi.org/10.1109/PBG.2005.194069>
- Sanin, A., Sanderson, C., & Lovell, B. C. (2010). Improved Shadow Removal for Robust Person Tracking in Surveillance Scenarios. In *2010 20th International Conference on Pattern Recognition (ICPR)* (pp. 141–144). Presented at the 2010 20th International Conference on Pattern Recognition (ICPR). <https://doi.org/10.1109/ICPR.2010.43>

- Science Kinetics | Augmented Reality Wall. (n.d.). *Science Kinetics*. <https://www.sciencekinetics.com/exhibits-catalog-home/augmented-reality-wall>. Accessed 17 January 2021
- Seo, J. H., & Mittal, R. (2011). A sharp-interface immersed boundary method with improved mass conservation and reduced spurious pressure oscillations. *Journal of Computational Physics*, 230(19), 7347–7363. <https://doi.org/10.1016/j.jcp.2011.06.003>
- Snibbe, S. S., & Raffle, H. S. (2009). Social Immersive Media: Pursuing Best Practices for Multi-user Interactive Camera/Projector Exhibits. In *Proceedings of the SIGCHI Conference on Human Factors in Computing Systems* (pp. 1447–1456). New York, NY, USA: ACM. <https://doi.org/10.1145/1518701.1518920>
- Stam, J. (1999). Stable fluids. In *Proceedings of the 26th annual conference on Computer graphics and interactive techniques* (pp. 121–128). ACM Press/Addison-Wesley Publishing Co. <http://dl.acm.org/citation.cfm?id=311548>. Accessed 28 September 2015
- The Virgin Islands Children's Museum. (n.d.). *VI Children's Museum*. <https://www.vichildrensmuseum.org>. Accessed 17 January 2021
- Tian, F.-B., Luo, H., Zhu, L., Liao, J. C., & Lu, X.-Y. (2011). An efficient immersed boundary-lattice Boltzmann method for the hydrodynamic interaction of elastic filaments. *Journal of computational physics*, 230(19), 7266–7283. <https://doi.org/10.1016/j.jcp.2011.05.028>
- Von Neumann, J. (1951). The general and logical theory of automata. *Cerebral mechanisms in behavior*, 1–41.
- Wei, X., Zhao, Y., Fan, Z., Li, W., Qiu, F., Yoakum-Stover, S., & Kaufman, A. E. (2004). Lattice-based flow field modeling. *IEEE Transactions on Visualization and Computer Graphics*, 10(6), 719–729. <https://doi.org/10.1109/TVCG.2004.48>
- Weisstein, E. W. (n.d.). Runge-Kutta Method. Text. <http://mathworld.wolfram.com/Runge-KuttaMethod.html>. Accessed 29 September 2015
- Wolfram, S. (1983). Statistical mechanics of cellular automata. *Reviews of Modern Physics*, 55(3), 601–644. <https://doi.org/10.1103/RevModPhys.55.601>
- Zhang, Z. (2000). A flexible new technique for camera calibration. *IEEE Transactions on Pattern Analysis and Machine Intelligence*, 22(11), 1330–1334. <https://doi.org/10.1109/34.888718>
- Zhao, Y. (2008). Lattice Boltzmann based PDE solver on the GPU. *The visual computer*, 24(5), 323–333.

APPENDIX A

INVENTION DISCLOSURES

INVENTION DISCLOSURE:

IP-1353: DEVELOPMENT OF A PORTABLE DEVICE FOR CHARACTERIZATION, IDENTIFICATION, AND QUANTIFICATION OF BACTERIA IN AQUEOUS SYSTEMS AS WELL AS DIFFERENTIATION FROM PARTICLES AND OTHER BACTERIA USING DIGITAL HOLOGRAPHY

Invention ID: **IP-1353**



Title: **Development of a portable device for characterization, identification, and quantification of bacteria in aqueous systems as well as differentiation from particles and other bacteria using digital holography**

Technology ID: **1353**

Type: **Software/Copyright**

Submitted By: **Jessica Silvaggi**

Updated Date: **10/25/2016**

Original Submitted Date: **3/19/2013**

Last Submitted Date: **3/19/2013**

Stage: **Approved**

Status: **On Hold/Active**

Description

Brief Overview of Invention/Work

It is a portable device that allows water to go through the system and is capable of identifying and quantifying bacteria and protozoan in situ

Confidential Description

The concept of this new portable device is two-fold: a flow-through mesoscale fluidic + handheld device. This portable device consists of a commercial CCD sensor chip (e.g., Model: MT9P031, Micron Technology) used in smartphones, which has a pixel size of 2.2 μm and an active area of $\sim 24 \text{ mm}^2$, and depth of field of 2 mm. The water sample is pumped through the mesoscale device and is retained in the device for $\sim 2 \text{ s}$ for imaging acquisition at 30 fps and processing. Since the sample volume in the device is 0.048 ml, it would take 6.9 min to get a representative sample of 10 ml. Digital in-line holography is proposed for processing the images. This is a two-step process. In the first step, an in-line hologram on a digital recording medium is recorded. In the second step, the numerical reconstruction is performed. In Dr. Strickler's lab, holography is used as a standard procedure for analyzing images of larger organisms (e.g., daphnia) (Malkiel et al, 2003). Movement of E. coli will be tracked and E. coli will be differentiated from particles and other organisms either by morphology or by its well-known swimming patterns (Watarai et al. 2010).

Key words for prior art and literature searches

bacteria, fluidic, digital holography

Inventor-Author Home Address

Inventor (1) Name, Home Address, & Citizenship

Marcia R. Silva - 2503 E Fenway Dr Oak Creek, WI 53154 - Brazilian
Thomas Hansen - 3370 S New York Ave. Milwaukee, WI 53207 - American

Inventor (2) Name, Home Address, & Citizenship

Rudi Strickler - Swiss

David Garman - Australian

Inventor (3) Name, Home Address, & Citizenship

Conception and Reduction

Conception Date/Date of Authorship

2/12/2013

First Reduction to Practice (Inventions Only)

2/12/2013

Public Discl.

Has there been any full or partial disclosure?

N

If yes, disclosure date

If yes, describe disclosure

If yes, was there a confidentiality agreement?

N

If yes, list names of persons or companies

Future Discl.

Are there any future plans to disclose?

N

If yes, future disclosure date

If yes, describe future disclosure

Background Information

Are lab/research records available?

Not at this stage; we have worked on the concept only.

Are related patents known to inventor/author?

No

Relevant publications-abstracts of other authors

Lee, M., O. Yaglidere and A. Ozcan (2011). "Field-portable reflection and transmission microscopy based on lensless holography." *Biomedical Optics Express* 2(9): 2721-2730.
Lee, S. A., G. Zheng, N. Mukherjee and C. Yang (2012). "On-chip continuous monitoring of motile microorganisms on an ePetri platform." *Lab Chip* 12: 2385-2390.
Watari, N. and R. G. Larson (2010). "The hydrodynamics of a run-and-rumble bacterium propelled by polymorphic helical flagella." *Biophysical Journal* 98(1): 12-17.

List your own related publications

Malkiel, E., J. Sheng, J. Katz and J. R. Strickler (2003). "The three-dimensional flow field generated by a feeding calanoid copepod measured using digital holography." *The Journal of Experimental Biology* 206: 3657-3666.
Silva, M. R., Q. Liao, S. L. McLellan, H. R. Bravo. "Novel Optical-Based Method for Assessment of green fluorescent protein (GFPuv)-labeled *Escherichia coli* in modeled aqueous systems". *Environmental Science and Technology*. Under Review.

Other Agreements

List agreements related to the invention/work

None

Did invention-work use materials from others?

No

Stage of Development

Stage of Development/Completion

concept only

Have the products been made, written or tested?

N

Test Date

Comments

Commercial Applications

Novel and unusual features and advantages

1- This novel system combines the idea of a flow-through mesoscale fluidic + handheld sized device, allowing the flexibility of real-time measurements as well as longer term monitoring installation
2- Assessment of smaller organisms (e.g., bacteria) due to higher pixel densities of CCDs and increasing computer power

Problem(s) this invention/work solves?

This device allows near real-time determination of *E. coli*, which is a fecal indicator bacteria established by EPA as the standard indicator organism for beach closings. Current standard microbiological measurement techniques take 24 hours to produce results which often is not timely enough to reflect current beach conditions

Products and Services

handheld beach health monitoring device; handheld water quality monitoring for a variety of bacteria and protozoan in environmental flows and water treatment plant;

Disadvantages to invention/work

Current challenges include handling sufficient volumes in a convenient time frame. We are hopeful that the ongoing increases in both CCD pixel resolution and computer power will address these challenges.

Competing Products and Services

There are several companies that commercialize flow cytometers in which fluorescent bacteria can be observed and quantified, but in all cases samples have to be collected from the study site and tested at the equipment. Applied biosystems (<http://www.appliedbiosystems.com/absite/us/en/home.html>), Fluxion Biosciences (<http://www.fluxionbio.com/about-us/about-fluxion/>), Beckman Coulter (<http://www.beckmancoulter.com>), Millipore (<http://www.millipore.com/>)
This can also potentially compete with molecular techniques such as real time PCR (qPCR) and digital droplet PCR (ddPCR)

Advantages

1- This novel system combines the idea of a flow-through mesoscale fluidic + handheld sized device, allowing the flexibility of real-time measurements as well as longer term monitoring installation
2- Assessment of smaller organisms due to higher pixel densities of CCDs and increasing computer power

Potential Licensees

Bio-Rad - www.bio-rad.com
Fisher Scientific - www.fishersci.com/
Applied biosystems - <http://www.appliedbiosystems.com>

Personal Interest

Inventors-authors interested in Start-Up company?

Yes

Have inventors-authors actually formed a company?

No

Inventors

Inventors

First Name	M	Last Name	Email	Significance	Contribution	Role Type	Address	Working For Company	Working For Department
Marcia	R	Silva	msilva@uwm.edu	1	30.00 %		2503 E Fenway Dr Oak Creek WI United States of America		
Thomas	F	Hansen	tomh@uwm.edu	2	30.00 %		600 E Greenfield Ave Milwaukee WI United States of America		
J. Rudi		Strickler	jrs@uwm.edu	3	20.00 %		Global Water Center Milwaukee Wisconsin United States of America		
David		Garman	dgarman@thewatercouncil.com	4	20.00 %		19 Russell Avenue Lindfield – Australia		Freshwater Sciences

Remarks

Remarks

By	Comment	Date Added
Jessica Silvaggi	Dear Inventors, Thank you very much for this exciting submission and catalyst grant. Since this is concept only at this time, we are going to categorize your invention as "pre-invention" in our system. This means the invention is on hold as we await further data and work on the project and aligns with the decisions for the catalyst grant and next steps in choosing which submissions make it to the next round. We will check back in with you over the upcoming months to learn of any new progress with the research. If there are any new data developments please contact us and we can add these to your disclosure file to reassess the status. Thank you again for your invention and we look forward to learning more, Best, Jessica Silvaggi	3/19/2013

Agreements

Agreements

Agreement ID	Title	Party	Type	Status	Effective	Updated
Option-21-042	(OTT1353) Option/Eval Ecoli Sense	Ecoli Sense	Option Agreement	Negotiating		
CDA/NDA-21-271	(OTT1353) CDA Ecoli Sense	Ecoli Sense	Confidentiality (CDA/NDA)	Negotiating		
MTA-18-156	(OTT1353) MTA Stonehouse	Stonehouse Water Technologies	Material Transfer (MTA)	Inactive		
N-Excl Lic-17-004	(OTT1335) Stonhouse Non Excl License	Stonehouse Water Technologies	Non-exclusive License (N-Excl)	Inactive		
Assign-17-124	Development of a portable device for characterization, identification, and quantification of bacteria in aqueous systems as well as differentiation from particulates and other bacteria using digital holography	Marcia R, Silva, Thomas F, Hansen	Assignment	Active	1/10/2017	

Documents

Documents

File Name	Created By	Date Created
-----------	------------	--------------

Interests

Interests

Computational Modeling, Engineering, Environmental Science, Fluid Mechanics, Freshwater Science, Health Science, Life Science Products, Microbiology, Microscopy/Microscope accessories, Particle Analysis, Pollution Monitoring, Scientific Instrumentation

Marketingtargets

MarketingTarget

Company	Contact	Email
Bio-Rad Laboratories, Inc		
Fisher Scientific		
Applied Biosystems		

Funding

Funding

Grant / Contract No	Title	Granted Date	Funding Institution	Investigator
---------------------	-------	--------------	---------------------	--------------

Patents

Patents

--	--	--	--	--

App No.	Patent No.	Internal ID	Title	Country	Type	Status	Filed Date	Issued Date	Updated Date
---------	------------	-------------	-------	---------	------	--------	------------	-------------	--------------

Per the UWM System Administrative Policy with respect to Intellectual Property Rights, I (we) hereby disclose this invention to the University of Wisconsin, Milwaukee ("UW-Milwaukee") and declare that this invention disclosure is complete and accurate to the best of my (our) knowledge.

This electronic signature is considered a legal and official signature for your disclosure.

Not signed yet

 Marcia R Silva (30.00 %) Date

Not signed yet

 Thomas F Hansen (30.00 %) Date

Not signed yet

 J. Rudi Strickler (20.00 %) Date

Not signed yet

 David Garman (20.00 %) Date

Not signed yet

 Witness Signature Date

Not signed yet

 Witness Signature Date

INVENTION DISCLOSURE

**IP-1417: LIVE INTERACTIVE FLUID DYNAMICS INSTALLATION USING
PROJECTED DISPLAY AND SHADOWS**

Invention ID: **IP-1417**

Title: **Live Interactive Fluid Dynamics Installation Using Projected Display and Shadows**



Technology ID: **1417**

Type: **Software/Copyright**

Submitted By: **Thomas Hansen**

Updated Date: **11/18/2014**

Original Submitted Date: **9/14/2014**

Last Submitted Date: **9/14/2014**

Stage: **Approved**

Status: **Active**

Description

Brief Overview of Invention/Work

In short, the installation projects a computer-generated depiction of fluid flow against a wall or other surface. When any object is placed in the path of the projector beam, casting a shadow in the image, the fluid flow changes to seeming flow around the shadow. Large embodiments can allow participants to walk in front of the image and see the fluid swirl and flow around their silhouettes. In addition, objects of interest such as airfoils, models of fish, etc., can be suspended by fine wires and flow can be observed around these objects. If the projected surface is a whiteboard, shapes can be drawn on the whiteboard in dark marker, or dark refrigerator magnets could be used on a magnetic surface.

Confidential Description

The invention is a combination of several existing technologies. I used an existing open-source computational fluid dynamics program, which already allowed the user to manually draw fluid flow obstructions on screen with a mouse. I then combined that with code that I wrote, which uses the open-source OpenCV library to obtain real-time images from a webcam. The webcam is trained on the projected output from the fluid dynamics code, which my code then uses to detect shadows, which my code then feeds back into the model in real-time, and creates fluid-flow obstructions matching the shape and location of the shadows. This creates the appearance of the fluid flowing around the shadows.

The fluid dynamics piece was derived from the work described here:
<http://physics.weber.edu/schroeder/fluids/>

The shadow-interaction piece was inspired by the work of Scott Snibbe, specifically this installation which I saw at the Milwaukee Art Museum:
<http://www.snibbe.com/projects/interactive/deepwalls>

I did just this evening find this page. No description beyond the title, and no other information beyond the photo was found.
http://www.tripadvisor.com/LocationPhotoDirectLink-g60974-d267159-69583997-Buffalo_Museum_of_Science-Buffalo_New_York.html

Key words for prior art and literature searches

Scott,Snibbe, Computational Fluid Dynamics, Interactive Art, Interactive Simulations

Inventor-Author Home Address

Inventor (1) Name, Home Address, & Citizenship

Thomas F. Hansen
3370 S. New York Ave.
Milwaukee, WI 53207

Inventor (2) Name, Home Address, & Citizenship

Inventor (3) Name, Home Address, & Citizenship

Conception and Reduction

Conception Date/Date of Authorship

9/8/2014

First Reduction to Practice (Inventions Only)

9/12/2014

Public Discl.

Has there been any full or partial disclosure?

Y

If yes, disclosure date

9/12/2014

If yes, describe disclosure

Demonstration display at the School of Freshwater Sciences open house, Sept 12-13.

If yes, was there a confidentiality agreement?

N

If yes, list names of persons or companies

Future Discl.

Are there any future plans to disclose?

Y

If yes, future disclosure date

If yes, describe future disclosure

I intend at the very least to publish a paper on this installation, I may also apply for grant funding to further this work.

UWM press photographers were at the SFS open house and took photos of the installation.

Background Information

Are lab/research records available?

Source codes-- project went from conception to first reduction in 5 days.

Are related patents known to inventor/author?

not known

Relevant publications-abstracts of other authors

The fluid dynamics piece was derived from the work described here:
<http://physics.weber.edu/schroeder/fluids/>

The shadow-interaction piece was inspired by the work of Scott Snibbe, specifically this installation which I saw at the Milwaukee Art Museum;
<http://www.snibbe.com/projects/interactive/deepwalls>

I did just this evening find this page. No description beyond the title, and no other information beyond the photo was found.
http://www.tripadvisor.com/LocationPhotoDirectLink-g60974-d267159-69583997-Buffalo_Museum_of_Science-Buffalo_New_York.html

List your own related publications

I presented this at the SFS open house but there were no written materials outside of a simple sign.

Other Agreements

List agreements related to the invention/work

n/a

Did invention-work use materials from others?

yes

Stage of Development

Stage of Development/Completion

A first reduction has been completed and demonstrated at a public event, with very positive feedback. Invention could stand exactly as-is and be usable, as demonstrated. However, product currently is not in a state to be installed by an end user. There are also some very important features, such as allowing moving shadows to impart momentum onto the simulated fluid, which are almost a requirement for this simulation to be considered complete.

Have the products been made, written or tested?

Y

Test Date

Comments

Demonstration was a runaway success. Small children at times mobbed the screen, delighting in the fluid particles flowing around their shadows. Several architects, engineers and educators expressed keen interest also.

Commercial Applications

Novel and unusual features and advantages

It is the application of a scientifically relevant computational model to an interactive display which allows real-world objects to interact with the model in real time. This has great potential as a teaching tool, giving participants the opportunity to develop an intuitive sense of how the fluid model behaves. It could also have scientific and industrial uses as a quick-prototyping tool, as physical drawings or even actual physical models can be placed in the projection beam to give an immediate idea of flow around objects.

Problem(s) this invention/work solves?

Computational Fluid Dynamics (CFD) encompasses a very important class of computational tools which are used in everything from airplane design to building architecture. Yet -- as evidenced by the feedback I received during the demonstration -- many people, even professionals in design fields -- are either unappreciative of the power of this technology, or simply unaware of its existence entirely. I had one mother of two small children (who were frolicking in front of the display as we spoke) carefully write down the term "computational fluid dynamics" so she could look it up when she got home. At the same time, a professor of architecture expressed a keen interest in showing this to his students.

Products and Services

- Classroom demonstrations
- Temporary or permanent installation in school/museum/public place (airports anyone!?)
- Quick prototyping tool for engineers

Disadvantages to invention/work

Physical limitations: It needs a somewhat light-controlled environment. Would not work outside or in front of open windows, for example. But that's pretty much true of any front-projection display anyway.

IP limitations: The incorporation of multiple pre-existing technologies, and a possible prior reduction of a nominally similar idea, may limit patent potential.

Competing Products and Services

Possible nominally similar installation:
http://www.tripadvisor.com/LocationPhotoDirectLink-g60974-d267159-69583997-Buffalo_Museum_of_Science-Buffalo_New_York.html

Advantages

Potentially very inexpensive: Existing embodiment consists of a laptop, projector, USB webcam. Schools already have these, cost could be simply the software.

Potential Licensees

Museums, schools, airports, other public entities who display art.
Engineering firms.

Personal Interest

Inventors-authors interested in Start-Up company?

possibly

Have inventors-authors actually formed a company?

no

Inventors

Inventors

First Name	MI	Last Name	Email	Significance	Contribution	Role Type	Address	Working For Company	Working For Department
Thomas	F	Hansen	tomh@uwm.edu	1	100.00 %		600 E Greenfield Ave Milwaukee WI United States of America		

Remarks

Remarks

By	Comment	Date Added

Agreements

Agreements

Agreement ID	Title	Party	Type	Status	Effective	Updated
N-Excl Lic-17-006	(OTT1417) Non-Excl license Agreement Hansen Atomic Creations	Thomas F. Hansen, Atomic Creations, LLC	Non-exclusive License (N-Excl)	Active	10/23/2017	
N-Excl Lic-17-001	(OTT1417) Exclusive License Science Kinetics	Science Kinetics	Non-exclusive License (N-Excl)	Active	8/10/2016	8/10/2016
MTA-16-136	(MTA) Software Use AVI	AVI Systems Inc,	Material Transfer (MTA)	Expired		
CDA/NDA-15-121	(OTT1417) NDA Pradeep-IcTect	Pradeep Jain	Confidentiality (CDA/NDA)	Expired		
Assign-15-092	(OTT1417) Assignment	Thomas F. Hansen	Assignment	Active	3/13/2015	3/13/2015

Documents

Documents

File Name	Created By	Date Created

Interests

Interests

Marketingtargets

MarketingTarget

Company	Contact	Email

Funding

Funding

Grant / Contract No	Title	Granted Date	Funding Institution	Investigator

Patents

Patents

App No.	Patent No.	Internal ID	Title	Country	Type	Status	Filed Date	Issued Date	Updated Date
62/133,028		1417-US00	Live Interactive Fluid Dynamics Installation Using Projected Display and Shadows	United States of America	Provisional [PPA]	Abandoned	3/13/2015		3/15/2015
1-3834541501	TXu 2-023-324	1417-USCopy	The Immersive Fluid Flow Experience	United States of America	Copyright [CR]	Issued - Copyright	7/21/2016	7/21/2016	3/1/2017

Per the UWM System Administrative Policy with respect to Intellectual Property Rights, I (we) hereby disclose this invention to the University of Wisconsin, Milwaukee ("UW-Milwaukee") and declare that this invention disclosure is complete and accurate to the best of my (our) knowledge.

This electronic signature is considered a legal and official signature for your disclosure.

Digitally signed on 9/23/2014

Thomas F Hansen (100.00 %)

Date

Digitally signed on 9/23/2014

Witness Signature

Date

Digitally signed on 9/23/2014

Witness Signature

Date

INVENTION DISCLOSURE:

**IP-1422: A LOW-COST DEVICE FOR QUANTIFYING WATER CURRENTS AND
WAVE HEIGHTS**

Invention ID: **IP-1422**

Title: **A low cost device for quantifying water currents and wave heights**



Technology ID: **1422**

Type: **Software/Copyright**

Submitted By: **Matthew Smith**

Updated Date: **2/12/2016**

Original Submitted Date: **10/6/2014**

Last Submitted Date: **10/6/2014**

Stage: **Approved**

Status: **Closed**

Description

Brief Overview of Invention/Work

A small cost effective system to that logs water velocity is being developed. The battery powered system comprises of a microcontroller, accelerometer, digital compass, non volatile memory, and realtime clock. Custom software enables analysis of water velocity to be determined following retrieval of the device or data transmission. The system has been developed using predominantly off the shelf parts.

Confidential Description

A small cost effective system to that logs water velocity is being developed. The battery powered system comprises of a microcontroller, 3 axis accelerometer, digital compass, non volatile memory, and realtime clock. Custom software enables analysis of water velocity to be determined following retrieval of the device or data transmission. The system has been developed using predominantly off the shelf parts. This system has application in water current monitoring and wave height determination. The system can operate as a subsurface tethered instrument or as a free floating instrument or surface tethered instrument. Where the system is free floating, GPS capability can be added.

Key words for prior art and literature searches

water velocity, accelerometer

Inventor-Author Home Address

Inventor (1) Name, Home Address, & Citizenship

Dr. Matthew C. Smith
5130 N Berkeley Blvd
Whitefish Bay, Milwaukee WI 53217

Citizenship: Australia

Inventor (2) Name, Home Address, & Citizenship

Tom Hansen
3370 S New York Ave
Milwaukee WI 53207

Citizenship: USA

Inventor (3) Name, Home Address, & Citizenship

Dr. John Janssen
307 East Carlisle
Whitefish Bay, WI 53204

Citizenship: USA

Conception and Reduction

Conception Date/Date of Authorship

10/13/2013

First Reduction to Practice (Inventions Only)

10/28/2014

Public Discl.

Has there been any full or partial disclosure?

N

If yes, disclosure date

8/29/2014

If yes, describe disclosure

2014-2017. United States Army Corps of Engineers. Evaluate the Use, Success, and Site Characteristics of an Experimental Fish Spawning Reef Created in Milwaukee Harbor. \$249,876

2013-2015 Great Lakes Fishery Commission
DETERMINING THE SUBSTRATE COMPOSITION AND INTERNAL STRUCTURE OF GLACIAL BEDFORMS USED AS SPAWNING HABITAT BY LAKE TROUT AT DRUMMOND ISLAND, LAKE HURON. \$48510

If yes, was there a confidentiality agreement?

N

If yes, list names of persons or companies

Discussions with collaborators on the Great Lakes Fishery Commission has led to them wanting to trial the instrument. This is a usage application not a developmental application). This has included:
Steve A. Farha: USGS - sfarha@usgs.gov
Charles Kjueger: Michigan State University kruege62@msu.edu

Future Discl.

Are there any future plans to disclose?

N

If yes, future disclosure date

12/1/2014

If yes, describe future disclosure

We wish to publish in peer reviewed literature

Background Information

Are lab/research records available?

Yes

Are related patents known to inventor/author?

There probably are - as there are similar methods out there to do this type of thing

Relevant publications-abstracts of other authors

[http://nopr.niscair.res.in/bitstream/123456789/26424/1/IJMS%2043\(1\)%2045-49.pdf](http://nopr.niscair.res.in/bitstream/123456789/26424/1/IJMS%2043(1)%2045-49.pdf)
http://ieeexplore.ieee.org/xpls/abs_all.jsp?arnumber=1194298
<http://journals.ametsoc.org/doi/pdf/10.1175/2010JTECHO724.1>

List your own related publications

None as yet

Other Agreements

List agreements related to the invention/work

Working on a non disclosure for the USGS and MSU for application in lakes

Did invention-work use materials from others?

Some code has been developed using open source material from Adafruit and other sources

Stage of Development

Stage of Development/Completion

Prototype

Have the products been made, written or tested?

Y

Test Date

10/28/2014

Comments

Commercial Applications

Novel and unusual features and advantages

Inexpensive method for measuring water velocity. Uses primarily off the shelf parts and application specific software.

Problem(s) this invention/work solves?

Low cost nature enables high spatial resolution to be obtained as multiple units can be built and deployed. Removes the need for use of multiple ADCP instruments

Products and Services

Fisheries research
physical oceanography and limnology
microbial source tracking
Source transport and fate
educational outreach

Disadvantages to invention/work

currently the system does not produce real time data - data is stored on board for later analysis

Competing Products and Services

Waverider buoy, Wave Track etc (are examples of wave height systems) not aware of similar commercial products that measure water velocity underwater.

Advantages

Removes the need for use of multiple ADCP instruments.

Potential Licensees

YSI, NorTec and other environmental sensor manufacturers

Personal Interest

Inventors-authors interested in Start-Up company?

No **

Have inventors-authors actually formed a company?

No

Inventors

Inventors

First Name	MI	Last Name	Email	Significance	Contribution	Role Type	Address	Working For Company	Working For Department
Matthew	C	Smith	matthew.c.smith1@gmail.com	1	50.00 %		Milwaukee Wisconsin United States of America		Freshwater Sciences
Thomas	F	Hansen	tomh@uwm.edu	2	35.00 %		600 E Greenfield Ave Milwaukee WI United States of America		Freshwater Sciences
John	A	Janssen	jjanssen@uwm.edu	3	15.00 %		University of Wisconsin-Milwaukee GLRF Main Building 117/169 Milwaukee Wisconsin United States of America		

Remarks

Remarks

By	Comment	Date Added
----	---------	------------

Agreements

Agreements

Agreement ID	Title	Party	Type	Status	Effective	Updated
--------------	-------	-------	------	--------	-----------	---------

Documents

Documents

File Name	Created By	Date Created
OTT1422_equity_review.pdf	Mark Doremus	10/7/2014

Interests

Interests

Marketingtargets

MarketingTarget

Company	Contact	Email
---------	---------	-------

Funding

Funding

Grant / Contract No	Title	Granted Date	Funding Institution	Investigator
---------------------	-------	--------------	---------------------	--------------

Patents

Patents

App No.	Patent No.	Internal ID	Title	Country	Type	Status	Filed Date	Issued Date	Updated Date
---------	------------	-------------	-------	---------	------	--------	------------	-------------	--------------

Per the UWM System Administrative Policy with respect to Intellectual Property Rights, I (we) hereby disclose this invention to the University of Wisconsin, Milwaukee ("UW-Milwaukee") and declare that this invention disclosure is complete and accurate to the best of my (our) knowledge.

This electronic signature is considered a legal and official signature for your disclosure.

Digitally signed on 10/6/2014
 Matthew C Smith (50.00 %) _____ Date

Not signed yet
 Thomas F Hansen (35.00 %) _____ Date

Not signed yet
 John A Janssen (15.00 %) _____ Date

Digitally signed on 10/6/2014
 Witness Signature _____ Date

Digitally signed on 10/6/2014
 Witness Signature _____ Date

INVENTION DISCLOSURE:

IP-1668: NOVEL METHOD OF MEASURING WATER CURRENT ON OPEN ENVIRONMENTAL IN-SITU SENSORS VIA ANALYSIS OF VORTEX SHEDDING AND TURBULENCE-INDUCED VIBRATIONS OF A BLUFF BODY USING A TRAINED DEEP NEURAL NETWORK

Invention ID: **IP-1668**



Title: **Novel method of measuring water current in open environmental in-situ sensors via analysis of vortex shedding and turbulence induced vibrations of a bluff body using a trained deep neural network.**

Technology ID: **1668**

Submitted By: **Thomas Hansen**

Original Submitted Date: **7/23/2019**

Stage: **Approved**

Type: **Patent-based Disclosure**

Updated Date: **7/24/2019**

Last Submitted Date: **7/23/2019**

Status: **Approved**

Technology and Invention Description

Brief Overview of the Technology

This is a very inexpensive device that can measure water current speed in open waters such as in streams, rivers, lakes, and oceans. It has a potential cost that is a small fraction of currently available technology.

Invention features seeking protection

This technology uses a single-board 2-, 3-, 6-, or 9-axis motion/orientation sensor embedded in a submersible package, along with a trained convolutional neural network (CNN). Data recorded by the sensor is analyzed by the CNN to infer the speed and direction of the water flowing around the submersible package. The invention, however, includes the design details of the CNN, as well as the data processing and CNN training procedure, which must be done to produce a trained CNN which is capable of performing the necessary calculations.

Invention Conception Date

3/23/2019

Invention Reduction to Practice

Provide details on the current stage of development of the invention.

A series of proof-of-concept experimental trials using a physically similar device have been successfully carried out. See "related patents or publications" for more information.

Funding (Grants, Govt. Funding or any External Funding) Please write N/A, when not applicable.

Publications and Disclosures

Are related patents or publications known to the inventor(s)?

The Lowell Instruments TCM-1 (<https://lowellinstruments.com/products/tcm-1-tilt-current-meter/>) operates in a physically similar fashion. It consists of a 6-axis (3-axis accelerometer (gravity sensor) + 3-axis magnetometer (compass)) embedded in a submersible float. That device calculates water current speed by taking a moving average of the sensor readings and estimating the average tilt of the device using these moving averages. The disclosed invention basically takes an opposite approach, and subtracts the average from the signal, and uses a trained convolutional neural network to infer the speed of the water current by analyzing the high-frequency spectral components of the signal which are left over after the moving average is subtracted. It basically exclusively relies on the portion of the signal that the TCM documentation specifically says must be filtered out.

There is also a company marketing very similar-sounding technology, but for a differing purpose: <https://reality.ai/machine-learning-for-sensors-and-signal-data/> Unknown if their technology is actually substantially similar "under the hood".

Related Publications by the inventor(s)

Dissertation in progress hypothesizes that such a device is possible, details the experimental trials, and puts forth the argument that the experimental trials demonstrate that the construction of such a device is possible.

If yes, disclosure date

6/14/2019

If yes, describe the disclosure

The rough concept was described in an oral presentation at a scientific conference (IAGLR) on 6/13/2019. The abstract below was published in the conference program. Note that the abstract was submitted when the concept for this disclosure was not yet fully conceived; that concept being the use of a convolutional neural network to enable the higher-frequency signal to stand on its own as a reliable measuring tool, and not just as a method to verify that the tilt calculation is in the ballpark.

Tilt-based current meters are increasingly popular and inexpensive, with wide application. Unlike acoustic-based sensors, which by and large have no external moving parts, tilt-based meters rely on the free movement of a tethered subsurface float. While giving the meter high sensitivity, at extremely low cost, it leaves the device susceptible to physical disruption by collision with vessels, entanglement in deployment lines, and so on. Any contact with such foreign objects renders the accuracy of subsequent readings in doubt, potentially rendering a sensor's data unusable. Fortunately, we discovered a straightforward method to validate the accuracy of data obtained from a tilt-based current meter. Inspired in part by the much smaller industrial vortex-shedding flow meter, we performed spectral analysis on the high-frequency component of the motion data recorded by the sensor—normally filtered out—and were able to identify a portion of the signal as attributable to vortex shedding. The linear relationship between vortex shedding frequency and current speed, although only useful in a limited range of speeds, was sufficient to validate the accuracy of the recorded data. We will also investigate whether more advanced spectral analysis techniques, such as the Hilbert-Huang Transform, will allow the extraction of more meaningful information from data heretofore discarded as noise.

Has there been any full or partial disclosures?

Y

Are there any future publication or disclosure plans?

N

If yes, future disclosure date

If yes, describe the future disclosure

Initial Meeting Availability

Initial Meeting Option 1

7/29/2019

Initial Meeting Time Option 1

1300

Initial Meeting Option 2

8/12/2019

Initial Meeting Time Option 2

1300

Meeting Availability Comments

I'm actually much more flexible than just those two dates. Just call me, we'll figure out a time.

Commercialization

Commercial Applications

Aquatic ecosystem research, water utilities, fishery management, natural resource management in general, input for interactive displays(!)

Agreements

Agreements (MTA, CDA or any other) at the time of the invention or ongoing ? Please write N/A, when not applicable.

Inventors

Inventors

First Name	MI	Last Name	Email	Significance	Contribution	Role Type	Address	Working For Company	Working For Department
Thomas	F	Hansen	tomh@uwm.edu	1	100.00 %		600 E Greenfield Ave Milwaukee WI United States of America		

Documents

Documents

File Name	Created By	Date Created
-----------	------------	--------------

Technology

Technology

Tech ID	Title	Manager	Status	Disclosure Date	Status Date
1668	Novel method of measuring water current in open environmental in-situ sensors via analysis of vortex shedding and turbulence induced vibrations of a bluff body using a trained deep neural network.	Smruti Patil	On Hold - Active	7/24/2019	12/21/2020

Remarks

Remarks

By	Comment	Date Added
Jessica Silvaggi	Tom, thanks for the invention disclosure. Can you email me the abstract from the conference and any other write ups you have for this work? Then I can approve. Thanks! Jessica jessica@uwmrf.org	7/23/2019

Interests

Interests

Per the UWM System Administrative Policy with respect to Intellectual Property Rights, I (we) hereby disclose this invention to the University of Wisconsin, Milwaukee ("UW-Milwaukee") and declare that this invention disclosure is complete and accurate to the best of my (our) knowledge.

This electronic signature is considered a legal and official signature for your disclosure.

Digitally signed on 7/24/2019

Thomas F Hansen (100.00 %)

Date

Digitally signed on 7/24/2019

Witness Signature

Date

Digitally signed on 7/24/2019

Witness Signature

Date

INVENTION DISCLOSURE:

**IP-1711: NOVEL DEEP LEARNING-BASED IMAGE-BIO-NANOTECHNOLOGY
SENSOR FOR RAPID DIAGNOSIS TEST OF VIRUS USING SALIVA**

Invention ID: **IP-1711**



Title: **Novel deep learning-based image-bio-nanotechnology sensor for rapid diagnostic test of virus using saliva**

Technology ID: **1711**

Submitted By: **Marcia Silva**

Original Submitted Date: **4/6/2020**

Stage: **Approved**

Type: **Patent-based Disclosure**

Updated Date: **4/30/2020**

Last Submitted Date: **4/6/2020**

Status: **On Hold/Active**

Technology and Invention Description

Brief Overview of the Technology

Our research team has conceived a novel deep learning-based image-bio-nanotechnology sensor for rapid diagnostics of viruses in saliva. This is a technology platform that can be adapted to be selective to a specific virus of interest. In this case, due to the pandemic crisis worldwide, we will focus on a sensor for detection of SARS-CoV-2, which causes COVID-19 acute respiratory disease.

Invention features seeking protection

(a) methods of nanofabrication of nanochannels (height of 250 nm and width of 1 μ m) on polydimethylsiloxane (PDMS) layers on glass microscopic slides.
(b) methods of functionalization of the internal surfaces of nanochannels with the biomarker of interest. In this case, the best candidate antibody identified is Anti-SARS-CoV-2 envelope protein antibody - Coronavirus (ab272503). Other antibodies may be tested independently or combined for best efficiency.
(c) methods of increasing contact time between saliva sample and biomarker. This will be accomplished by nanochannels and functionalization of their walls with proper biomarker.
(d) The application of deep machine learning to the holographic detection of nanoparticles and viruses by neural classification of the Rayleigh scattering of an incident coherent light source by such particles. The physical size of virus, the SARS-CoV-2 virus in this study, makes it difficult to image using traditional optical techniques. However, we do not propose a system that images the virus or even attempts to calculate the physical position of virus particles with any precision within a sample volume. Rather, we propose a method to answer the much simpler question of whether the virus is present or not.

Invention Conception Date

3/27/2020

Invention Reduction to Practice

Provide details on the current stage of development of the invention.

Conception stage.

Funding (Grants, Govt. Funding or any External Funding) Please write N/A, when not applicable.

N/A

Publications and Disclosures

Are related patents or publications known to the Inventor(s)?

Related Publications by the Inventor(s)

None

If yes, disclosure date

If yes, describe the disclosure

Has there been any full or partial disclosures?

N

Are there any future publication or disclosure plans?

N

If yes, future disclosure date

If yes, describe the future disclosure

Initial Meeting Availability

Initial Meeting Option 1

4/13/2020

Initial Meeting Time Option 1

3

Initial Meeting Option 2

4/20/2020

Initial Meeting Time Option 2

Meeting Availability Comments

Commercialization

Commercial Applications

Rapid sensor for detection of virus in saliva

Agreements

Agreements (MTA, CDA or any other) at the time of the invention or ongoing ? Please write N/A, when not applicable.

N/A

Inventors

Inventors

First Name	MI	Last Name	Email	Significance	Contribution	Role Type	Address	Working For Company	Working For Department
Marcia	R	Silva	msilva@uwm.edu	1	50.00 %		2503 E Fenway Dr Oak Creek WI United States of America	University of Wisconsin-Milwaukee	WATER
Thomas	F	Hansen	tomh@uwm.edu	2	50.00 %		600 E Greenfield Ave Milwaukee WI United States of America	University of Wisconsin-Milwaukee	Freshwater Sciences

Documents

Documents

File Name	Created By	Date Created
-----------	------------	--------------

Technology

Technology

Tech ID	Title	Manager	Status	Disclosure Date	Status Date
1711	Novel deep learning-based image-bio-nanotechnology sensor for rapid diagnostic test of virus using saliva	Jessica Silvaggi	On Hold - Active	4/6/2020	11/16/2020

Remarks

Remarks

By	Comment	Date Added
----	---------	------------

Interests

Interests

Per the UWM System Administrative Policy with respect to Intellectual Property Rights, I (we) hereby disclose this invention to the University of Wisconsin, Milwaukee ("UW-Milwaukee") and declare that this invention disclosure is complete and accurate to the best of my (our) knowledge.

This electronic signature is considered a legal and official signature for your disclosure.

Digitally signed on 4/6/2020

Marcia R Silva (50.00 %)

Date

Digitally signed on 4/7/2020

Thomas F Hansen (50.00 %)

Date

Digitally signed on 4/6/2020

Witness Signature

Date

Digitally signed on 4/6/2020

Witness Signature

Date

APPENDIX B

PUBLISHED MANUSCRIPT ON HAND-HELD HOLOGRAPHIC SENSOR:

**OPTICALLY BASED BACTERIA HAND-HELD SENSOR: FROM FUNDAMENTALS
TO PROOF OF CONCEPT**



Optically Based Bacteria Hand-Held Sensor: From Fundamentals to Proof of Concept

Andrew Thompson¹ · Basil Hable¹ · Adam Honts¹ · J. R. Strickler¹ · Thomas Hansen^{1,2} · Marcia R. Silva¹

Received: 21 April 2020 / Revised: 18 June 2020 / Published online: 4 August 2020
© Springer Science+Business Media, LLC, part of Springer Nature 2020

Abstract

A prototype of a hand-held particle sensor based on digital inline holographic microscopy was developed to work as an early warning device to detect bacteria *Escherichia coli* (*E. coli*) in water within minutes. The aim of the device is to record holographic images of water samples and perform rapid analyses (less than 20 min) of these samples to give timely information about the levels of particulates, with the goal of detecting and quantifying pathogens such as *E. coli* in water samples. Using the hand-held sensor, laboratory trials were performed to compare the effectiveness of the sensor with traditional methods of detecting *E. coli* in water. To address the linearity of the sensor signal, a dilution series covering nine decades of bacterial suspensions were analyzed and a linear regression coefficient of determination (R^2) of 86.4% was revealed. Preliminary studies have shown that the sensor can detect average values of *E. coli* levels from 7 colony forming units (CFU)/mL to 10^6 CFU/mL in deionized water spiked with the bacteria. The device can be essential for accurate and precise bacteria counts in drinking water systems inline or at home. The sensor's major advantages are its portability, low cost, ease of operation, low power consumption rate, and no consumption of chemical reagents is needed to visualize and count *E. coli*.

Keywords *E. coli* · DIHM · Hand-held sensor · Optical sensor

Electronic supplementary material The online version of this article (<https://doi.org/10.1007/s11220-020-00306-2>) contains supplementary material, which is available to authorized users.

✉ Marcia R. Silva
msilva@uwm.edu

¹ UWM Water Technology Accelerator (WaTA), University of Wisconsin – Milwaukee, Milwaukee, WI, USA

² School of Freshwater Sciences, University of Wisconsin – Milwaukee, Milwaukee, WI, USA

1 Introduction

Clean and safe fresh water is vital for human health. However, the most recent World Health Organization (WHO) report [26] shows that safely managed drinking water services is available to only 5.2 billion people (71% of the global population), leading to high levels of environmental contamination and exposure to the risks of microbial infections and other waterborne diseases.

Bacterial pathogens are important targets for detection and identification for efficiently and effectively monitoring of the water quality and assurance of clean and safe water [6]. Since it is difficult, time-consuming, and expensive to test pathogens directly, the United States Environmental Protection Agency (USEPA) recommends the test of fecal indicators, which are generally not harmful themselves and indicate the possible presence of pathogenic bacteria, viruses, and protozoans [23]. USEPA recommends the test of the fecal indicator bacteria *Escherichia coli* (*E. coli*) to assess the health risk from water contact in recreational waters, for example. Standard microbiological cell culture methods—the standard plate count (SPC) and the most probable number (MPN)—are time consuming, taking 24 h for *E. coli* quantification [16].

To address the issue of long turnaround times for *E. coli* testing, the USEPA in 2012 approved the use of the qPCR DNA amplification technique for use in recreational water testing [12]. This test can be as rapid as three hours. However, it comes at a high cost: \$30,000–\$50,000 up front, plus \$8–\$15 per test, and requires qualified personnel for analysis and interpretation [26]. Therefore, both private and government sectors strongly need sensors that can detect pathogens or indicators in a fast and accurate manner. While certainly applicable in many areas of the U.S., it is out of reach for most of the underserved, poor, and remote areas, where much of the need lies.

The review of recent progress in the pathogen sensors that utilize micro- and nanofabrication technology [10], impedimetric biosensors [24], and microbiological sensing technologies [1] has been reported elsewhere. More specifically, research involving the development of technologies for the detection, observation, and removal of *E. coli* and similar organisms using rapid and potentially inexpensive technologies has been ongoing for some time. The Environmental Biotechnology Cooperative Research Centre (EBCRC) funded several projects in Australia to address the need for rapid and inexpensive bacterial detection using various technologies [2, 13]. A few developments have been described as inexpensive hand-held devices. In 2010, researchers at Kings College London created a “hand-held fluorescence detector” which utilizes a fluorescent substrate to detect *E. coli* in environmental waters [25]. In 2013, the University of Alberta announced [18] that a research lab there had succeeded in developing a method for detecting *E. coli* in water using a special chemical solution that changes color in the presence of the coliform bacteria, and uses a cell phone’s camera to record the color change and transmit the information wirelessly to the laboratory [20]. Also, in 2013, young inventor Alison Bick, recipient of the 2011 Stockholm Junior Water Prize for her work, was granted a U.S. Patent [3] for her invention of

a method for the qualitative measurement based on emission of fluorescent and phosphorescent wavelength light spectrum and image analysis of the water qualities for detection of both coliform bacteria and *E. coli*. As for the removal of *E. coli*, Parsa et al.'s [17] work with the application of electro dialysis shows promise not only for removing leachate, but also for possibly removing *E. coli*. Yet, to the best of our knowledge, no inexpensive hand-held devices for detection of bacteria in water are available on the market despite all this promising work.

Initially inspired by the work done at UCLA [15] and Harvard [7] exploring the use of digital inline holographic microscopy, our research group has been working towards developing a sensor capable of imaging and characterizing water-borne particulates, flora, and fauna, using very inexpensive components. We hope to take advantage of the growing opportunities afforded by the worldwide boom in very inexpensive, miniature electronic devices (such as smartphones), as Lvov et al. [14] did in the construction of their optical hand-held sensor for the detection of defects in aircraft structures.

Traditional lens-based approaches to microscopy require precise lens-focusing systems with lenses and other parts polished and machined to very high tolerances, to resolve objects suspended at various depths into a sample volume. By contrast, it is possible to take just one holographic image of a sample volume and then “digitally focus” on a range of focal lengths and resolve an entire sample volume [8]. The digital focusing process is somewhat like how multiple two-dimensional computed tomography (CT) scans may be combined into a large three-dimensional volume and used to detect irregularities [9]. Finally, this platform has an important advantage over all the other potential hand-held technologies: it does not consume any reagents such as fluorescent dyes, substrates, or markers. This is advantageous because it reduces the cost of testing and reduces the problem of safe and environmentally sensitive disposal of such substances.

In this study, a prototype of a hand-held particle sensor based on DIHM is developed to work as an early warning device to detect bacteria *Escherichia coli* (*E. coli*) in water within minutes. The aim of the device is to record holographic images of water samples and perform rapid analyses with the goal of detecting and quantifying pathogens such as *E. coli* in water samples. We present details of the design, calculation of sample volume and quantification of environmental *E. coli* cells using both the standard method and the novel sensor for calibration of the sensor and evaluation of its performance.

2 Materials and Methods

2.1 Components and Setup

The build requires a laser diode of a known wavelength (GeeBat Mini Laser Dot Diode Module Head Red, wavelength 650 nm, 5 V, 5 mW Diode Lasers with internal lens removed), a complementary metal-oxide-semiconductor (CMOS) sensor ‘camera’ (See3CAM_CU51—5MP Custom Lens Monochrome USB3 Camera by e-con Systems, housing an e-CAM50_CU9P031_MOD—5.0 MP MT9P031

Monochrome camera module), a 10 mm standard glass cuvette (Azzotta Part N₀-G104—pathlength 10 mm, volume 3.5 mL, optical glass—340–2500 nm) to hold the volume of liquid being examined, and a laptop (Lenovo Yoga 720-12IKB I3 4G 128G 10H, Model Name: 81B5) to process the results using software program. The components were purchased for under \$300 (ignoring the used laptop) and can be operated by a standard off-the-shelf desktop or laptop.

2.2 Design Overview

A schematic of the DIHM design is depicted in Fig. 1. Light from a laser is aimed into a cuvette holding water to be tested. The emerging spherical wave illuminates the particles present, scattering the coherent light from the laser by diffraction and produce new spherical wavefronts centered at the particles while the bulk of the original spherical wavefronts from the laser continue to the complementary metal–oxide–semiconductor (CMOS) sensor and serve as a reference beam. At the CMOS sensor surface the scattered waves interfere with the reference beam waves to produce an interference pattern or hologram.

The subsections of 2.2 focus on the calculations for determining the sample volume, the numerical aperture and resolution, and the cost of the design. For hardware specifications and power consumption rate, see Supplementary Material.

2.2.1 Determination of Sample Volume (SV)

SV is the volume of sample which is in-line between the point source and the image sensor—which is, by definition, the volume which can be accurately reconstructed using the DIHM technique. The sample volume is that portion of the sample within the cuvette in which particles can be observed by the sensor.

Figure 2 shows the physical layout of the sensor. The laser has its internal collimator lens removed—the collimator lens is what normally focuses a laser into a narrow beam—and so in its absence the coherent light emerges from the laser package as a roughly conical section of a spherical wave. The dotted inner portion of the laser emission depicts that portion of the laser light which is destined to strike the sensor.

Figure 3 is a closeup detail of Fig. 2 in the vicinity of the CMOS sensor, showing how the laser light passes through the cuvette and onto the CMOS sensor. It also

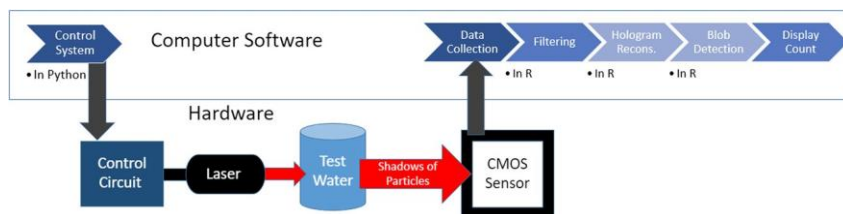


Fig. 1 The particle sensor design

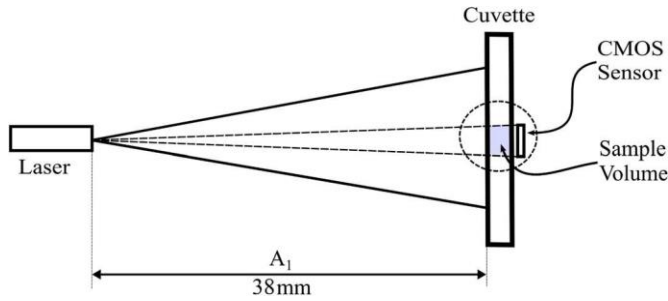


Fig. 2 Schematic of optical sensor profile

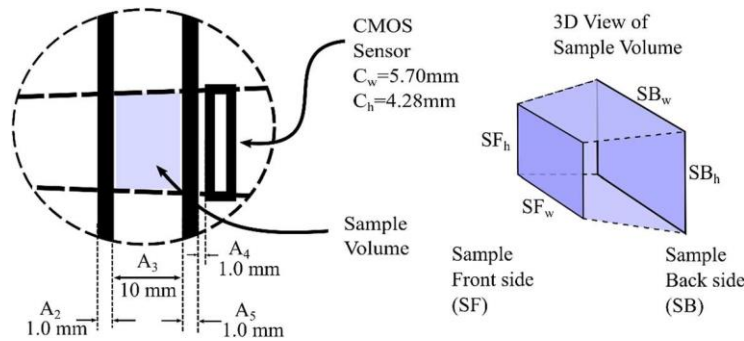


Fig. 3 Detail of sample volume within the cuvette, and the CMOS sensor

shows the 3D view of the sample volume, which is in the shape of a truncated right pyramid.

Precise calculation of the SV requires considering the differing indices of refraction of the three materials that lie in the path between the laser and the sensor: air, cuvette glass, and water. Snell’s Law describes the behavior of light as it passes between two materials of differing refractive indices [4]. Following a modified version of W. Casselman’s schematic diagram (Fig. 4), it is possible to simplify equations.

By definition, $m_1 = \tan\theta_1$, and $m_2 = \tan\theta_2$ but we can make a common simplification that for very small angles θ , $\sin\theta \approx \tan\theta \approx \theta$, thus from Snell’s law (Eq. 1):

$$n_1 \sin\theta_1 = n_2 \sin\theta_2 \tag{1}$$

We can substitute $m_1 \approx \sin\theta_1$ and $m_2 \approx \sin\theta_2$ and obtain Eq. 2:

$$n_1 m_1 \approx n_2 m_2 \tag{2}$$

where m_1 and m_2 are simply the *slopes* of the lines of light with respect to the normal to the surface.

We then label the dimensions (distances, thicknesses) of our Figs. 2 and 3 as follows:

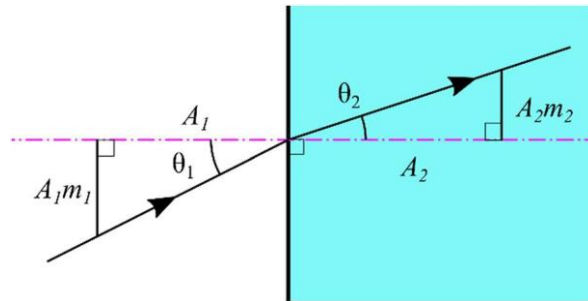


Fig. 4 Modified version of W. Casselman's diagram

- A_1 = distance from laser to cuvette (38 mm)
- A_2 = thickness of cuvette glass facing the laser (1 mm)
- A_3 = inside width of cuvette (10 mm)
- A_4 = thickness of cuvette glass on sensor side (1mm)
- A_5 = distance between cuvette glass and CMOS sensor (1 mm)
- C = width or height of CMOS sensor (5.70 mm and 4.28mm)

We then label the three indices of refraction in our system as follows:

$$\begin{aligned} n_0 &= n \text{ for air } (\approx 1.00) \\ n_1 &= n \text{ for water } (\approx 1.3325) \\ n_2 &= n \text{ for the cuvette glass } (\approx 1.5230) \end{aligned}$$

We further observe that, since $m_0 n_0 = m_1 n_1 = m_2 n_2$, that $m_1 = m_0 \left(\frac{n_0}{n_1} \right)$ and $m_2 = m_0 \left(\frac{n_0}{n_2} \right)$. Thus we can write Eq. 3:

$$C = A_1 m_0 + A_2 m_0 \left(\frac{n_0}{n_2} \right) + A_3 m_0 \left(\frac{n_0}{n_1} \right) + A_4 m_0 \left(\frac{n_0}{n_2} \right) + A_5 m_0 \quad (3)$$

And obtain Eq. 4 by rearranging Eq. 3:

$$\frac{C}{m_0} = A_1 + A_2 \left(\frac{n_0}{n_2} \right) + A_3 \left(\frac{n_0}{n_1} \right) + A_4 \left(\frac{n_0}{n_2} \right) + A_5 \quad (4)$$

Isolating m_0 , we obtain Eq. 5:

$$m_0 = \frac{C}{A_1 + A_2 \left(\frac{n_0}{n_2} \right) + A_3 \left(\frac{n_0}{n_1} \right) + A_4 \left(\frac{n_0}{n_2} \right) + A_5} \quad (5)$$

We thus can calculate, for the larger CMOS sensor width of $C = 5.70$ mm:

$$m_0 = \frac{(5.70 \text{ mm})}{(38 \text{ mm}) + (1.0 \text{ mm})\left(\frac{(1.00)}{(1.5230)}\right) + (10 \text{ mm})\left(\frac{(1.00)}{(1.3325)}\right) + (1.0 \text{ mm})\left(\frac{(1.00)}{(1.5230)}\right) + (1.0 \text{ mm})}$$

$$m_0 = 0.1192$$

The widths of both the laser-side, or front side (SF_w), as well as the back side (BS_w) of the sample volume can then be calculated, through Eqs. 6 and 7:

$$SF_w = A_1 m_0 + A_2 m_0 \left(\frac{n_0}{n_2}\right) \quad (6)$$

$$SF_w \approx 4.608 \text{ mm}$$

$$SB_w = A_1 m_0 + A_2 m_0 \left(\frac{n_0}{n_2}\right) + A_3 m_0 \left(\frac{n_0}{n_1}\right) \quad (7)$$

$$SB_w \approx 5.502 \text{ mm}$$

Following the analogous calculations for the heights resulted in a $SF_h = 3.46 \text{ mm}$ and $SB_h = 4.132 \text{ mm}$. (Also, $m_0 = 0.08951$ which we will need later.)

Finally, applying the standard, well-known formula for the volume of a truncated right pyramid (Eq. 8)

$$v = \frac{1}{3} h (a_1 + a_2 + \sqrt{a_1 a_2}) \quad (8)$$

And setting $h = A_3 = 10 \text{ mm}$, $a_1 = SF_w SF_h$, $a_2 = SB_w SB_h$, we obtained the sample volume of

$$SV \approx 192.4 \text{ mm}^3 = 192.4 \mu\text{l}$$

2.2.2 Calculation of Numerical Aperture and Resolution

The numerical aperture (NA) is an important characteristic value that allows us to calculate the resolving power of the microscope. NA is calculated as shown below in Eq. 9: [19]

$$NA = \frac{\left(\frac{W}{2}\right)}{\sqrt{\left(\frac{W}{2}\right)^2 + D^2}} \quad (9)$$

where W is the width of the sensor, and D is the distance from the point source to the plane of the sensor.

Because in this sensor, the varying indices of refraction cannot be neglected, we cannot simply use the physical distance from the laser to the sensor. We must consider the fact that the intervening material has higher refractive indices than air.

However, this is not difficult because we can use the results of the prior calculation. Since the light path begins and ends in air (corresponding to A_1 and A_5 in Figs. 2 and 3) we already know the slopes of the light envelope that strikes the sensor and can thus determine that the virtual distance to the laser light source from the sensor must be simply $\frac{C_w}{m_0} = \frac{5.70 \text{ mm}}{0.1192} \approx 47.82 \text{ mm}$. This is the value we will use for D in the NA formula.

Lateral resolution -or the smallest distance that two particles can be laterally separated and still be resolved as separate particles—is limited as shown in Eq. 10 below [19]:

$$|\mathbf{r}_2 - \mathbf{r}_1| \geq \frac{\lambda}{2\text{NA}}, \quad (10)$$

where \mathbf{r}_1 and \mathbf{r}_2 are two-point sources (particles) in the same plane and λ is the wavelength of the coherent light source (laser).

Depth resolution is limited as shown in Eq. 11 below:

$$|\mathbf{r}_2 - \mathbf{r}_1| \geq \frac{\lambda}{2(\text{NA})^2}. \quad (11)$$

where \mathbf{r}_1 and \mathbf{r}_2 are two-point sources (particles) located in a line perpendicular to the plane of the sensor and λ is the wavelength of the coherent light source (laser).

Note that since NA is always $\ll 1$, it follows that the depth resolution will always be significantly coarser than the lateral resolution.

For our sensor, the numerical aperture is calculated using the narrower of the dimensions, where $W = 4.28 \text{ mm}$ and $D = 47.82 \text{ mm}$, resulting in $\text{NA} = 0.0447064$ using Eq. 9. Also, as $\lambda = 650 \text{ nm}$ (red laser), the lateral resolution results in $7.27 \text{ }\mu\text{m}$. Similarly, the depth resolution obtained is 163.6 mm .

2.2.3 Estimation of Costs of the Novel Optical Sensor for Bacteria Detection

The cost of the optical sensor for bacteria detection at the prototype stage is under \$300 per unit. The most expensive item, the CMOS sensor, costs \$179. The 3D printed case costs \$90 including the fee to use the printer. The USB cable is \$5. A cuvette, laser diode, and other electronic parts are each under \$1. Once production surpasses 1000 units, we estimate a cost savings of around 40%, yielding a price of approximately \$200 per device. For example, the See3CAM monochrome sensor costs \$179 for one. In comparison, when bought in bulk, the cost would be \$99/unit for 1000 units, representing a 44% savings for that component.

2.3 Environmental *E. coli* Cells Preparation, Growth, and Quantification Using the Standard Method

A brief overview of this process is provided in Fig. 5. Environmental *E. coli* cells were isolated from raw activated sewage collected from the Milwaukee Metropolitan Sewerage District (MMSD) by streaking the sludge on modified m-TEC agar

Preparing Samples

- Gather Raw Activated Sewage
- Streak plates of modified m-TEC agar plates with the sewage
- 24 hours of incubation for the plate(s)
- Pick 1 colony from any of the plates and place the colony into its own tube of LB media
- 18 hours of incubation for the tube(s)
- Decimal serial dilutions



Laboratory Method

- Pump & Filter 10^{-6} to 10^{-8} for each sample
- 24-hour incubation
- Manually count

Sensor

- Run 10^{-1} to 10^{-9} for each sample
- Software counts with results in <5 mins per tube
- Near instant software count

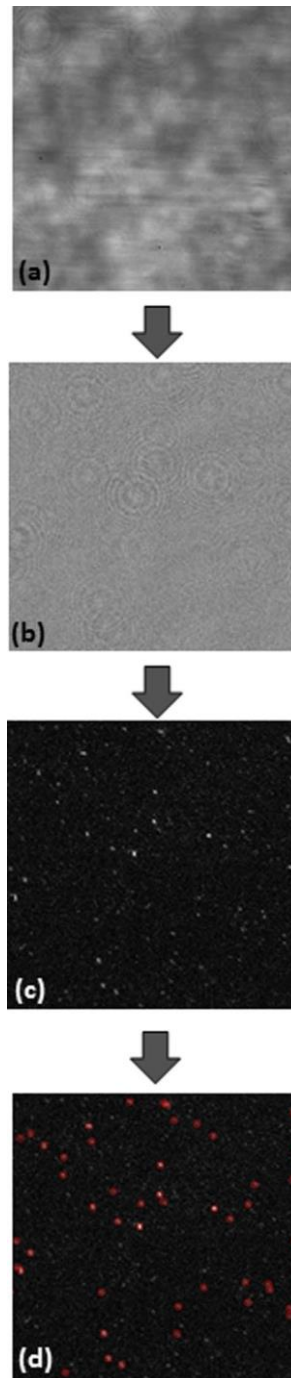
Fig. 5 A flowchart of the methods used to prepare culture of environmental *E. coli* and quantify it using EPA standard method and the novel sensor

plates (Difco, Sparkes, MD). The sludge streaked will contain many types of bacteria, however, *E. coli* will grow purple while others mostly grow white. This means *E. coli* colonies may be selected and used once grown. After twenty-four hours at 44.5 °C, one loop full of freshly grown *E. coli* was used to inoculate 5 mL of lysogeny-broth (LB) medium. *E. coli* cultures were grown for 18 h at 37 °C shaking at 160 rpm. Decimal serial dilutions were carried out in deionized (DI) water from 10^{-1} to 10^{-9} from the culture stock and prepared in 15 mL Falcon tubes. The number of Colony Forming Units (CFU) was determined in duplicate by filtering 1000- μ l aliquots from serial dilutions 10^{-6} and 10^{-8} through a 0.45- μ m-pore-size 47 mm nitrocellulose filter and placing the filters on modified m-TEC agar plates. After incubation for 24 h at 44.5 °C, CFU were counted for each plate, averaged, and expressed as CFU/mL [22].

2.4 Quantification of *E. coli* Using the Optical Sensor

Bacteria culture was drawn from each of the 15 mL tubes containing bacterial dilutions into the cuvette. A raw image (2592×1944 pixels) is acquired at 15 frames per second (Fig. 6a), followed by background subtraction to remove artifacts (Fig. 6b). These artifacts are mainly caused by the laser scattering off numerous other particles and objects present in the system, such as dust particles and other impurities present on the outside surface of the cuvette, imperfections in the focusing laser, and so on. Background subtraction was accomplished by taking several images of the sample as it moved slowly through the cuvette, and the images averaged together, and subtracting this average from each of the images. Since the subject particles

Fig. 6 Steps of image processing to count bacteria: **a** acquisition of raw image; **b** background subtraction; **c** image reconstruction; **d** detection and quantification of bacteria



and bacteria were the only objects moving while these images were taken, the result of the process produces images which contained only the deviations from the average, which almost exclusively contain the interference patterns generated by the particles in motion from frame to frame. Numerical image reconstruction is then performed, calculated in one plane at the distance from the CMOS sensor to the cuvette (Fig. 6c). It is in this process that an image is produced by reconstructing the concentric circles and bringing them into sharp focus. Figure 6c exemplars the stark sharpness achieved from image reconstruction. It is now possible to visualize particles.

The final step in the processing of images is to perform identification of particles. Even after image reconstruction, some artifacts and noise are still detectable. To differentiate between what is noise and what is *E. coli*, two additional numerical steps are performed. First, a 2D Fast Fourier Transform (FFT) is performed to rid the image of both brightness differences (and low frequency variations) as well as very fine image static (or high frequency noise). Then straightforward blob detection is performed on the image, in which continuous regions of pixels are identified, and then filtered based on overall size to identify those blobs which are most likely to represent images of *E. coli* cells. To visualize this effect, Fig. 6d shows the exact view as Fig. 6c, however each verifiable *blob* detected generates a red circle at the point where a possible image of *E. coli* was detected.

A calibration curve was then prepared using these counts graphed against the known concentrations of *E. coli* for the images recorded, in order to evaluate the performance of the sensor and to serve as a metric as our detection methods are refined and improved.

3 Results and Discussion

The following section will compare the standard method of acquiring CFU/mL counts of *E. coli*, and how the sensor obtains CFU/mL counts to evaluate how well the sensor performs given the same samples.

3.1 Calibration and Performance of the Hand-Held Particle Optical Sensor

Comparison between the bacterial concentration measured by image analysis and the bacterial counts obtained by the standard cell count method is shown in Fig. 7. Linear regression indicated that $y = 0.0066x + 8420.2$ with the coefficient of determination $R^2 = 86.9\%$, where x is concentration of cells measured in CFU/mL and y is the concentration of particles/mL, measured via image analysis with the novel sensor. The calibration curve for nine different dilutions of environmental *E. coli* in deionized water were comprised of seven trials per dilution. The concentration of cells was determined from the fresh *E. coli* cells' culture via standard cell count and the final concentration was calculated for each dilution.

To find the sensor's optimal use range, Fig. 8 was made to compare a linear trend to a power trend when the three lowest data points are removed. Comparing

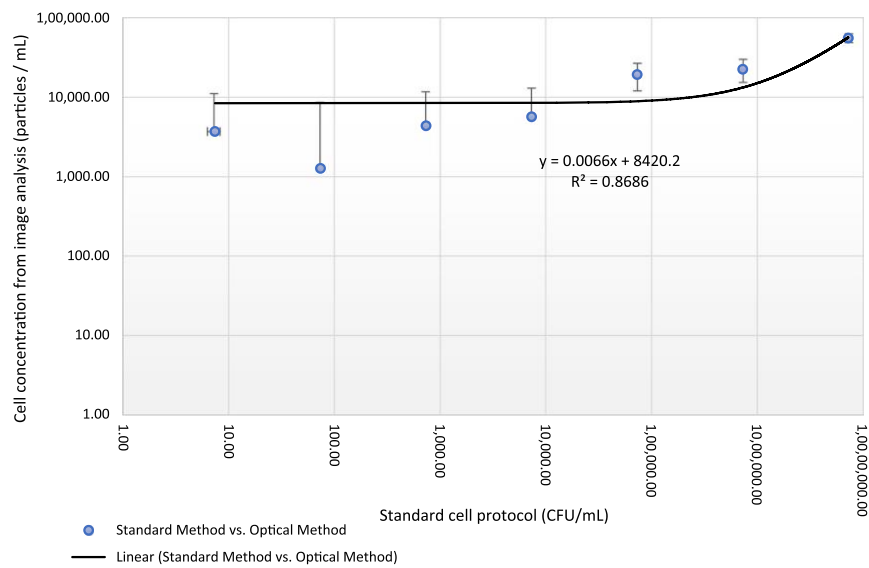


Fig. 7 A calibration curve for nine different dilutions of environmental E. coli in DI water comprised of seven trials per dilution. $R^2 = 87\%$

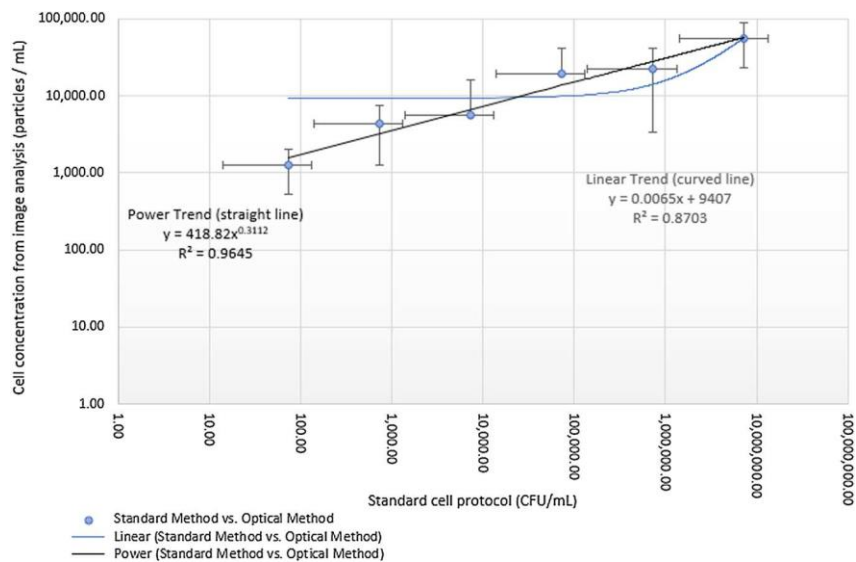


Fig. 8 A comparison between the linear trendline and the power trendline. Notice how the power trend has a higher R^2 of 96%

Figs. 8 to 7 shows a power trend has a higher R^2 (96.4%) value within the range of 7 to 10^6 CFU/mL, which is very appropriate for drinking water applications. This validates the imaging method and gives us the proof of concept for the technology. However, more trials may be ran to reduce the standard deviation.

Figure 7 shows the calibration curve by removing the two lowest data points, as they formed a plateau and including a linear trend.

The standard method, EPA Method 1603, quantifies only live and viable cells, while the novel sensor can also detect dead and viable but nonculturable cells (VBNC) (based on its optical principals). Currently, it is not capable of differentiating dead, nonculturable, or living cells (other than the ones not moving). This increase in divergence between the two methods may also be explained by increased bacterial clumping as the density of bacteria increases. As the concentration of bacteria increases, the discrepancy between the two methods increases, following a power trend. Other reasons for the results' variation include particles being misidentified as *E. coli* (be it over or under counting), and *E. coli* clinging still to the sides of the cuvette and not being counted as a result (due to the sensor only counting particles suspended and moving in the water). It is also possible that during testing, even after vortex mixing the tube for a more even distribution of particles, particles in the water may have fallen outside the sample volume, be it too high or too low, for the sensor to count. Cross contamination of the cuvette that was thoroughly washed with deionized water multiple times and then reused is possible, though, if too bad a problem, disposable cuvettes could be used (causing a non-negligible cost per use). Even with these possible complications, the sensor seems to do well. When compared to previous methods mentioned, the proposed sensor stands out. Dirk Wildeboer et al.'s work with detecting *E. coli* with a hand-held fluorescence detector works in a similar time frame of 30 min. Their work even can detect *E. coli* amounts down to 7 CFU/mL, like the proposed sensor can. However, the proposed sensor does not require enzyme markers to be added to the water like theirs does, and thus, the proposed sensor is cheaper [25]. Sushanta Mitra's work with the University of Alberta also uses a chemical solution to detect *E. coli* in water [20]. Both methods rely on chemicals that may incur long-term costs, while the proposed sensor is reusable as is.

This research represents a very important step toward rapid monitoring systems of drinking water inline or at home as the sensor has the capability of detecting very low levels of bacteria within minutes and at low cost. In addition, this technology platform has potential to be explored in a variety of fields as it has received interest from several industries spanning a wide range of applications, including as a hand-held or portable tool for governmental agency monitoring of beaches and other recreational waters, as an in situ environmental particle sensor to be deployed on buoys or subsurface marine and freshwater based sensor platforms, as a real-time monitor of well-water purity, as a low-cost detector of water-borne pathogens in highly disadvantaged contaminated areas like those found in developing countries, to detect biological and non-biological impurities in human urine samples, and to monitor the purity of intravenous (IV) solution bags.

3.2 Limitations of the System

The largest limitation of the system is the limited capability to discern *E. coli* from abiotic particles and other living bacterial particles. Currently, non-moving particles are removed and particles not within an *E. coli*'s size range are removed. This worked well enough in deionized water spiked with *E. coli*, though, may need additional work for environmental samples. In addition to deionized water, other types of clean water, such as tap water, and other types of microbial organisms, such as other bacteria, yeast, protozoa, etc. will be explored. For applications with environmental water where turbidity is high and multiple strains of bacteria and other organisms are simultaneously present, we expect to include a pre-filtration step and include other features, such as functionalization of capture surfaces with molecules with specific charge or affinity to selectively bind to the target contaminants. Future work also includes investigating various methods to increase lateral resolution, including using two or more lasers of different wavelengths as in [11, 21]; designing and constructing a robust, field-capable enclosure; and introducing more intelligent image analysis techniques to identify bacterial behavior as in [5, 21]. Next phase of research and development also includes testing the performance of the sensor with more water samples spiked with *E. coli* to build a robust database and more accurate results. Furthermore, we may reduce the dimensions of the original image (2592×1944) being captured, as only a 1024×1024 subsection of that image is later used. This would mean being able to acquire images through the CMOS sensor at 60 frames per second (at 1920×1080) rather than 15 frames per second as it is now. More frames per second would mean a smoother change in-between frames which would mean an easier time modeling the flow of particles in the cuvette.

The blob detection algorithm could also be improved. A trained convolutional neural net could identify particles that are in focus through a training set of data manually decided to be particles in focus. Programming an algorithm capable of displaying an exact count of particles in focus is an arduous process. Currently, our research group is working on using a JavaScript script to robustly tabulate particle counts more consistently.

4 Conclusions

A simple hand-held optical sensor is presented for rapid analyses of bacteria measurement in deionized water. This relatively low-cost DIHM-based optical sensor was tested in laboratory and is as effective as other particle counting devices which can be used to count *E. coli*. It is constructed of inexpensive off-the-shelf components which are readily available. This makes the sensor cheaper than most. The optical sensor is also sensitive enough to detect average *E. coli* levels from 7 CFU/mL to 10^6 CFU/mL, which is not only as good as the traditional laboratory methods, but also much faster. In addition, without using chemical markers, the proposed sensor can be ran longer, for less money. Currently, a study is under way to build a more robust database to enable more accurate measurements. With additional work, it could be used to count other bacteria and other microorganisms. This research

represents a very important step toward real-time monitoring systems for drinking water inline or at home by making accurate pathogen detection faster and more affordable.

Acknowledgements Funding was provided by Support for Undergraduate Research Fellows (SURF), University of Wisconsin-Milwaukee.

References

1. Abbasian, F., Ghafar-Zadeh, E., & Magierowski, S. (2018). Microbiological sensing technologies: A review. *Bioengineering*, 5, 20.
2. Barr, J. J., Blackall, L. L., & Bond, P. (2010). Further limitations of phylogenetic group-specific probes used for detection of bacteria in environmental samples. *The ISME Journal*, 4, 959–961.
3. Bick, A. D. (2013). *Method and apparatus for testing water quality using a cell-phone application, mirror and plastic bag*. US Patent US8442661B2. June 2013. Retrieved January 15, 2019 from <https://patents.google.com/patent/US8472661>.
4. Casselman, W. (2001). *Snell's law—The law of refraction*. The University of British Columbia. Retrieved January 15, 2019 from <https://www.math.ubc.ca/~cass/courses/m309-01a/chu/Fundamentals/snell.htm>.
5. Darnton, N. C., Turner, L., Rojevsky, S., & Berg, H. C. (2007). On torque and tumbling in swimming *Escherichia coli*. *Journal of Bacteriology*, 189, 1756–1764.
6. Edberg, S. C., Rice, E. W., Karlin, R. J., & Allen, M. J. (2000). *Escherichia coli*: The best biological drinking water indicator for public health protection. *Symposium Series Society for Applied Microbiology*, 2, 106S–116S.
7. Fung, J., Perry, R. W., Dimiduk, T. G., & Manoharan, V. N. (2012). Imaging multiple colloidal particles by fitting electromagnetic scattering solutions to digital holograms. *Journal of Quantitative Spectroscopy & Radiative Transfer*, 113(18), 2482–2489. <https://doi.org/10.1016/j.jqsrt.2012.06.007>.
8. Garcia-Sucerquia, J., Xu, W., Jericho, S. K., Klages, P., Jericho, M. H., & Kreuzer, H. J. (2006). Digital in-line holographic microscopy. *Applied Optics*, 45(5), 836–850.
9. Gomez, A. M. L., Santana, P. C., & Mourão, A. P. (2020). Dosimetry study in head and neck of anthropomorphic phantoms in computed tomography scans. *SciMedicine Journal*, 2, 38–43.
10. Heo, J., & Hua, S. Z. (2009). An overview of recent strategies in pathogen sensing. *Sensors*, 9(6), 4483–4502.
11. Isikman, S. O., Greenbaum, A., Luo, W., Coskun, A. F., & Ozcan, A. (2012). Giga-pixel lens free holographic microscopy and tomography using color image sensors. *PLoS ONE*, 7, e45044.
12. Kesteloot, K., Azizan, A., Whitman, R., & Nevers, M. (2012). New recreational water testing alternatives. *Park Science*, 29(2), 6–12.
13. Laczka, O., Skillman, L., Ditcham, W. G., Hamdorf, B., Wong, D. K. Y., Bergquist, P., et al. (2013). Application of an ELISA-type screen printed electrode-based potentiometric assay to the detection of *Cryptosporidium parvum* oocysts. *Journal of Microbiological Methods*, 95, 182–185.
14. Lvov, N., Khabarov, S., Todorov, A., & Barabanov, A. (2018). Versions of fiber-optic sensors for monitoring the technical condition of aircraft structures. *Civil Engineering Journal*, 4, 2895–2902.
15. Mudanyali, O., Oztoprak, C., Tseng, D., Erlinger, A., & Ozcan, A. (2010). Detection of waterborne parasites using field-portable and cost-effective lensfree microscopy. *Lab on a Chip*, 10(18), 2419–2423. <https://doi.org/10.1039/c004829a>.
16. Olstadt, J., Schauer, J. J., Standridge, J., & Kluender, S. (2007). A comparison of ten USEPA approved total coliform/*E. coli* tests. *Journal of Water and Health*, 5(2), 267–282.
17. Parsa, N., Khajouei, G., Masigol, M., Hasheminejad, H., & Moheb, A. (2018). Application of electro-dialysis process for reduction of electrical conductivity and COD of water contaminated by composting leachate. *Civil Engineering Journal*, 4, 1034–1045.
18. Richard, C. (2013). *Research team develops new method to detect E. coli in water*. University of Alberta. Retrieved January 15, 2019 from <https://phys.org/news/2013-09-team-method-coli.html>.

19. Schnars, U., & Jüptner, W. (1994). Direct recording of holograms by a CCD target and numerical reconstruction. *Applied Optics*, *33*, 179–181.
20. Siva, N., & Kumar Gunda, S. N. (2013). Microspot with integrated wells (MSIW) for the detection of *E. coli*. In *ASME 2013 11th international conference on nanochannels, microchannels and minichannels, ICNMM 2013*.
21. Su, T.-W., Xue, L., & Ozcan, A. (2012). High-throughput lens free 3D tracking of human sperms reveals rare statistics of helical trajectories. *PNAS*, *109*, 16018–16022.
22. United States Environmental Protection Agency. (USEPA). (2002). *Method 1603: Escherichia coli (E. coli) in water by membrane filtration using modified membrane-thermotolerant Escherichia coli agar (modified mTEC)*. Retrieved January 15, 2019 from https://www.epa.gov/sites/production/files/2015-08/documents/method_1603_2009.pdf.
23. United States Environmental Protection Agency. (USEPA). (2012). *Monitoring and assessing water quality—volunteer water quality*. Retrieved January 15, 2019 from <https://archive.epa.gov/water/archive/web/html/index-18.html>.
24. Wang, Y., Ye, Z., & Ying, Y. (2012). New trends in impedimetric biosensors for the detection of foodborne pathogenic bacteria. *Sensors*, *12*(3), 3449–3471.
25. Wildeboer, D., Amirat, L., Price, R. G., & Abuknesha, R. A. (2010). Rapid detection of *Escherichia coli* in water using a hand-held fluorescence detector. *Water Research*, *44*, 2621–2628.
26. World Health Statistics (WHO). (2018). *Monitoring health for the SDS sustainable development goals*. Retrieved January 15, 2019 from <http://apps.who.int/iris/bitstream/handle/10665/272596/9789241565585-eng.pdf>.

Publisher's Note Springer Nature remains neutral with regard to jurisdictional claims in published maps and institutional affiliations.

APPENDIX C

PUBLISHED MANUSCRIPT ON HAND-HELD HOLOGRAPHIC SENSOR:

**OPTICALLY BASED HANDHELD SENSOR FOR VISUALIZATION AND
QUANTIFICATION OF CRYPTOSPORIDIUM PARVUM**



Optically Based Hand-Held Sensor for Visualization and Quantification of *Cryptosporidium Parvum*

Andrew Thompson¹ · Basil Hable¹ · Kyana Young² · Thomas Hansen^{1,3} · J. R. Strickler^{1,4} · Marcia R. Silva¹

Received: 21 April 2020 / Revised: 3 August 2020 / Accepted: 14 September 2020 /
Published online: 29 September 2020
© Springer Science+Business Media, LLC, part of Springer Nature 2020

Abstract

The ingestion of the protozoan parasite *Cryptosporidium*, resulting in the associated disease cryptosporidiosis, can cause major problems if introduced into a water supply for both animals and humans. This research focuses on the creation of a sensor to track and quantify the parasite with a digital camera system using Digital Inline Holographic Microscopy (DIHM) and software reconstruction. Since *Cryptosporidium* oocysts are not single celled and can be around 4–8 μm in diameter, they are easily detected with the DIHM at various depths within a 3.5 mL cuvette. As the sensor is improved by modifications, it could pick up behavior of movement and sizes of particles measured to positively identify the particle(s) being tracked as *Cryptosporidium* as others have achieved on *Escherichia coli* and other microorganisms. A significant advantage of this technique is the resulting sensor costs significantly less than traditional microscopes used in laboratory tests for detecting *Cryptosporidium*, or other methods like USEPA Method 1623 and can provide results within minutes. The sensor is a stellar alternative to current methods in detecting and quantifying *Cryptosporidium*.

Keywords Cryptosporidium · Sensor · DIHM · Water

✉ Marcia R. Silva
msilva@uwm.edu

¹ Water Technology Accelerator (WaTA), University of Wisconsin-Milwaukee, Milwaukee, WI, USA

² Department of Engineering, Wake Forest University, Winston-Salem, NC, USA

³ School of Freshwater Sciences, University of Wisconsin-Milwaukee, Milwaukee, WI, USA

⁴ Department of Biological Sciences, University of Wisconsin-Milwaukee, Milwaukee, WI, USA

1 Introduction

Cryptosporidium is a genus of parasites [26], first described by Tyzzer in 1907 [38], that negatively affects the health of humans [13] and animals [28, 30] who ingest the parasite through the fecal–oral route [18]. *Cryptosporidium* causes cryptosporidiosis which is a severe gastrointestinal illness [15] which can be fatal to newborns [14], the elderly [25], and the immunocompromised [1], like those with human immunodeficiency virus / acquired immunodeficiency syndrome (HIV/AIDS) [29]. In fact, the first human case was reported in 1976 in an immunocompetent child [27].

Detection and prevention of *Cryptosporidium* breakthrough in water systems is important to prevent associated illnesses. Inadequate drinking water treatment techniques have caused many cases of infection, diarrheal disease, and sometimes death from the parasite in the United States [6, 10] and around the world [1, 11, 31, 35]. The largest outbreak in history occurring in Milwaukee County, Wisconsin of the United States where there were at least 400,000 cases of cryptosporidiosis in 1993 [21]. That was and still would be a significant portion of Milwaukee County's population of about 950,000 people in 1993 [23] and 948,201 people in 2018 [3].

An early detection would be able to give a detailed view of how a contaminated water source or water system may be within a municipality. Following the Long Term 2 Enhanced Surface Water Treatment Rule (LT2ESWTR), water systems of less than 10,000 people in the United States of America are only required to test for *Cryptosporidium* (for an initial two year period) if 10 *Escherichia coli* (*E. coli*) / 100 mL (lakes or reservoir source) or 50 *E. coli* / 100 mL (flowing stream source) are detected [8]. For water suppliers of at least 10,000 people, during this 2 year period, *Cryptosporidium* must be tested at least monthly [8]. This monitoring is used to ensure drinking water treatment systems are working properly. Because the tests are done at least monthly, *Cryptosporidium* presence in water occurs post-consumption. The monthly testing is likely due to the cost of current systems; the cost limits proper warning of *Cryptosporidium* presence [2].

The World Health Organization (WHO) recommends monitoring turbidity targets as an indirect method to increase the removal of *Cryptosporidium*, without using a direct detection method to determine the presence of *Cryptosporidium* in water. [39]. Another method, surface-enhanced resonance Raman spectroscopy, can detect *Cryptosporidium* in non-real time [33]. Other methods can detect various concentrations of *Cryptosporidium* in real time as the sensor does. These other methods include polymerase chain reaction (PCR) measurement [12], surface plasmon resonance-based inhibition assays [16], and quartz crystal microbalance with dissipation monitoring (QCM-D) [32]. Both the proposed sensor and the listed methods give the ability to continuously monitor water for *Cryptosporidium* in real time. However, there are difficulties and scenarios in which the proposed sensor would be a better option.

As for PCR, there is a risk of contamination of short amplified DNA fragments, laboratory areas must be sterilized, sometimes requires a single tube, or multiple

tubes to be used then discarded [9, 24]. This generates waste that the proposed sensor does not generate as the proposed sensor can reuse a single cuvette or use a flow-through cuvette (as if attached to a water pipe). In addition, PCR requires support equipment such as centrifuges [9, 24] while the proposed sensor does not require more than the device itself and a laptop. This saves money and simplifies the process.

As for surface plasmon resonance methods, the industrial process to create this type sensor is more complex. The production involves self-assembling monolayers [16, 17] which itself requires multiple processes to produce [19]. While the proposed sensor requires a complementary metal-oxide sensor (CMOS), they are also used for photography [22, 36], so it is more widely available as an “off-the-shelf” product. This keeps costs lower for the proposed sensor.

As for QCM-D, researchers were able to use this method to find concentrations of 3×10^5 – 1×10^7 oocysts/mL [32], while our proposed sensor looks from 3×10^{-1} to 3×10^2 oocysts/mL. The proposed sensor has a different use range and may be more precise.

As for other non-real time methods, the proposed sensor mediates high costs by performing the quantification of *Cryptosporidium* via software in real time, rather than through relatively lengthy laboratory processes, like USEPA Method 1623 [7]. Images of the water sample are taken using a laser and a typical CMOS camera. The software then analyzes particles detected by the sensor 15 times per second.

While the Digital Inline Holographic Microscopy (DIHM) process is not new, the sensor is novel because it combines the DIHM method with novel software made to detect *Cryptosporidium*. In addition, the sensor fills a niche that the other types of sensors listed earlier have not. As stated earlier, the sensor requires less setup than PCR (PCR requires centrifuges, for example), is easier to assemble than surface plasmon resonance methods, has a different use range than QCM-D, and is in real-time, unlike Raman spectroscopy and laboratory methods like EPA Method 1623.

2 Material and Methods

2.1 Components and Setup

The sensor consists of three main components: a 650 nm laser (GeeBat Mini Laser Dot Diode Module Head Red, wavelength 650 nm, 5 V, 5mW Diode Lasers with internal lens removed) to illuminate particles in a cuvette (Azzotta Part N₀. G104—pathlength 10 mm, volume 3.5 mL, optical glass—340–2500 nm) which holds the sample being examined, and a CMOS (See3CAM_CU51—5MP Custom Lens Monochrome USB3 Camera by e-con Systems, housing an e-CAM50_CU9P031_MOD—5.0 MP MT9P031 Monochrome camera module) to image the patterns of light wave constructive and destructive interference. Two additional cables were used: one USB 3.0 type-A to USB 3.0 type-Micro B and one USB type-A to USB type-Micro B. A laptop was used to process the data (Lenovo Yoga 720-12IKB I3 4G 128G 10H, Model Name: 81B5).

2.2 Design Considerations

2.2.1 Design Overview

Figure 1 shows a three-dimensionally modeled version of the core DIHM process.

The laser is powered from a custom circuit described in Sect. 2.2.4 Hardware and Circuitry. The CMOS is connected to the laptop via USB 3.0 type-A to USB 3.0 type-Micro B cable for data transfer. The data collected is then processed through a program written in JavaScript that creates the hologram in the DIHM process and returns a comma separated variable file which is processed in Microsoft Excel for *Cryptosporidium* counts.

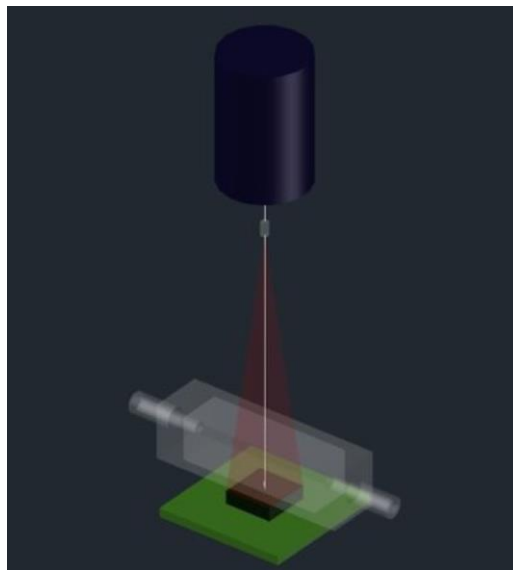
2.2.2 Calculating the Sample Volume (SV)

SV is the portion of the sample within the cuvette in which particles can be observed by the sensor.

Within the laser, the collimator lens is removed. The lens focuses the light. Without it, a conical section of a spherical wave of coherent light is produced. Figure 2 shows the conical section as a solid line, and the light destined to hit the CMOS sensor as a dotted line. This is what produces the SV's shape. (Fig. 3).

Calculation of the SV means considering indices of refraction for the materials that are between the laser and the CMOS: air, cuvette glass, and water. Different refractive indices changing light as it goes through two materials requires the use of Snell's Law [5]. An altered version of W. Casselman's schematic diagram in Fig. 4, allows a simplification of the equations.

Fig. 1 The setup's laser (top), cuvette, and CMOS (bottom) work together



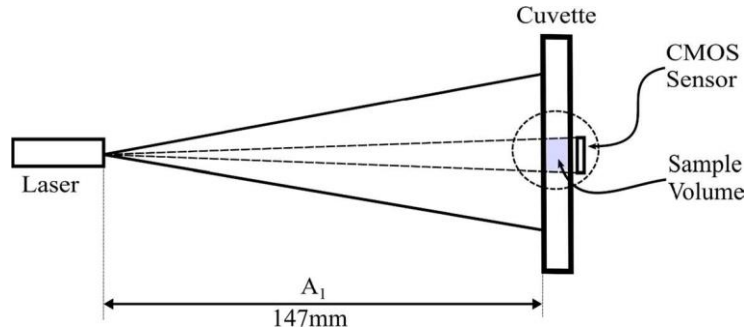


Fig. 2 The Sample Volume is not a simple cubic area, but a truncated right pyramid (a square frustum). The face closest to the laser is smaller than the face further from the laser

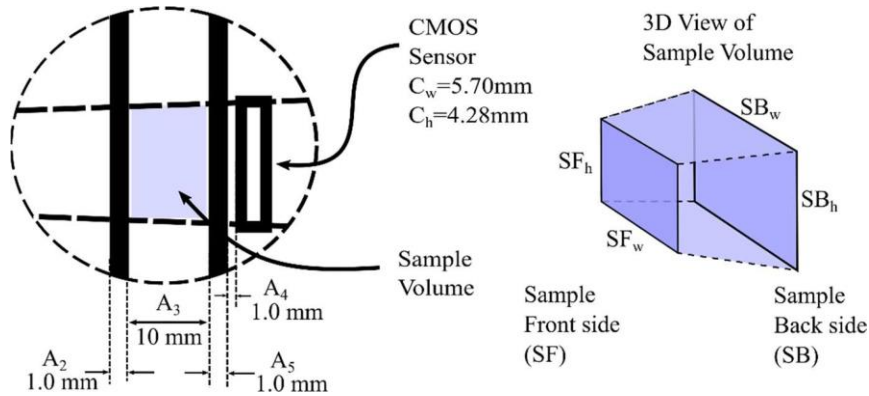
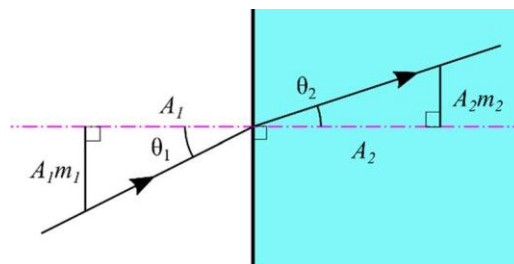


Fig. 3 A closer view of the SV with relevant dimensions provided to calculate the SV

Fig. 4 Altered diagram of W. Casselman's



By definition, $m_1 = \tan \theta_1$, and $m_2 = \tan \theta_2$ and a common simplification that for very small angles θ , $\sin \theta \approx \tan \theta \approx \theta$ is used, thus from Snell's law (Eq. 1):

$$n_1 \sin \theta_1 = n_2 \sin \theta_2 \tag{1}$$

Substitute $m_1 \approx \sin \theta_1$ and $m_2 \approx \sin \theta_2$ to obtain Eq. 2:

$$n_1 m_1 \approx n_2 m_2 \quad (2)$$

where m_1 and m_2 are the slopes of the lines of light with respect to the normal to the surface.

The dimensions (distances, thicknesses) of Figs. 2 and 3:

$$A_1 = \text{Distance from laser to cuvette (147mm)}$$

$$A_2 = \text{Thickness of cuvette glass facing the laser (1mm)}$$

$$A_3 = \text{Inside width of cuvette (10mm)}$$

$$A_4 = \text{Thickness of cuvette glass on sensor side (1mm)}$$

$$A_5 = \text{Distance between cuvette glass and CMOS (1mm)}$$

$$C = \text{Width or height of CMOS (5.70mm and 4.28mm)}$$

The three indices of refraction are as follows:

$$n_0 = n \text{ for air } (\approx 1.00)$$

$$n_1 = n \text{ for water } (\approx 1.3325)$$

$$n_2 = n \text{ for cuvette glass } (\approx 1.5230)$$

Since $m_0 n_0 = m_1 n_1 = m_2 n_2$, that $m_1 = m_0 \left(\frac{n_0}{n_1} \right)$ and $m_2 = m_0 \left(\frac{n_0}{n_2} \right)$. Thus Eq. 3:

$$C = A_1 m_0 + A_2 m_0 \left(\frac{n_0}{n_2} \right) + A_3 m_0 \left(\frac{n_0}{n_1} \right) + A_4 m_0 \left(\frac{n_0}{n_2} \right) + A_5 m_0 \quad (3)$$

And obtain Eq. 4 by rearranging Eq. 3:

$$\frac{C}{m_0} = A_1 + A_2 \left(\frac{n_0}{n_2} \right) + A_3 \left(\frac{n_0}{n_1} \right) + A_4 \left(\frac{n_0}{n_2} \right) + A_5 \quad (4)$$

Isolating m_0 , obtains Eq. 5:

$$m_0 = \frac{C}{A_1 + A_2 \left(\frac{n_0}{n_2} \right) + A_3 \left(\frac{n_0}{n_1} \right) + A_4 \left(\frac{n_0}{n_2} \right) + A_5} \quad (5)$$

For the larger CMOS width of $C = 5.70\text{mm}$:

$$m_0 = \frac{(5.70\text{mm})}{(147\text{mm}) + (1.0\text{mm}) \left(\frac{(1.00)}{(1.5230)} \right) + (10\text{mm}) \left(\frac{(1.00)}{(1.3325)} \right) + (1.0\text{mm}) \left(\frac{(1.00)}{(1.5230)} \right) + (1.0\text{mm})}$$

$$m_0 = 0.03635$$

Using Eqs. 6 and 7, the width of the side closest to the laser (SF_w) and the back side (SB_w) of the SV is calculated:

$$SF_w = A_1 m_0 + A_2 m_0 \left(\frac{n_0}{n_2} \right) \quad (6)$$

$$SF_w \approx 5.367 \text{ mm}$$

$$SB_w = A_1 m_0 + A_2 m_0 \left(\frac{n_0}{n_2} \right) + A_3 m_0 \left(\frac{n_0}{n_1} \right) \quad (7)$$

$$SB_w \approx 5.640 \text{ mm}$$

The same calculations for the heights result with $SF_h = 4.030 \text{ mm}$ and $SB_h = 4.234 \text{ mm}$ (later the height's $m_0 = 0.02729$ will be needed).

Lastly, the volume of a truncated right pyramid is used:

$$v = \frac{1}{3} h (a_1 + a_2 + \sqrt{a_1 a_2}) \quad (8)$$

Substitute $h = A_3 = 10 \text{ mm}$, $a_1 = SF_w SF_h$, $a_2 = SB_w SB_h$, to obtain an SV of

$$SV = 227.451 \text{ mm}^3 = 227.451 \mu_1$$

2.2.3 Calculation of Numerical Aperture (NA) and Resolution

The resolving power of the microscope, the NA, is a valuable description of the microscope's resolution. The calculation of NA is as follows: [34]

$$NA = \frac{\left(\frac{W}{2} \right)}{\sqrt{\left(\frac{W}{2} \right)^2 + D^2}} \quad (9)$$

W is the width of the CMOS (4.28 mm), and D is the distance from the laser to the plane of the CMOS. That distance is altered by the refractive indices of the materials the light passes through. Thankfully, the results of previous calculations can be used to get D. The light begins and ends in air (A_1 and A_5 in Figs. 2 and 3). This means, the slopes of light are known and can be used to find the distance to the laser from the CMOS is $\frac{C_w}{m_0} = \frac{5.70 \text{ mm}}{0.03635} \approx 156.81 \text{ mm}$. This is the value for D in Eq. 9. The NA was calculated using the narrower of the dimensions, where $W = 4.28 \text{ mm}$ and $D = 156.81 \text{ mm}$, resulting in $NA = 0.01364592$ from Eq. 9.

The smallest distance that two particles can be distinctly, laterally separated is the lateral resolution. This is shown in Eq. 10:[38]

$$|\mathbf{r}_2 - \mathbf{r}_1| = \frac{\lambda}{2NA} \quad (10)$$

The point-sources \mathbf{r}_1 and \mathbf{r}_2 are a part of the same plane and the wavelength of the coherent light source (laser) is λ .

The equation for depth resolution is below:

$$|\mathbf{r}_2 - \mathbf{r}_1| = \frac{\lambda}{(2NA)^2} \quad (11)$$

This time, \mathbf{r}_1 and \mathbf{r}_2 , the point-sources, are in a line perpendicular to the plane of the sensor and λ is still the wavelength of coherent light from the laser (650 nm).

Because the NA is strictly much less than 1, the depth resolution is always larger than the lateral resolution.

The lateral resolution is 23.82 μm . Similarly, the depth resolution obtained is 1745.33 μm .

2.2.4 Hardware and Circuitry

A three-part, custom-made circuit is used to power the laser used in the DIHM process. This circuit consists of a modified USB-A to Micro-USB cable, a 170- Ω resistor, and the laser diode. The cable's USB-A end is connected to the laptop and the Micro-USB end is clipped to use the +5 V wire to power the circuit. The +5 V wire connects to the 170- Ω resistor which connects to the laser. The other wire of the laser connects to the ground of the clipped USB cable. Figure 5 displays this below.

2.2.5 Power Consumption Rate

The sensor's laser and CMOS are powered by the laptop. The laser diodes 5mW is negligible, and the CMOS needs 0.84–1.50 W for acquiring data.

2.2.6 Software Design and Organization

Upon using the sensor to acquire images (2592 by 1944 pixels at 15 frames per second), the images must be processed. Figure 6 shows a raw image acquired by a CMOS sensor for a sample with no *Cryptosporidium* and Fig. 7 shows an image of

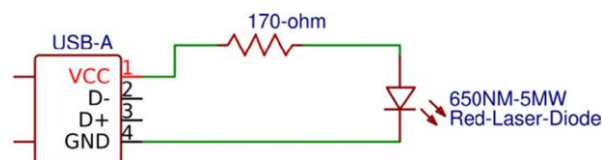


Fig. 5 The custom-made circuit used to power the laser for DIHM

Fig. 6 The ‘raw image’ acquired by the CMOS before any editing (cropped to 1024 by 1024 pixels). This image is one from sample C. Sample C has zero *Cryptosporidium*

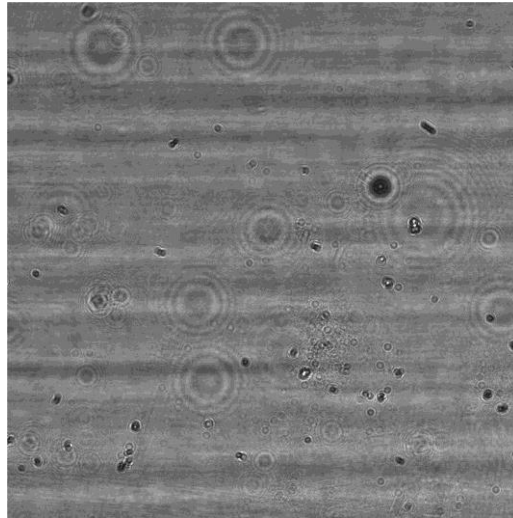
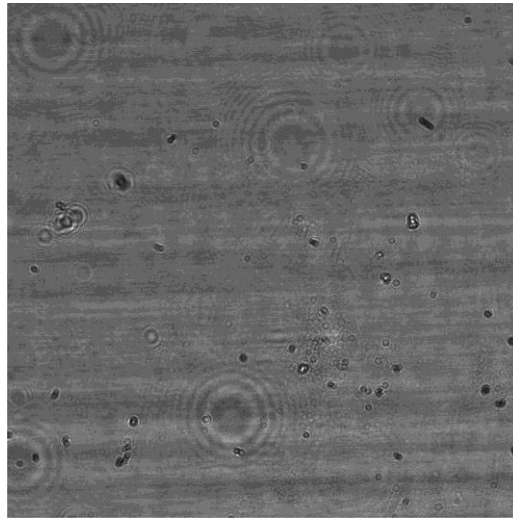


Fig. 7 A raw image cropped to 1024 by 1024 of one image of sample B. Sample B has 1,000 *Cryptosporidium*. It is difficult to see a difference between this and Fig. 6 without computer help



a sample with 1000 *Cryptosporidium* without any editing. It is difficult to see the difference between the two images without computer help. That is why a series of image processing steps and image reconstruction is needed.

The first step is to filter the images by removing non-moving content, like dust on the CMOS or bacteria on the cuvette. This is done by continuously subtracting one image from the previous image the sample to tell what has moved in the DI water.

The resulting image is ready to be processed as a hologram following the DIHM process. Put simply, the ripple-like patterns in the images are “shadows”

of light waves constructively and destructively interfering. The closer the object casting the “shadow” is to the light source, the larger the “shadow” will be. The further it is, the smaller the shadow. Using the mathematical relationship behind that process, the distance of a particle from the light source can be found by artificially reconstruct what the light would look like at a distance between the CMOS and the light source incrementally.

At each increment, a software process called “blob detection” is ran to highlight them easier for a program to count.

The depth information, as exemplified in Fig. 8, plus the X and Y coordinates from the depth reconstructions, gives the X, Y, and Z coordinates for each particle’s three-dimensional position and its size. This information is written to a comma separated variable file (.csv) and imported into Microsoft Excel to be tabulated and graphed. The.csv file for this set of trials covered 14,024 particles in 18 samples. Following a similar method, our research team has been able to demonstrate the use of this optically based sensor platform for detection and quantification of bacteria *E. coli* spiked in DI water [37].

2.3 *Cryptosporidium* Preparation and Quantification Using the Standard Method

The Iowa isolate of *Cryptosporidium* oocysts were propagated in the Holstein calf. The oocysts, after purification using cesium chloride and sucrose, stored in antibiotic solution before delivery to the Wisconsin State Laboratory of Hygiene (WSLH). The Wisconsin State Laboratory of Hygiene provided the flow cytometer-sorted live sample oocysts. *Cryptosporidium* oocysts were stored in 3 mL of phosphate buffered saline (PBS) (1X) in preparation for analysis. Triplicates of live sample of the oocysts (10, 100, 1000, and 10,000) were used as the positive control for the detection methods; a negative control consisted of triplicate 3 mL samples of PBS. Samples were transferred to a cuvette placed in the sensor holder for analysis.

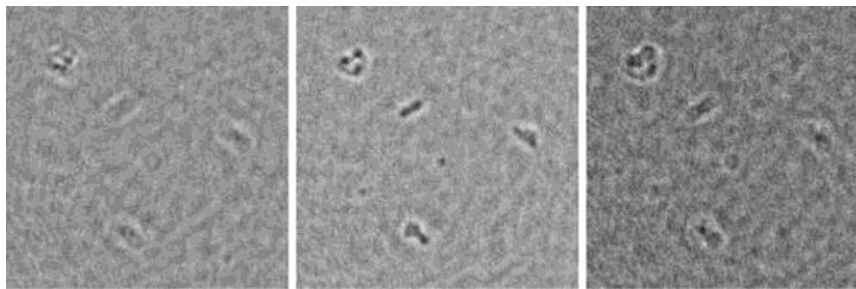


Fig. 8 An example of a series of depths at 3.3 mm, 3.5 mm, and 3.7 mm (left to right) for a sample of *Escherichia coli* in deionized (DI) water

2.4 *Cryptosporidium* Quantification Using the Novel Optical Sensor

Cryptosporidium oocysts were measured using the sensor by putting 3 mL of the sample into the sensor's cuvette, then running an "ffmpeg" bash script to capture 10s of data from the CMOS. The cuvette was emptied and rinsed with 3 mL of HNO₃ and 3 mL of DI water before use was repeated for the next sample. After the data was gathered, the software process outlined in 2.2.6 was ran.

3 Results

3.1 Calibration and Performance of the Novel Optical Sensor

Each of the six samples, A through F, were measured three times. "Count" is the cumulative number of pixels of particles in each sample. "Particle Value" is the brightness of the pixels counted in "Count". "Crypto" is the actual amount of *Cryptosporidium* oocysts put into the sample to be measured. The volume measured by the sensor was 227.451 μ l or 0.227451 mL as stated in Sect. 2.2.2. The *Cryptosporidium* was in 3 mL of DI water. Results are displayed in Table 1.

A graph of the comparison between the sensor and actual amount of *Cryptosporidium* / mL is shown in Fig. 9. Note for the logarithmic regression, the value of 0 Crypto / mL was replaced with 0.03333333 to avoid log (0) (negative infinity).

The R^2 value of 0.9827 indicates a high correlation between the sensor's Count / mL and the actual amount of *Cryptosporidium* in the water samples. Standard

Table 1 Particle counts using the novel sensor's process

Source	Count/mL	Particle value / mL	Crypto / mL
A1	44,736.835	44,381.28677	3.33333333
A2	11,225.955	12,207.14716	3.33333333
A3	44,794.048	50,468.69097	3.33333333
B1	27,578.908	23,931.61726	333.333333
B2	37,645.851	25,514.85162	333.333333
B3	56,383.101	59,030.88099	333.333333
C1	13,143.589	16,323.57625	0
C2	33,013.434	26,901.99451	0
C3	37,975.402	31,228.02628	0
D1	74,453.938	90,055.06904	33.3333333
D2	21,892.923	20,237.97587	33.3333333
D3	19,809.555	24,330.43063	33.3333333
E1	30,597.196	22,533.42751	0.33333333
E2	36,467.942	21,422.90186	0.33333333
E3	26,102.541	16,194.10506	0.33333333
F1	56,765.791	48,464.83069	0
F2	21,917.469	18,669.69828	0
F3	1586.3086	763.7644728	0

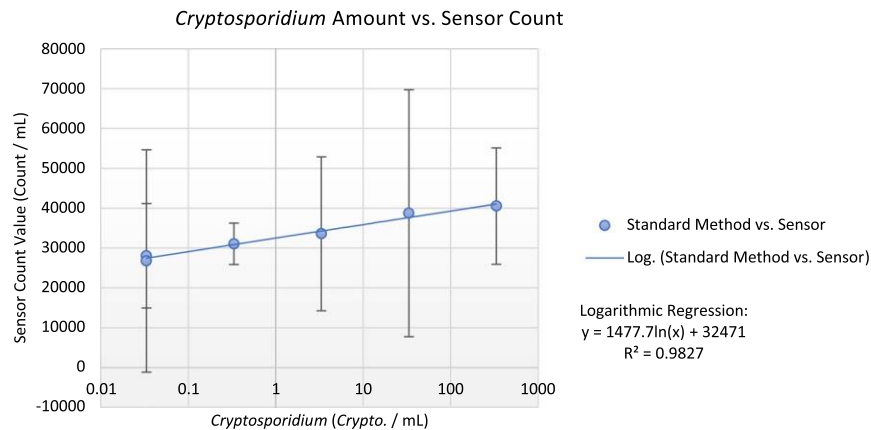


Fig. 9 Correlation between the actual amount of *Cryptosporidium* versus the sensor's count with standard deviation bars

deviation is expected to reduce as the sensor is trained with larger dataset. Comparatively, the use of QCM-D demonstrated a correlation of $R^2 = 0.99$ for spiked values of 3.0×10^5 oocysts/mL [34]. However, any concentration lower than the 3.0×10^5 oocysts/mL or higher than 10^7 oocysts/mL was not distinguishable using the protocol. The piezoelectric-excited millimeter-sized cantilever biosensor [4], using the resonance frequency change to oocysts glass surface antibody binding relationship, demonstrated a correlation coefficient detection of 0.98 when 100 to 10,000 oocysts/mL flowed (1 mL/min) over the glass surface for an 80-min duration; this method requires the use of additional chemicals for antibody immobilization. Moreover, the use of a label-free interdigitated-based capacitive biosensor, also making use immobilized antibodies, demonstrated an $R^2 = 0.9118$ when correlating the relationship between relative capacitance and the concentration of oocysts [20].

4 Conclusions

The sensor has been shown to be able to detect *Cryptosporidium* and do so in less than 20 min for an equipment cost of about \$300 (a \$179 CMOS, \$90 3D printed case, \$5 USB-A to Micro-USB, less than \$20 cuvette, and laser & resistor under \$1 each with price reductions in bulk). The sensor brings closer the ability to watch for *Cryptosporidium* in DI water in real time in a lab, public water system, or an individual's household.

Moving forward, specific families of pathogens will be tracked to teach the sensor to differentiate between various species of organisms. Training a convolutional neural net to do particle recognition could achieve this. As it stands, measuring in (at least) triplicate with this system improves consistency in measurement.

Acknowledgements Our research was funded in part by the Undergraduate Research Fellows (SURF) program at the University of Wisconsin – Milwaukee (UWM). Thanks to the Wisconsin State Laboratory of Hygiene for the live sample oocysts sorting. Thanks to Dr. Brooke Mayer for the use of her lab while handling *Cryptosporidium*.

References

1. Abubakar, I., Aliyu, S. H., Arumugam, C., Usman, N. K., & Hunter, P. R. (2007). Treatment of cryptosporidiosis in immunocompromised individuals: Systematic review and meta-analysis. *British Journal of Clinical Pharmacology*, *63*(4), 387–393.
2. Bryan, B. A., & Kandulu, J. M. (2009). Cost-effective alternatives for mitigating *Cryptosporidium* risk in drinking water and enhancing ecosystem services. *Water Resources Research*. <https://doi.org/10.1029/2008WR007606>.
3. Bureau, USC. (2020). QuickFacts–Milwaukee County, Wisconsin; Milwaukee city, Wisconsin. <https://www.census.gov/quickfacts/fact/table/milwaukeecountywisconsin,milwaukeecitywisconsin/PST045219>. Accessed January 3, 2020
4. Campbell, G. A., & Mutharasan, R. (2008). Near real-time detection of *Cryptosporidium parvum* oocyst by IgM-functionalized piezoelectric-excited millimeter-sized cantilever biosensor. *Biosensors and Bioelectronics*, *23*(7), 1039–1045.
5. Casselman, W. (2001). The law of refraction. <https://www.math.ubc.ca/~cass/courses/m309-01a/chu/Fundamentals/snell.htm>.
6. D'Antonio, R. G., et al. (1985). A waterborne outbreak of cryptosporidiosis in normal hosts. *Annals of Internal Medicine*, *103*, 886–888.
7. EPA (2005) Method 1623: *Cryptosporidium* and *Giardia* in Water by Filtration/IMS/FA
8. EPA (2016) Long term 2 enhanced surface water treatment rule documents.
9. Fontaine, M., & Guillot, E. (2003). An immunomagnetic separation-real-time PCR method for quantification of *Cryptosporidium parvum* in water samples. *Journal of Microbiological Methods*, *54*, 29–36.
10. Gharpure, R., Perez, A., Miller, A. D., Wikswo, M. E., Silver, R., & Hlavsa, M. C. (2019). Cryptosporidiosis Outbreaks—United States, 2009–2017. *Morbidity and Mortality Weekly Report*, *68*, 568–572.
11. Glaberman, S., et al. (2002). Three drinking-water-associated cryptosporidiosis outbreaks, Northern Ireland. *Emerging Infectious Diseases*, *8*, 631–633.
12. Guy, R. A., Payment, P., Krull, U. J., & Horgen, P. A. (2003). Real-time PCR for quantification of *Giardia* and *Cryptosporidium* in environmental water samples and sewage Applied. *Environmental Microbiology*, *69*, 5178–5185.
13. Hamoudi, A. C., Qualman, S. J., Marcon, M. J., Hribar, M., McClung, H. J., Murray, R. D., et al. (1988). Do regional variations in prevalence of cryptosporidiosis occur? The central Ohio experience. *American journal of public health*, *78*, 273–275.
14. Huang, D. B., Chappell, C., & Okhuysen, P. C. (2004). Cryptosporidiosis in children. *Seminars in Pediatric Infectious Diseases*, *15*, 253–259.
15. Jokipii, L., Pojola, S., & Jokipii, A. M. M. (1983). *Cryptosporidium*: a frequent finding in patients with gastrointestinal symptoms. *The Lancet*, *322*, 358–361.
16. Kang, C. D., Cao, C., Lee, J., Choi, I. S., Kim, B. W., & Sim, S. J. (2008). Surface plasmon resonance-based inhibition assay for real-time detection of *Cryptosporidium parvum* oocyst. *Water Research*, *42*, 1693–1699.
17. Kang, C. D., Lee, S. W., Park, T. H., & Sim, S. J. (2006). Performance enhancement of real-time detection of protozoan parasite, *Cryptosporidium* oocyst by a modified surface plasmon resonance (SPR) biosensor. *Enzyme and Microbial Technology*, *39*, 387–390.
18. Keusch, G. T., Hamer, D., Joe, A., Kelley, M., Griffiths, J., & Ward, H. (1995). Cryptosporidia—who is at risk? *Schweizerische Medizinische Wochenschrift*, *125*, 899.
19. Love, J. C., Estroff, L. A., Kriebel, J. K., Nuzzo, R. G., & Whitesides, G. M. (2005). Self-assembled monolayers of thiolates on metals as a form of nanotechnology. *Chemical reviews*, *105*, 1103–1170.
20. Luka, G., Samiei, E., Dehghani, S., Johnson, T., Najjaran, H., & Hoorfar, M. (2019). Label-Free capacitive biosensor for detection of *Cryptosporidium*. *Sensors*, *19*, 258.

21. MacKenzie, W. R., et al. (1994). A massive outbreak in Milwaukee of *Cryptosporidium* infection transmitted through the public water supply. *The New England Journal of Medicine*, 331, 161–167.
22. Mehta, S., Patel, A., Mehta, J. (2015). CCD or CMOS Image sensor for photography. In: *2015 International conference on communications and signal processing (ICCSP)*, 2015. (pp 291–294)
23. Milwaukee County, Wisconsin Population (2020). <https://worldpopulationreview.com/us-counties/wi/milwaukee-county-population>. Accessed January 3, 2020
24. Minarovičová, J., Kaclíková, E., Krascenicsová, K., Siekel, P., & Kuchta, T. (2009). A single-tube nested real-time polymerase chain reaction for sensitive contained detection of *Cryptosporidium parvum*. *Letters in Applied Microbiology*, 49, 568–572.
25. Mor, S. M., DeMaria, A., Jr., Griffiths, J. K., & Naumova, E. N. (2009). Cryptosporidiosis in the elderly population of the United States : an official publication of the Infectious Diseases Society of America. *Clinical Infectious Diseases*, 48, 698–705.
26. Morgan, U. M., Xiao, L., Fayer, R., Lal, A. L., & Thompson, R. C. A. (1999). Variation in *Cryptosporidium*: towards a taxonomic revision of the genus. *International Journal of Parasitology*, 29, 1733–1751.
27. Nime, F., Burek, J., Page, D., Holscher, M., & Yardley, J. (1976). Acute enterocolitis in a human being infected with the protozoan *Cryptosporidium*. *Gastroenterology*, 70, 592–598.
28. NRC (1991) Infectious diseases of mice and rats. National Academies Press (US), Washington, (DC)
29. O’connor, R. M., Shaffie, R., Kang, G., & Ward, H. D., (2011). Cryptosporidiosis in patients with HIV/AIDS. *AIDS*, 25, 549–560.
30. O’Donoghue, P. (1995). *Cryptosporidium* and cryptosporidiosis in man and animals. *International Journal for Parasitology*, 25, 139–195.
31. Pape, J., Levine, E., Beaulieu, M., Marshall, F., Verdier, R., & Johnson, W. J. (1987). Cryptosporidiosis in Haitian children. *The American Journal of Tropical Medicine and Hygiene*, 36, 333–337.
32. Poitras, C., Fatisson, J., & Tufenkji, N. (2009). Real-time microgravimetric quantification of *Cryptosporidium parvum* in the presence of potential interferents. *Water Research*, 43, 2631–2638.
33. Rule, K. L., & Vikesland, P. J. (2009). Surface-enhanced resonance Raman spectroscopy for the rapid detection of *Cryptosporidium parvum* and *Giardia lamblia*. *Environmental Science and Technology*, 43, 1147–1152.
34. Schnars, U., & Jüptner, W. (1994). Direct recording of holograms by a CCD target and numerical reconstruction. *Applied Optics*, 33, 179–181.
35. Sethi, S., Sehgal, R., Malla, N., & Mahajan, R. (1999). Cryptosporidiosis in a tertiary care hospital. *The National Medical Journal of India*, 12, 207–209.
36. Theuwissen, A. J. P. (2001). CCD or CMOS image sensors for consumer digital still photography? In: 2001 international symposium on VLSI technology, systems, and applications. Proceedings of technical papers Hsinchu, Taiwan, Taiwan 2001. IEEE. doi:<https://doi.org/10.1109/VTSA.2001.934511>
37. Thompson, A., Honts, A., Strickler, J. R., Hansen, T., & Silva, M. R. (2020). Optically based bacteria hand held-sensor: from fundamentals to proof of concept. *Sensing and Imaging*, 21(1), 217–241.
38. Tyzzer, E. E. (1910). An extracellular Coccidium, *Cryptosporidium Muris* (Gen. Et Sp. Nov.), of the gastric Glands of the Common Mouse. *The Journal of Medical Research*, 23, 487–510-3.
39. WHO (2017) Water quality and health-Review of turbidity information for regulators and water suppliers.

Publisher’s Note Springer Nature remains neutral with regard to jurisdictional claims in published maps and institutional affiliations.

APPENDIX D

**PROVISIONAL PATENT APPLICATION:
FLOW SIMULATION AND VISUALIZATION
WITH REAL-TIME VIDEO INTERACTIVITY**

Provisional Application for United States Patent

TITLE: Flow Simulation and Visualization with Real-Time Video Interactivity

INVENTOR(S): Thomas F. Hansen

BACKGROUND

[0001] The study of the dynamics of fluid flow through and around solid objects is important in a wide range of fields, including oceanography and limnology, architecture, engineering, biology, and medicine. Computer models of such flows have been developed and are in common use. However, the operation of such models generally requires extensive training, and intimate knowledge of the relatively complex mathematics and physics upon which the models are based. They generally require extensive setup and configuration, and lack interactivity. Such complexity is required to ensure the accuracy of the model calculations, which is vital when used by scientists and engineers to design critical structures such as buildings, aircraft, and plumbing systems. At the same time it becomes very difficult for those who lack extensive mathematical and physics training to develop an intuitive understanding, or “feel,” for the concepts of fluid flow.

BRIEF SUMMARY OF THE INVENTION

[0002] The subject invention comprises a method and apparatus which provides an interactive display which demonstrates a flowing fluid interacting with physical objects. In its initial embodiment, an animated depiction of computer-simulated two-dimensional horizontal fluid flow – similar to flow through a pipe or wind tunnel – is projected onto a

wall. Shadows cast by people, animals, or other objects placed in the projection beam interactively disrupt the flow, and the animated flow changes in real-time to reflect the new path of flow, as the simulation is updated continuously to treat the shadows as solid objects placed in the flow field. This invention has wide potential application, from educational demonstrations in front of a classroom, to interactive exhibits in museums, and other public places such as airports. In this embodiment, someone simply can put their hand in the projection field, cast a shadow, and immediately see the simulated fluid flow around the shadow of their hand.

BRIEF DESCRIPTION OF THE DRAWINGS

[0003] Figure 1. Figure 1 shows a simple schematic diagram of the physical arrangement of the key elements: the projector, the screen, the object casting a shadow, and the camera, as well as depicting the connections to a computer.

[0004] Figure 2. Figure 2 shows a block diagram of the functional components, which is basically an exploded view of Figure 1.

[0005] Figure 3. Figure 3 shows graphically how each step of the process works. This is referred to in much more detail in the next section.

[0006] Figure 4. Figure 4 schematically shows another embodiment in which the shape and position of the object which defines the fluid flow obstacle is detected separately from the projection and/or display of the fluid simulation by use of a "green screen" or other similarly contrasting background.

[0007] Figure 5. Figure 5 depicts an extension of the embodiment depicted in Figure 4 by taking advantage of the fact that the "green screen" embodiment captures the full

image of the person and/or object which is defining the fluid obstacle. So, rather than simply recreating the shadow effect, the actual image of the person and/or object is superimposed on the flow field, giving the appearance of the actual person and/or object being immersed in the fluid flow simulation.

[0008] Figure 6. Figure 6 breaks down in further detail exactly how the software takes the input from the camera, uses it to update the fluid flow, and updates the display.

DETAILED DESCRIPTION AND BEST MODE OF IMPLEMENTATION

[0009] When the initial embodiment is first started up, the display will look similar to the depiction shown in Figure 3.1. The flow simulated is similar to a wind tunnel, or water flow through a pipe, with the flow moving horizontally from left to right. The flow is represented in two ways. First, the model computes the trajectory of imaginary particles as if they were suspended in the computed flow field, and displays them as each iteration of the model is completed. Optionally, as shown in Figure 3.1, 3.5, and 3.6, the particles can have “tails” which show the path the particle has taken. This helps emphasize the direction of the flow, and helps visualize the flow speed and direction when still images of the model display are taken, as of course shown in the figures.

[00010] When an object, or just a person’s hand, is placed between the projector and the screen, a shadow is cast, which obscures part of the projected image of the fluid flow. This is depicted in Figure 3.2. This shadow is detected by the camera, and a simple image filter called a “threshold” filter is used to isolate the shadow from the rest of the image. This is done by simply taking all image pixels brighter than a threshold value and making them white, and taking all image pixels below that threshold and

making them black. The simulated fluid flow is purposely designed to never actually display below a certain brightness level, thus the only places in the camera's view of the flow display that will appear very dark or black will be the shadows of objects. This allows the simple threshold filter to reliably isolate the shadows from the image.

[00011] Once the shadow has been isolated from the image by the threshold filter process, a piece of the software referred to in the Figures as the Boundary Condition Updater takes the shadow image and resamples (or pixelates) the shadow to correspond with the computational domains of the fluid flow model, resulting in a data set which is graphically depicted in Figure 3.4.

[00012] The fluid dynamics model, at the iteration following the establishment of the new solid boundary configuration, will immediately use the new solid boundaries to compute the fluid flow, taking the new boundaries into account. This results in a display similar to that shown in Figure 3.5. One detail that is important to note here, is that the resampled, pixelated version of the shadow is not displayed on the screen. This is not necessary in the initial embodiment, because the shadow being cast by the object is still present. Thus it is not only unnecessary and redundant in this arrangement to display the shadows, it also serves to minimize the effect of having finite computational domains, which for lower-powered computers must be several display pixels across. This results in small discrepancies between the shadow cast and the actual boundaries used by the model. In normal situations, these discrepancies are too small to notice them in the behavior of the simulated fluid. They would become much more obvious if they were displayed at the same time as the shadows. Thus for these reasons the shadow is not usually re-displayed by the system.

[00013] Finally, Figure 3.6 gives some insight into the potential of this embodiment for scientists, students, and even the general public to experiment with the model and begin to get a “feel” for how fluid dynamic systems work.

[00014] In yet another embodiment, Figure 4., the camera is pointed directly at the objects representing the solid boundaries, which has a background of contrasting brightness placed behind them. A chroma-keyed "green screen"-- a standard tool in the art of video production -- could be used here to provide the contrasting background. This allows the threshold process to produce an isolated image of the objects in the same fashion as before, following all the same steps as the initial embodiment. One significant difference is that, unlike the initial embodiment, in this alternate setup the new boundaries computed from the camera image are actively displayed in the flow visualization as dark silhouettes. This is necessary because there is no shadow cast on the flow field image. In fact, the flow field does not need to be projected in this case, and can be easily displayed on any type of computer monitor or display.

[00015] The inventor also proposes another embodiment, depicted in Figure 5, in which the original camera image of the actual objects used to compute the boundary conditions is itself overlaid onto the fluid simulation. In this embodiment, this effect would be optimal if a device such as a "green screen" were employed. This would allow the fluid flow display to actually show the actual image of the object in the fluid flow, giving the appearance of the person and/or object actually being immersed in the flow, adding some realism to the depiction. A bench or shelf covered with the same "green screen" coloring could be deployed on this embodiment, allowing the person or object to appear suspended in mid-fluid, swimming for example.

SUMMARY

Embodiments of the invention include a method for generating a computational fluid dynamics interactive digital display comprising: projecting a first image onto a surface, casting a shadow onto the surface by interdisposing at least one object between the surface and projection source, capturing a second image of the surface with cast shadows, and generating a computational fluid dynamics model with data from the second image. The method may be run consecutively where the first image projected onto the surface is related to the computational fluid dynamics model with data from the second image of a previous instance of the method. The data from the second image used to generate a computational fluid dynamics model may result from threshold, filtering, and edge detection techniques. Data from the second image may inform the computational fluid dynamics model of boundary conditions based on the location of the objects in the image. These images are intended to be generated and processed at video speeds of at least 10 frames per second, producing the effect of continuous interactivity with the computational fluid dynamics model. Higher speeds of 20-30 frames per second are preferable, but the speeds may be limited by the computational power available.

Embodiments of the invention include a method for generating a computational fluid dynamics interactive digital display comprising: placing at least one object within the field of view of a camera and between the camera and a high contrast background, capturing an image of at least one of the objects in front of the high contrast background,

generating a computational fluid dynamics model with data from the image, and displaying the computational fluid dynamics model. The method may be run consecutively to generate an interactive display. Data from the captured image and computational fluid dynamics model may be displayed onto the high contrast background. The captured image of an object may be displayed as an overlay of the boundary conditions generated for the object in the computational fluid dynamics model. The data may include the image of the object.

Embodiments of the invention include an interactive simulated fluid flow display comprising: a camera, a projector with a field of view that is within the field of view of the camera, and an algorithm that integrates data from the camera into a fluid flow simulation that may be then projected as an image.

FIGURE 1.

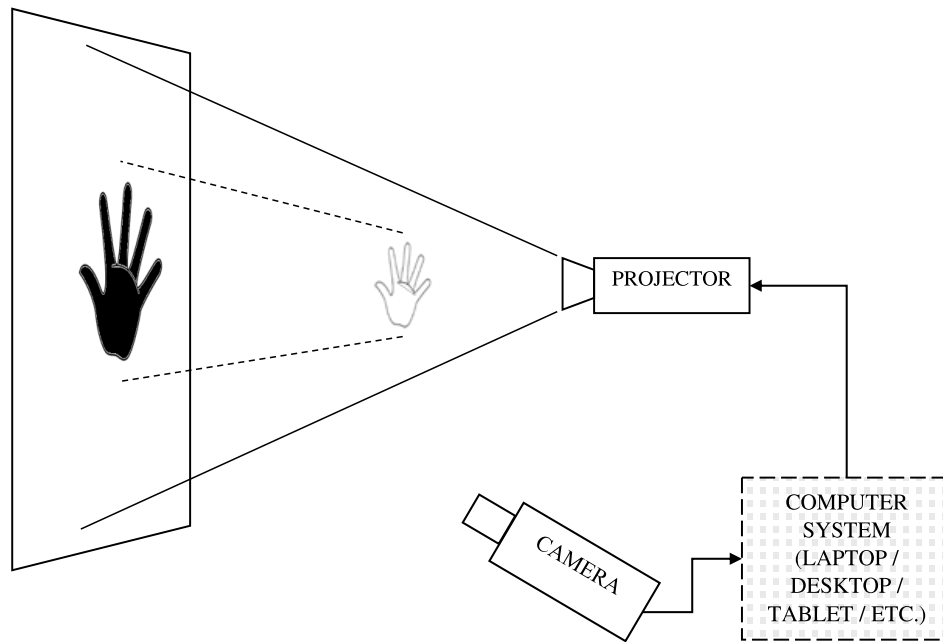


FIGURE 2.

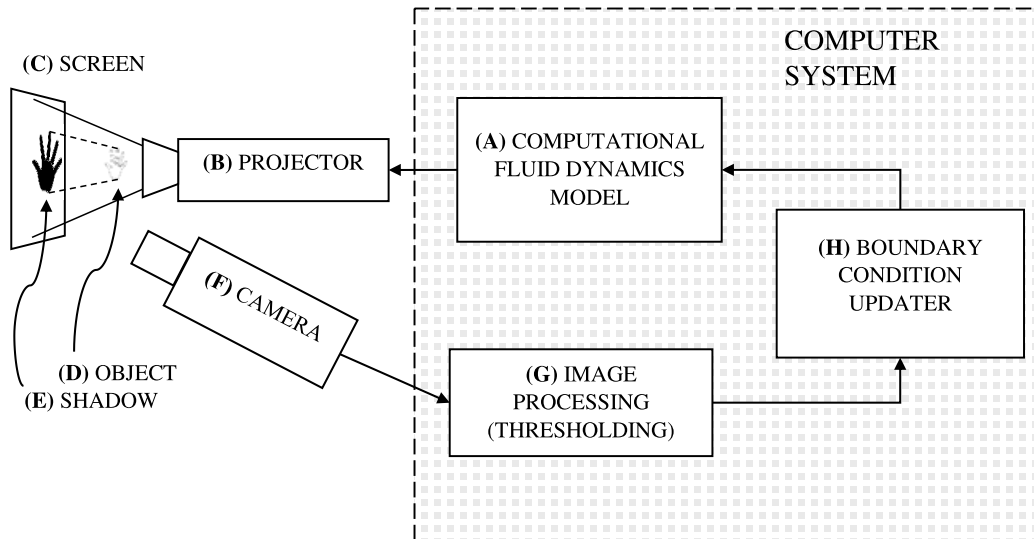


FIGURE 3.

All letters in parentheses, such as (A), refer to the items shown in Figure 2.

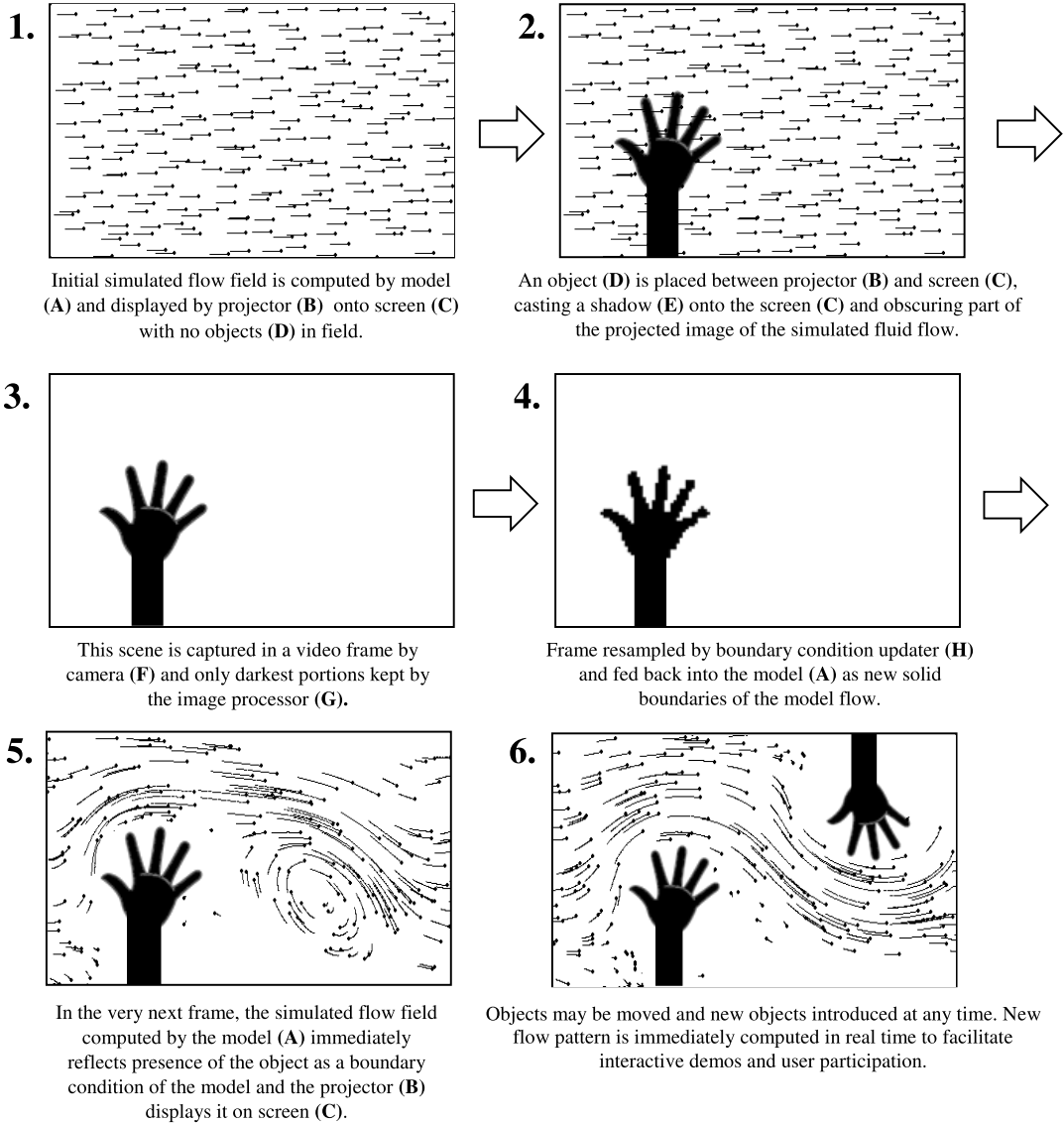


FIGURE 4.

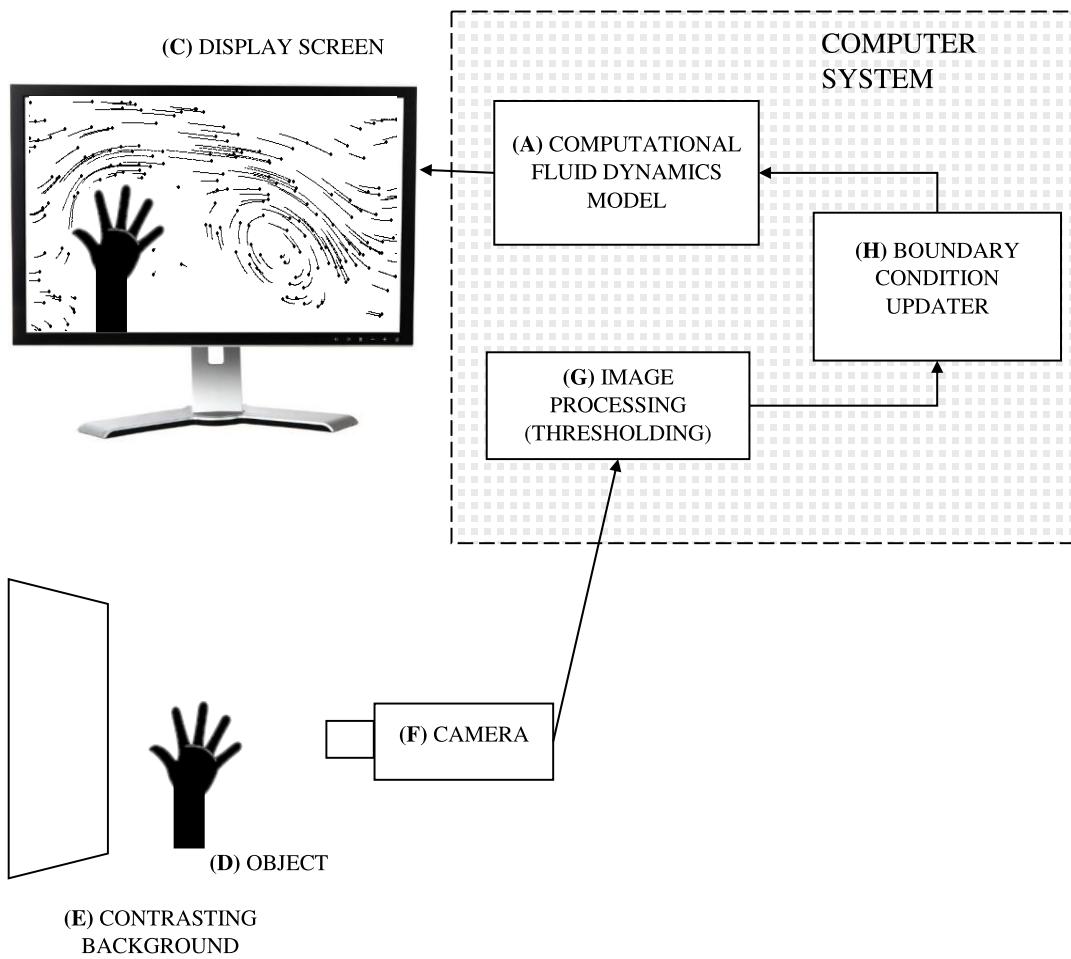


FIGURE 5.

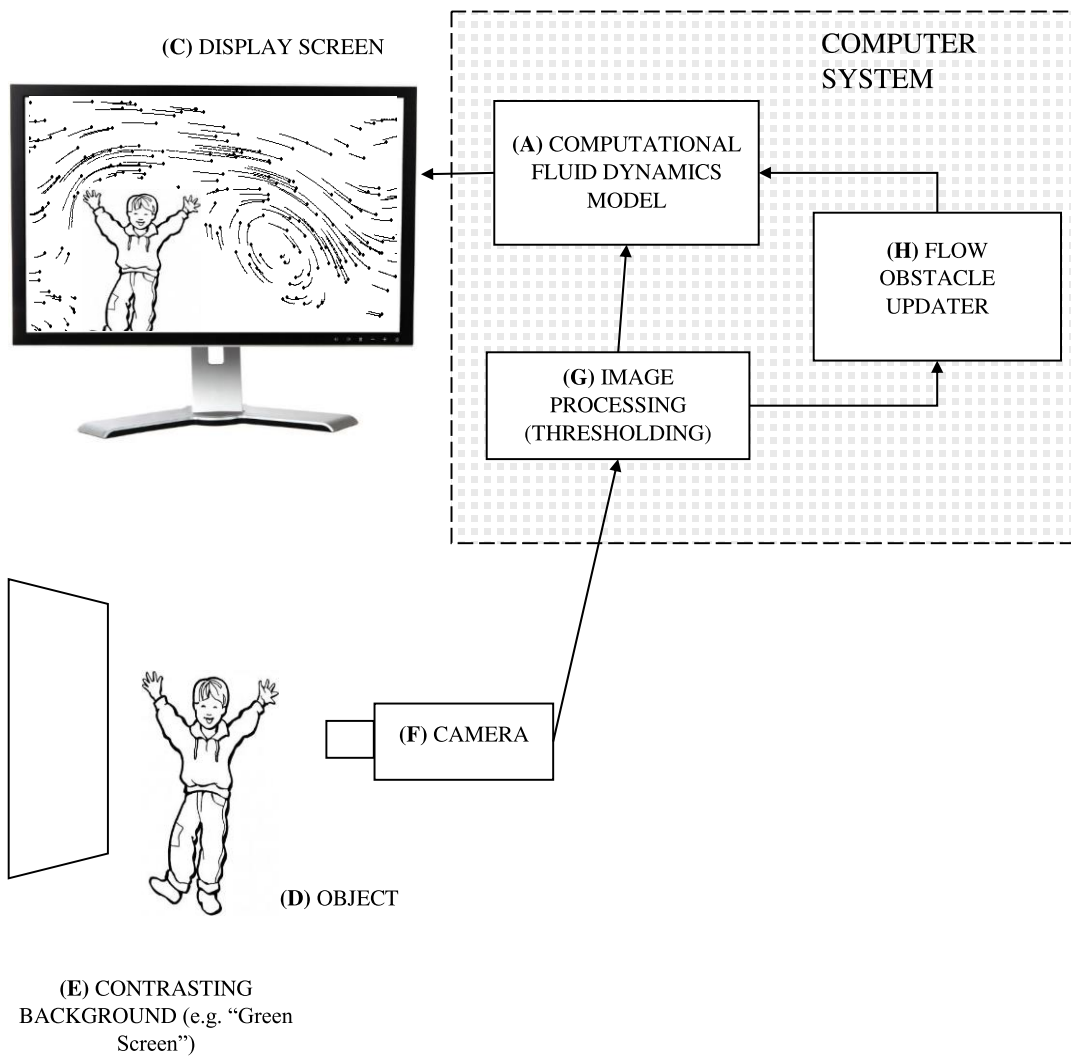
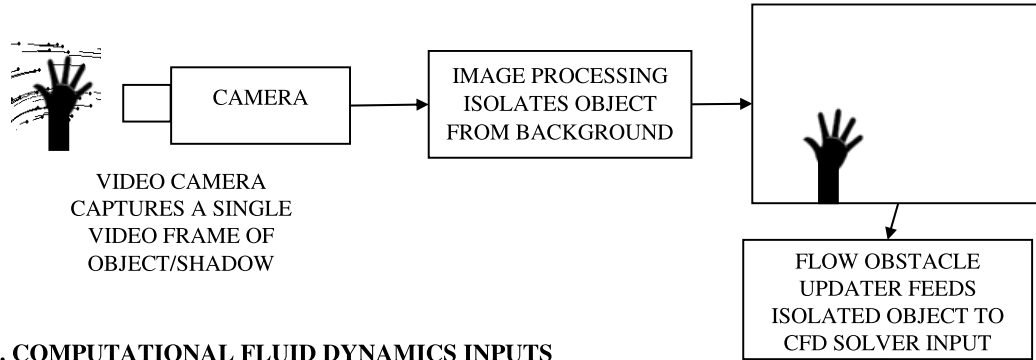
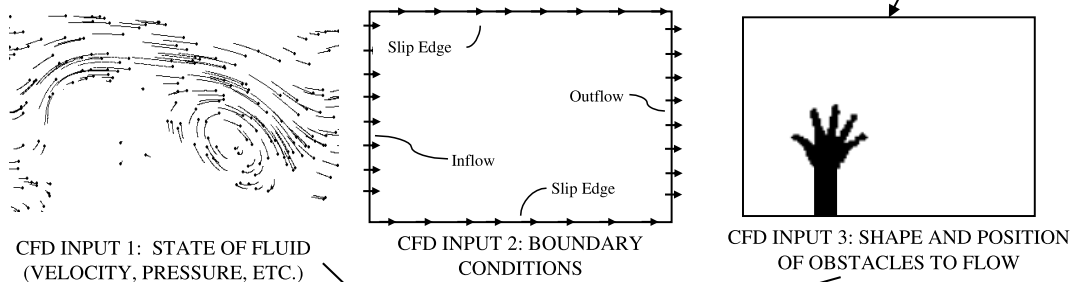


FIGURE 6.

A. CAMERA AND IMAGE PROCESSING



B. COMPUTATIONAL FLUID DYNAMICS INPUTS



C. DISPLAYING RESULT

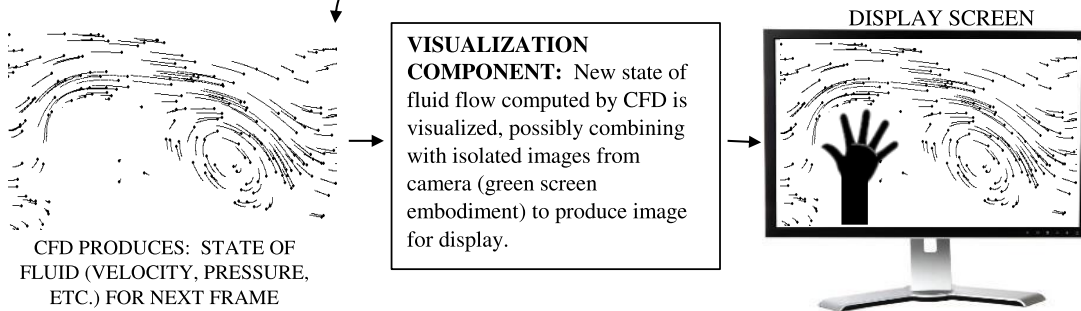
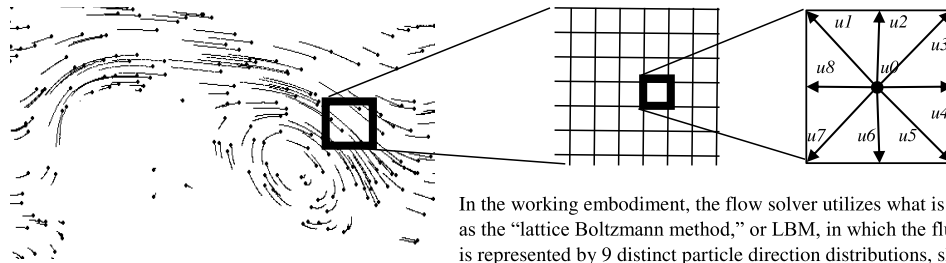


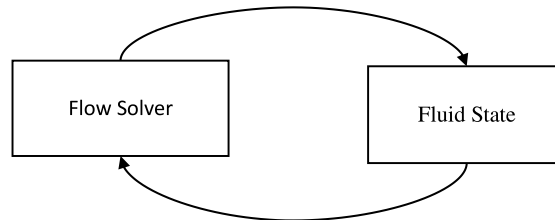
FIGURE 7. Details of flow solver operation.

A. A typical CFD flow solver models an effectively continuous fluid by breaking up the flow field into a grid of computational domains, each containing the physical characteristics of the fluid in that piece.

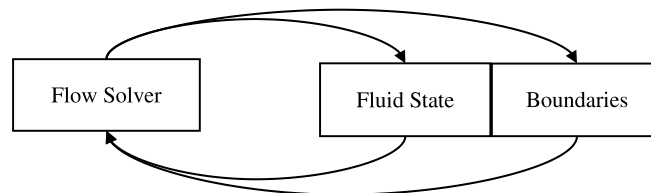


In the working embodiment, the flow solver utilizes what is known as the “lattice Boltzmann method,” or LBM, in which the fluid state is represented by 9 distinct particle direction distributions, shown here as $u0$ through $u8$. The overall physical properties of velocity and density are calculated from those values.

B. The lattice Boltzmann method, like most CFD methods, computes the fluid flow over fixed intervals, or time steps. So, the solver in effect takes the state of the fluid at time X , and computes what it will look like at time $X+t$, where t is the time step interval. Then the result is simply fed back into the model to get the next state, and so on.



C. In reality, to model anything but the simplest theoretical situations, the fluid state is augmented by the addition of external inputs--- basically, the (potentially changing) conditions under which the fluid is being modeled. For the working embodiment, these largely comprise the boundary conditions for the model: the size and shape of the channel in which the fluid is flowing as well as any objects which the fluid will encounter in its path.

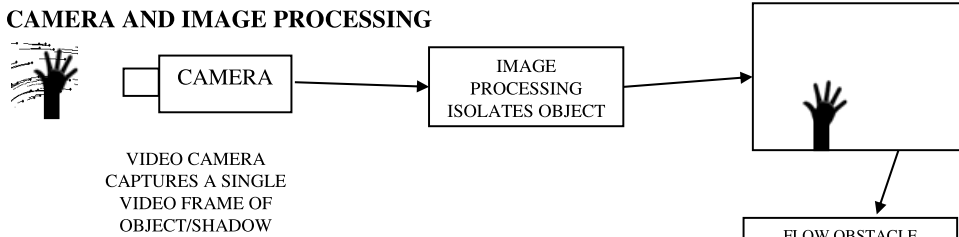


(Note that there is an arrow from the solver to the boundaries. Some flow solvers do model and compute phenomena such as erosion, sediment transport, and even larger objects freely flowing in the fluid. This is not strictly true of the working embodiment of this invention, unless you consider the reactions of the participants to the flow field modifying their behavior, as constituting the completion of that arrow.)

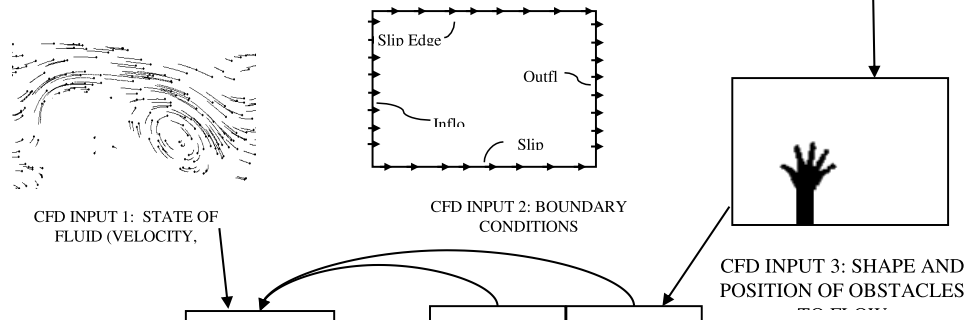
Figure 7 (cont'd)

D. In the working embodiment, a digital video camera, or webcam, is used to define some of the boundary conditions. So, using the previous graphic as a base, we can work in the other elements and see where they fit in this scheme.

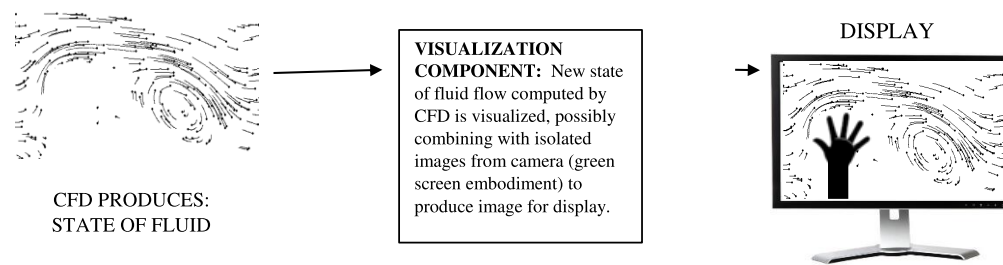
A. CAMERA AND IMAGE PROCESSING



B. COMPUTATIONAL FLUID



C. DISPLAYING



THOMAS F. HANSEN

Senior Information Processing Consultant
UWM School of Freshwater Sciences
University of Wisconsin–Milwaukee
tomh@uwm.edu

PROFESSIONAL PREPARATION

- University of Wisconsin—Milwaukee, B.Sc., Computer Science with Chemistry minor, 1991
- University of Wisconsin—Milwaukee, PhD Student, UWM School of Freshwater Sciences. Expected graduation: Spring 2021.

APPOINTMENTS

- Senior Information Processing Consultant, Indefinite Appointment, UWM School of Freshwater Sciences, 2011–Present
- Senior Information Processing Consultant, Probationary Appointment, Great Lakes WATER Institute and School of Freshwater Sciences, University of Wisconsin—Milwaukee, 2005–2011
- Senior Information Processing Consultant, Fixed-Term Appointment, Great Lakes WATER Institute, University of Wisconsin—Milwaukee, 2002–2005
- IT Consultant, Database Administrator, and Webmaster, Dentalworkers, Inc., 2000–2004
- Senior Web Developer, Software Engineer, Database Administrator, and Interactive Media Producer, Cybertoons Corporation, Milwaukee, Wisconsin, 1999–2002
- Software Developer, Consultant, and Webmaster, Real Easy Real Estate Software and Executive Systems, Ltd., 1987–1999
- Freelance web developer, various clients, 1997–present

SYNERGISTIC ACTIVITIES

Web Site Development

- I created the WATER Institute’s first comprehensive web site virtually from scratch in 2003. This included spearheading the design of a new logo for the Institute, as well as interviewing virtually all WATER researchers and scientists to develop the content. I single-handedly acted as web developer, graphic designer, science writer, and computer programmer to accomplish this task.
- In 2005 I created an automated time-lapse webcam system depicting the Milwaukee inner harbor. It is very popular with the general public, and its imagery is regularly used by the National Weather Service to help in reporting visibility status for the harbor, as well as by other agencies. It is, as of October 2015, in use by local TV stations in their weather forecasts.

Database and Data Management

- *Milwaukee Harbor WiFi*: I worked with the IT staff of Pier Wisconsin/Discovery World in 2005 to install an 802.11 (“Wi Fi”) access point on Cudahy Tower on the Milwaukee

lakefront. This installation has provided wireless data connectivity in support of a variety of very important programs on the local, state, and federal levels, including Discovery World's schooner S/V Denis Sullivan and UWM's R/V Neeskay, the NOAA GLERL Milwaukee weather station, and the UWM GLUCOS buoy sensor array.

- *Marine Database*: Created a shipboard data collection and database system for the R/V Neeskay which records depth, water temperature and GPS data in real time, and supports additional sensors as well. This system has provided very valuable support for numerous research programs.
- *Funded Research*: Received grant funding in 2005 from the UWM Center for Water Security (CWS) for a project entitled "Engineering Intelligence for Remote Data Acquisition Systems." I documented this work in detail as part of the Center's quarterly reports to its funding agency, the U.S. Defense Advanced Research Program Agency (DARPA). The results of my DARPA-funded CWS work were applied to the creation of a CO₂ data acquisition system that collected data for almost two years.

PRESENTATIONS AND PUBLICATIONS

- Kipp, J., & **Hansen, T.** (2006). A Software Framework for an Integrated Observing System. *OCEANS 2006 Conference* (pp. 1-3). Presented at the OCEANS 2006 Conference, Boston, MA.
- **Hansen, T. F.** (2006). A Networked, Real-Time Control and Data Acquisition System. Presented at the International Association for Great Lakes Research, Windsor, ON.
- Consi, T. R., Barske, G., Bootsma, H., **Hansen, T.**, Janssen, J., Klump, V., Paddock, R., et al. (2006). GLUCOS: The Great Lakes Urban Coastal Observing System. *OCEANS 2006 Conference* (pp. 1-5). Presented at the OCEANS 2006 Conference, Boston, MA.
- Consi, T. R., Anderson, G., Barske, G., Bootsma, H., **Hansen, T.**, Janssen, J., Klump, V., et al. (2009). Measurement of spring thermal stratification in Lake Michigan with the GLUCOS observing system. *OCEANS 2009 Conference* (pp. 1-5). Presented at the OCEANS 2009 Conference, Biloxi, MS.
- **Hansen, T.F.** (2010). Creation, Implementation, and Practical Field Use of a Real-Time Bathymetry Mapping System Created with Open-Source Tools as an Adjunct to Multibeam Surveys. Presented at the International Association for Great Lakes Research, Toronto, ON.
- Thompson, Andrew, Basil Hable, Kyana Young, **Thomas Hansen**, J. R. Strickler, and Marcia R. Silva. "Optically Based Hand-Held Sensor for Visualization and Quantification of *Cryptosporidium Parvum*." *Sensing and Imaging* 21, no. 1 (September 29, 2020): 46. <https://doi.org/10.1007/s11220-020-00311-5>.
- Thompson, Andrew, Basil Hable, Adam Honts, J. R. Strickler, **Thomas Hansen**, and Marcia R. Silva. "Optically Based Bacteria Hand-Held Sensor: From Fundamentals to Proof of Concept." *Sensing and Imaging* 21, no. 1 (August 4, 2020): 41. <https://doi.org/10.1007/s11220-020-00306-2>.